Silver Nanowire Arrays: Fabrication and Applications

Dissertation submitted for the degree of Doctor of Natural Sciences (Dr. rer. nat.)

Presented by

Yuyi Feng

at the

Universität Konstanz

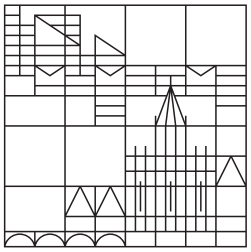

Faculty of Mathematics and Natural Sciences
Department of Physics

Date of the oral examination: December 16, 2016
First referee: Professor Dr. Lukas Schmidt-Mende
Second referee: Professor Dr. Eva Weig

Contents

Abstract

Nanowire arrays have increasingly received attention for their use in a variety of applications such as surface-enhanced Raman scattering (SERS), plasmonic sensing, and electrodes for photoelectric devices. However, until now, large scale fabrication of device-suitable metallic nanowire arrays on supporting substrates has seen very limited success.

This thesis describes my work first on the development of a novel successful processing route for the fabrication of uniform noble metallic (e.g. Ag and Au) nanowire arrays on ITO (and other) substrates. Ag nanowire arrays are studied in detail. I use an in situ oxygen plasma cleaning process and a sputtered Ti layer to enhance the adhesion between the anodic aluminum oxide (AAO) template and the ITO glass. An ultrathin gold layer (2 nm) is deposited as a nucleation layer for the electrodeposition of silver. Furthermore, a stable cyanide-free electrolyte compatible with the AAO templates is developed. Ultimately, an unprecedented high level of uniformity and control of the nanowire diameter, spacing, and length has been achieved.

Moving forward, new architectures for organic solar cells are employed, based on such nanostructured electrodes, covered with a separate zinc oxide (ZnO) layer. Two types of solar cells are presented in this thesis. One is a traditional opaque solar cell with a thick (100 nm) Ag back contact. The other is a semi-transparent solar cell with a transparent top electrode (consisting mainly of Ca:Ag). Complementary characterization tools enable further in-depth investigation of the optical and electronic properties of such devices. The results show that the Ag nanowire arrays seem to enhance the charge collection efficiency. However, using too thick a polymer film (which is necessary to ensure a working device) combined with the increased nanowire-polymer interface, introduces extended defect sites for recombination, which limits the efficiency of the nanowire solar cell. Finally, this work yields a clearer design route for Ag nanowire organic solar cells, suggesting a use of a proper semiconductor layer with low recombination rate as well as a very thin polymer layer to conformally coat the Ag nanowire arrays. In this way, the nanowire solar cells not only make use of the charge collection and light trapping advantages of Ag nanowires, but also minimize recombination losses.

Additional techniques explored on metallic nanowire arrays as part of this project included Raman and low-temperature (< 80 K) angle-dependent UV-Vis, which pave the way for potential applications in SERS, temperature sensing, and many other areas.

Zusammenfassung

Nanowire Arrays haben wachsende Aufmerksamkeit für eine Vielzahl von Anwendungen erfahren, wie z.B. oberflächenverstärkte Raman Streuung (SERS), plasmonische Sonden und Elektroden für Photovoltaik. Bisher war die Herstellung von Metall-Nanowire Arrays auf Trägersubstraten in einer Größenordnung, die für die Deviceproduktion geeignet ist, bedingt erfolgreich.

Zuerst beschreibt diese Arbeit die erfolgreiche Entwicklung eines neuen Fertigungsprozesses, der die Herstellung von gleichmäßigen Edelmetall-Nanowire Arrays (z.B. Ag und Au) auf ITO und anderen Substraten erlaubt. Ag Nanowire Arrays werden im Detail untersucht. Um die Adhäsion zwischen dem anodischen Aluminiumoxid (AAO) Templat und dem ITO-Glas zu verbessern, wird ein in situ Sauerstoffplasmareinigungsschritt verwendet und eine Ti-Schicht aufgesputtert. Ein ultradünner Goldfilm (2 nm) wird als Nukleationsschicht für die Elektrodeposition von Silber abgeschieden. Ferner wird ein stabiler cyanidfreier Elektrolyt, welcher mit den AAO-Templaten kompatibel ist, entwickelt. Schließlich wurde ein beispiellos hoher Grad an Gleichmäßigkeit und Kontrolle über Durchmesser, Abstand und Länge der Nanowires erreicht.

Des Weiteren werden neuartige Bauweisen für organische Solarzellen verwendet, basierend auf solchen nanostrukturierten Elektroden, die mit einer Zinkoxid-Schicht (ZnO) bedeckt sind. Zwei Typen von Solarzellen werden in dieser Arbeit vorgestellt. Einer ist eine herkömmliche opake Solarzelle mit einer dicken (100 nm) Ag-Rückelektrode. Der andere ist eine Semitransparente Solarzelle mit einer transparenten Topelektrode (hauptsächlich bestehend aus Ca-Ag). Komplementäre Charakterisierungstechniken ermöglichen weitere in die Tiefe gehende Untersuchungen der optischen und elektronischen Eigenschaften einer solchen Solarzelle. Die Ergebgnisse zeigen, dass die Ag Nanowire Arrays die Effizienz der Ladungsträgerkollektion verbessern. Allerdings führt die Verwendung eines ausgedehnten Polymerfilms, welcher für die einwandfreie Funktion der Solarzelle benötigt wird, auch zu einem erhöhten Aufkommen von Defekten, die ihrerseits wiederum die Effizienz der Nanowire-Solarzelle begrenzen. Schließlich geht aus dieser Arbeit die Empfehlung hervor, beim Design von organischen Ag Nanowire Solarzellen geeignete Halbleiterschichten mit niedrigen Rekombinationsraten zu verwenden, sowie sehr dünne Polymerschichten, die die Ag Nanowire Arrays gleichmäßig bedecken. Auf diese Weise nutzen die Nanowire Solarzellen nicht nur die Vorteile bei Ladungsträgerkollektion und Lichteinfang, die Nanowires mit sich bringen, sondern minimieren außerdem Rekombinationsverluste.

Zusätzlich wurden fortgeschrittene optische Methoden, wie Raman und winkelabhängige tieftemperatur (< 80 K) UV-Vis auf metallische Nanowire Arrays angewendet. Dies ebnet den Weg für potentielle Anwendungen in SERS, Temperaturbestimmung und vielen anderen Bereichen.

1. Motivation

1.1. Introduction

One of the biggest challenges humanity is facing today is the looming global energy crisis. Renewable energy plays a crucial role, not only in meeting the increasing energy demand, but also in addressing the problem of escalating air pollution.[1] By 2014, renewables already contributed a share of 13.8% to the total energy supply (Figure 1.1 left), and this share is predicted to continuously grow, according to the International Energy Agency (2016 edition).[2] Impressively, among all renewables, photovoltaics (PV) exhibited the fastest annual growth rate of 46.2% between 1990 and 2014 (Figure 1.1 right).[2] At present, the PV market is dominated by polycrystalline silicon solar cells.[3] However, the costs are so high that this model cannot guarantee substantial uptake of photovoltaics by consumers.[4] This high costs of polycrystalline silicon solar cells is mainly due to the expensive and energy-intensive high-temperature process.[1]

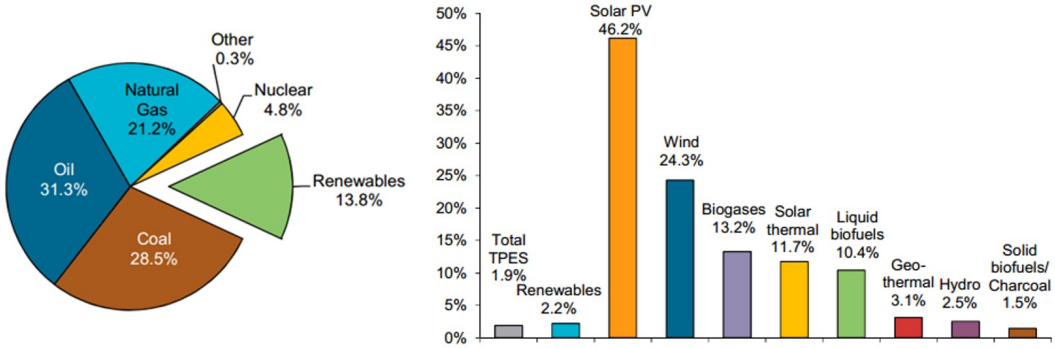

Figure 1.1.: Left: World total primary energy supply in 2014. Right: Annual growth rates of world renewables supply from 1990 to 2014. Reprinted with permission from [2]. ©OECD/IEA 2016 Renewables Information, www.iea.org/statistics, IEA Publishing. Licence: www.iea.org/t&c.

Organic solar cells (OSCs) can be considered as promising new alternatives, not only owing to their low cost fabrication process (e.g. roll-to-roll process), but also owing to their other attractive advantages such as being light-weight and compatible with flexible substrate.[5] Examples of three conceptional applications of OSCs - roof-top OSCs for parking canopies, roof-top OSCs for cars, and semi-transparent OSCs for buildings - are depicted in Figure 1.2.

Figure 1.2.: Conceptional applications for organic solar cells (OSCs). Left: Konarka roof-top OSCs for parking canopies.[6] Middle: roof-top OSCs for the concept car "Smart Forvision".[7] Right: semi-transparent OSCs for SwissTech Convention Center. This picture was made by Solaronix (Photographer: David Martineau).[8]

However, the power conversion efficiency of OSCs ($\eta_{\max} \sim 10\%$ [9]) falls far behind their inorganic counterparts ($\eta_{\max} \sim 25\%$ [10]). Extensive studies worldwide are focusing on overcoming the current limitations of OSCs to further improve their efficiencies.

1.2. Operation of Organic Solar Cells

The typical structure of an organic solar cell (OSCs) consists of a photoactive layer sandwiched between electron and hole selective contacts.[11] The widely used photoactive layer is a three-dimensional intermixing of a donor and an acceptor materials, which is referred to as a bulk heterojunction (BHJ). Figure 1.3 illustrates the basic working principles of BHJ OSCs [11–15]:

- Step 1: BHJ materials absorb light and generate coulombically bounded electro-hole pairs, i.e., Frenkel excitons.
- Step 2: excitons diffuse to the donor-acceptor interface and split up into free-charge carriers. The driving force is provided by the energetic off-set between the donor and acceptor materials.
- Step 3: free charges migrate towards different electrodes by the build in electric field.
- Step 4: free charges are collected at the electrodes.

Although significant process in understanding the basic working principles of BHJ OSCs has been made, many fundamental questions such as the mechanisms of charge generation, transport, collection and recombination are still under debate and remain unclear.[11, 16]

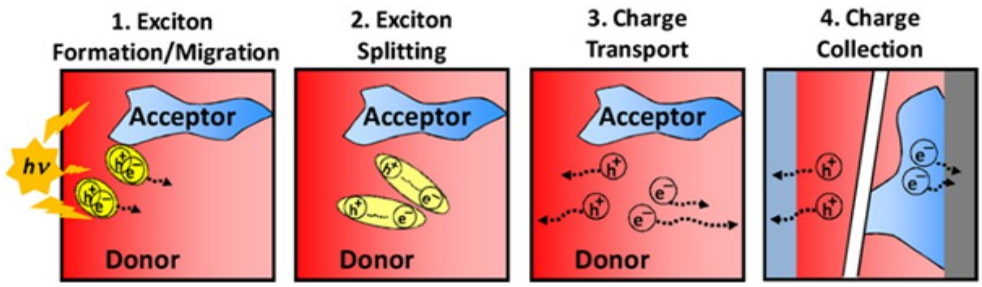

Figure 1.3.: Basic working principles of bulk heterojunction organic solar cells (BHJ OSCs). Courtesy of Facchetti.[12]

1.3. Nanowire Electrodes for Solar Cells

One major limiting factor for organic solar cells is low carrier mobilities, leading to poor charge collection efficiency.[14] To overcome this limit, a promising way is to incorporate inorganic nanowire (or nanorod, nanocone) arrays into OSCs. This is because the one-dimensional nanowire arrays can provide direct pathways for fast charge transport.[17–19] Specifically, if the interfacial spacing is the order of double of exciton diffusion length, all dissociated charges would be perfectly collected by nanowire electrodes before they could recombine. Besides, plenty of studies have shown that nanowire arrays can efficiently enhance light harvesting through introducing scattering at interfaces where the neighboring materials have different refractive indices.[20–27] Moreover, some nanowire solar cells show high angle acceptance of incident light, which provides for practical deployment of solar panels without installation of costly solar tracking systems.[28, 29]

However, due to the huge junction area, most semiconductor nanowire solar cells face limitations in device performance due to charge recombination across material interfaces, leading to poor solar cell performance.[30–33] Many research groups have tried to address this issue by developing metal oxide core-shell nanowire arrays.[33–36] For example, a conductive metal oxide core (e.g. ZnO) is coated with a shell layer with an offset conduction band (e.g. TiO_2, Al_2O_3) in order to further increase distance between electron-hole pairs while simultaneously promoting charge extraction along the axis of the nanowire.[33] This strategy was further employed in doped TiO2 core-shell wires to amplify the electron mobility in the core of the wire without forming a recombination center along the internal interface.[33, 37] Additionally, these wires promote field amplification via plasmonic resonance as well as acting as a light scatterer [38], leading to an increase in absorption in the surrounding active layers of the organic solar cells.[33]

1.4. Outline of the Thesis

This thesis addresses the impact of free-standing silver nanowire arrays on the device physics of organic solar cells. **Chapter 1** gives a very brief introduction to the basic principles of organic solar cells and the concept of nanowire solar cells. Subsequently, a short description of experimental methods is presented in **Chapter 2**. In **Chapter 3**, it is for the first time demonstrated that large-area free-standing silver nanowire arrays can be fabricated on ITO glass via template-assisted electrodeposition in a controllable way. Moreover, the optical properties of plasmonic silver nanowire arrays such as ultra violet-visible (UV-Vis) spectra and surface enhanced Raman (SERS) spectra are also presented.

Chapter 4 discusses how the free-standing silver nanowire arrays were further conformally coated by a semiconductor (e.g. ZnO) shell, forming Ag-ZnO core-shell nanowire arrays. The chapter also presents how the organic solar cell devices (opaque&semi-transparent) comprising Ag-ZnO core-shell nanowire arrays were realized. An in-depth investigation of device physics such as external quantum efficiency (EQE), charge collection and recombination gives an clearer design route for nanowire solar cells.

In **Chapter 5**, conclusions are drawn, and an outlook for future research is given.

2. Experimental Methods

This chapter provides an overview of experimental methods used during my PhD research. I will attempt to give an overview of the experimental techniques, and the information that can be obtained from them. For the exact fabrication and measurement parameters, you can find them in the experimental section of each chapter. More details about the makes and models of the equipments can be found in literature and books cited as references.

2.1. Scanning Electron Microscopy (SEM)

Scanning Electron Microscopy (SEM) is one of the most powerful tools for the characterization of nanomaterials. The SEM operates by using an accelerated incident electron beam to strike the surface of the sample. The scattered electrons from the sample are then collected by the detector to generate images. In this project, for SEM analysis, a Carl Zeiss 1540 XB system was used with a field emission cathode source under high vacuum. The operating acceleration voltages were between 1 kV and 5 kV, which could lead to a theoretical resolution of approximately 2 nm with an actual resolution estimate around 10-20 nm depending on the user experience. The working distance was between 1 mm and 6 mm.The SEM2 mode and InLens mode were mostly used. The SEM2 mode collects both back-scattered electrons (elastic) and the secondary electrons (inelastic); this method was able to generate images, although resolution was limited at high magnifications. However, the InLens mode mainly collected the secondary electrons that were close and highly sensitive to the sample surface (see Figure 2.1) and thereflectionore could produce high resolution topographical images of the specimen.[39]

Samples were stuck onto steel stubs with silver paste. For non-conductive materials, approximately 2 nm Au was sputtered on the sample surface to avoid charging effects. Cross-sectional samples were scratched from the reverse side of the substrates with a glass cutter and cleaved manually. If necessary, the samples were immersed in liquid N_2 beforehand.

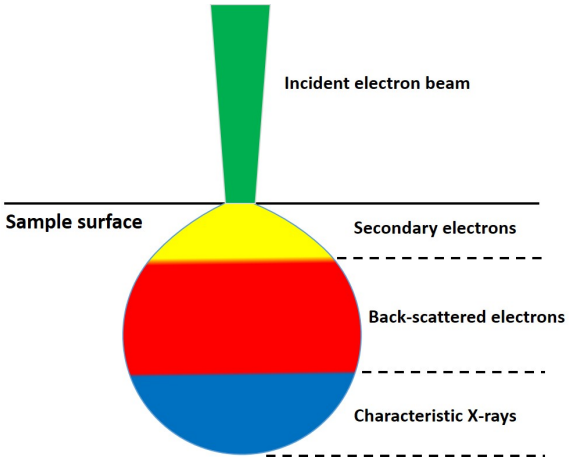

Figure 2.1.: SEM interaction volume for various electron-specimen interactions. Based on Zhang et al.[39]

2.2. Four-Point Probe

Four-point probe is widely used for measuring the sheet resistance of thin films. The sheet resistance is defined as the resistivity per film thickness, therefore

$$R_{\text{sheet}} = \frac{\rho}{t} \tag{2.1}$$

where ρ is the electrical resistivity and t is the film thickness.

The schematic configuration of our homemade four-point probe is shown in Figure 2.2. A Keithley SourceMeter2400 is used to provide a current though the outer probes, and the voltage is measured between the inner probes.[40] The sheet resistance is then obtained as

$$R_{\text{sheet}} = 4.532 \cdot \frac{V}{I} \tag{2.2}$$

2.3. Current-Voltage (J-V) Measurement

Current-voltage (J-V) measurement is the simplest, and probably the most important technique for characterizing solar cells. While the power conversion efficiency (PCE) is the primary parameter extracted from the J-V curve, careful analysis of the curve can lead to rich information about the physics of solar cells. The J-V curve can be measured under illumination with an AM1.5G (AM: air mass) simulated spectrum as well as in the dark with a light proof overlay. Figure 2.3a schematically displays a J-V setup. A

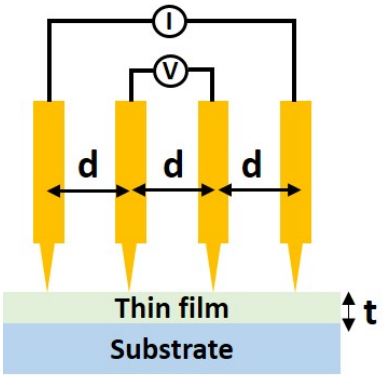

Figure 2.2.: Four-point probe scheme. In practical terms, four gold pin probes are arranged in a straight line with an identical distance of 1 mm between them.

solar simulator (typically a Xenon lamp combined with an AM1.5G filter) shines light on a masked solar cell sample. A sourcemeter supplies the sweeping voltage, and the corresponding current is measured, resulting in the J-V graph (shown in Figure 2.3b). The common characteristics of solar cells are:

- Short-circuit current (J_{SC}): the current-density at 0 V bias.
- Open-circuit voltage (V_{OC}): the voltage at 0 current-density.
- Fill factor: the "squareness" of the J-V curve; $FF = J_{MPP}V_{MPP}/(J_{SC}V_{OC})$.
- Power conversion efficiency (PCE): the ratio of the converted electrical energy to the incident radiative energy; $PCE = P_{max}/P_{in} = J_{SC}V_{OC}FF/P_{in}$, where P_{max} is the maximum output power, P_{in} is the incident light power.

Additionally, in practical application when the solar cell is connected to an electrical load, the optimal working condition is at the maximum power point (MPP).

In concrete terms, J-V measurements were carried out on two different homemade systems (the old system designed by Holger Hesse, et al.; the new system with batch-testing capabilities designed by Eugen Zimmerman). The old system used a LOT Oriel LS0106 150 W Xe-Lamp, and the new system used a LOT Oriel LS0106 1000 W Xe-Lamp. Both lamps were combined with an AM1.5G filter. The light intensity was calibrated using a silicon reference solar cell with a KG5 filter certified by the Frauenhofer Institute. For standard J-V measurement, light intensity was adjusted to 100 mW/cm^2. And for light-intensity dependent J-V measurement, the neutral density filters were used to change the intensities from 0.3 to 100 mW/cm^2. The active solar area (using a mask) was 0.125 cm^2. The current was recorded with a typical sweeping voltage at a scan rate of 0.01 V and integration time of 0.01 s at each voltage point. These parameters are typical for organic solar cells in this thesis, but for other types of solar cells, e.g. perovskite solar cells, the values need re-adjusting to reach a dynamic equilibrium at each applied

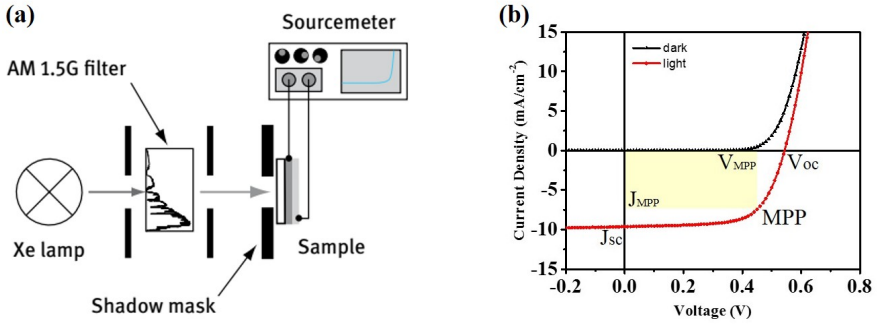

Figure 2.3.: (a) Setup for J-V measurement. Reprinted with permission from Lukas Schmidt-Mende & Jonas Weickert, Organic and Hybrid Solar Cells. An Introduction, Berlin, Boston: De Gruyter, 2016, pp. 212, fig. 4.10.[15] (b) A typical J-V curve of a solar cell sample under illumination and in the dark.

voltage. For further detailed description regarding, for example, the geometry of solar cells, please see Holger Hesse's dissertation.[41] All J-V measurements were adhered to the key rules advised by Schmidt-Mende and Snaith.[42, 43]

2.4. External Quantum Efficiency (EQE) Measurement

External quantum efficiency (EQE) measurement is probably the second most important technique for characterizing solar cells, which gives the detailed information about the spectrally resolved photocurrent of J-V curves. The EQE is defined as the ratio of the number of photogenerated electrons to the number of incident photos (also referred to as incident photon to current conversion efficiency (IPCE)). In terms of experimentally measurable quantities, the expression of EQE is derived as

$$EQE = \frac{J(\lambda)}{e} \cdot \frac{hc}{P_0(\lambda)\lambda} \tag{2.3}$$

where $J(\lambda)$ is the current density, e is the electronic charge, h is Planck's constant, c is the vacuum velocity of light, $P_0(\lambda)$ is the power of the incident light at wavelength λ. An EQE setup is illustrated schematically in Figure 2.4a. Similar to the layout of the J-V setup, a monochromator (LOT Oriel Omni 150) was additionally positioned between the 150 W Xe-Lamp and sample. The intensity of the resulting monochromatic light (FWHM 5 nm; $\ll 100\,\mathrm{mW/cm^2}$) was calibrated using a silicon reference solar cell with a KG5 filter certified by Frauenhofer Institute. Typically, the EQE spectra were obtained at wavelengths of 300-800 nm in steps of 2-4 nm (bias 0 V). In my case, most EQE measurements were performed without a white light background. A sample EQE curve for P3HT:PCBM organic solar cells is shown in Figure 2.4b.

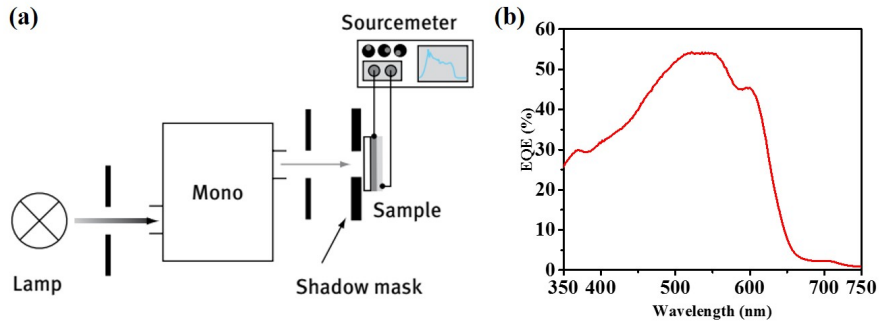

Figure 2.4.: (a) Setup for EQE measurement. Reprinted with permission from Lukas Schmidt-Mende & Jonas Weickert, Organic and Hybrid Solar Cells. An Introduction, Berlin, Boston: De Gruyter, 2016, pp. 219, fig. 4.16.[15] (b) A typical EQE curve for a solar cell sample.

Since EQE is the photon response of the solar cell at a given wavelength, the integral of the EQE with the solar spectrum should give the J_{sc} under the specific light intensity, therefore

$$J_{\mathrm{SC}}^{\mathrm{calc}} = \int eEQE(\lambda)N_{\mathrm{P}}(\lambda)d\lambda \tag{2.4}$$

where e is the electronic charge, $EQE(\lambda)$ is the external quantum efficiency at wavelength λ, $N_{\mathrm{P}}(\lambda)$ is the total number of incident photons per second per square centimeter, which is derived from the AM1.5G solar spectrum.[42] A comment about how important it is to cross-check the EQE and J-V results to make sure both measurements are valid was published by Zimmermann et al.[42] in 2014, and I would like to refer the reader to this paper for the details. The main point is the $J_{\mathrm{SC}}^{\mathrm{calc}}$ should be equal to or more than the measured J_{SC}.

Additionally, the EQE divided by the total absorption of the solar cell (Abs) yields the internal quantum efficiency (IQE), therefore

$$IQE(\lambda) = \frac{EQE(\lambda)}{Abs(\lambda)} \tag{2.5}$$

The unit of Abs here is %. The Abs (%) can be calculated from the experimentally measured absorbance A (also referred to as optical density (OD)) as

$$Abs(\lambda) = 1 - 10^{-\mathrm{A}(\lambda)} \tag{2.6}$$

Since the IQE excludes the optical losses of the solar cell, it is used to analyze the charge transport properties of the device.

2.5. Ultra Violet-Visible Light-Near Infrared (UV-Vis-NIR) Measurement

Ultra violet-visible light-near infrared (UV-Vis-NIR) measurement is widely used to characterize the optical properties of the sample (e.g. transmission, absorption and reflection). Figure 2.5 displays a simplified scheme of our UV-Vis-NIR setup (Cary 5000 series, Agilent Technologies). The system is capable of a direct measurement of absorbance, rather than extinction, because the integrating sphere contributes to eliminating the influence of scattering. In this thesis, all measurements were performed in a double beam mode with a zero/baseline correction (that is, the measured spectra were referenced to 100% and 0% transmittance). The spectra were typically scanned at a rate of 1 nm/s and a spectral bandwidth of 5 nm. Depending on the purpose of the measurement as well as the geometry of the samples, there were additional specific parameters (e.g. sample-positioning, sample-masking and beam size), which are described in their corresponding sections.

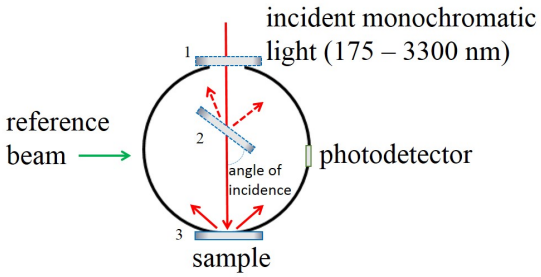

Figure 2.5.: UV-Vis-NIR setup with an integrating sphere. Samples can be positioned at 1) front port, 2) center of the sphere, and 3) back port, depending on the purpose of the measurement. Based on Manara et al.[44]

2.6. Other Measurements

A variety of other measurements such as X-ray diffraction (XRD), transmission electron microscope (TEM) , Raman, and photoelectron spectroscopy in air (PESA) were carried out in the process of data collection in this thesis. Since many of these measurements are standard in the lab, I will not go into details about these techniques.

3. Fabrication of Free-Standing Nanowire Arrays on Rigid Substrates

This chapter is partly based on the article *Uniform large-area free-standing silver nanowire arrays on transparent conducting substrates.* I planned and performed the experiments, wrote the manuscript and was responsible for editing. Clay A. Nemitz helped me with the optimization of the fabrication process and proof-reading.

3.1. Introduction

3.1.1. State of the Field Literature Review

3.1.1.1. Template-assisted Nanostructure Synthesis

Creation of nanostructure arrays such as nanowires, nanotubes, nanodots and nanobrushes [45] is a crucial prerequisite for the fabrication of advanced nanostructured devices. Over the past 60 years, numerous techniques have been developed to fabricate nanostructure arrays, including electron-beam lithography (EBL) [46], chemical vapor deposition (CVD) [47], hydrothermal growth [37], reactive inkjet printing (RIJ) [48], and template-assisted synthesis [33, 49–51]. The EBL and CVD methods are limited by their expensive and time-consuming processes. Hence, alternative methods for making nanostructure arrays are needed. For example, low-cost hydrothermal growth methods have been successfully developed for making ZnO [52], TiO_2 [37, 53], NiO [54] and VO_2 [55] nanowires. But so far, no metallic nanowires have been fabricated using the hydrothermal method, probably due to the challenge of finding the right precursors. Moreover, the rapid RIJ method has been recently demonstrated as a proof-of-concept to generate biocompatible rocket-like arrays. However, decreasing feature sizes to nanometer scale still remains a bottleneck, as the smallest size currently is around 10 μm.[48]

Template-assisted synthesis has been widely accepted as the most versatile method for fabricating nanostructure arrays.[56–58] The most common templates are track-etched templates (e.g. porous polycarbonate templates [59–64]), block copolymer templates [65–73], colloid nanosphere templates (e.g. polystyrene sphere templates [74–83]), and anodic aluminum oxide (AAO) templates [33, 84–90].

Track-etched templates are produced by bombarding polymer films with energetic ions, which results in the formation of linear tracks, followed by chemical etching to get

widened pores.[91, 92] By changing the conditions of bombardment and chemical etching, the pore size can be fine tuned from tens of nanometer to tens of micrometer with an aspect ratio of 1 - 1000, and meanwhile the porosity can be adjusted in the range of $10^5 - 10^{10}$ cm^{-2}.[93] However, these kinds of templates are disordered due to the random ion bombardment.[94]

Block copolymer templates are made from two or more chemically different polymers, which are covalently bonded in an "end-connecting" way [65] and self-assemble into well-ordered structures. By selectively removing one of the polymer blocks, one can achieve the desired porous templates. Highly ordered and uniform block copolymer templates on rigid substrates (e.g. Si) have been recently fabricated.[95–97] The typical pore size is 10-50 nm [98], and the porosity goes up to 10^{11} cm^{-2} and over [94]. However, these polymer templates are not heat-resistant (with melting point of up to 150°C [99]), and also not compatible with aqueous electrolytes due to their strong hydrophobic properties.

Besides block copolymer templates, self-assembly colloid nanosphere templates are another group of attractive soft templates, including polystyrene sphere (PS) and silica (SiO_2) sphere. A periodic (either hexagonally close-packed [100] or non-close-packed [101–103]) nano/micro-sphere monolayer template could be obtained by various methods such as lift-up of the substrate [104, 105], draining-off the water [100], spin-coating [101, 106, 107], and the very recently developed micro-propulsive injection (MPI) [108]. The colloid sphere size can range from tens of nanometer to tens of micrometer.[56]. However, until now, high-aspect-ratio noble metallic nanowire arrays have not yet been achieved using these templates, due to the templates' dimension limitations.[109] More detailed explanation can be found in Section 3.1.2.2.

Anodic aluminum oxide (AAO) templates are fabricated through an electrochemical anodization process of placing aluminum in an acidic solution, followed by chemical etching to get widened pores.[110] After a sufficient anodizing time, the pores can self-organize into highly ordered hexagonal structures, likely due to the repulsive mechanical forces between neighboring pores during the anodization process.[111] AAO templates possess a variety of advantages: they are highly ordered [111], have a low-cost fabrication process [112], are thermally stable (ca.1000°C) [113], and have a broad range of size (diameter: 14-200 nm, interpore distance: 50-500 nm, porosity: $10^8 - 10^{11}$, aspect ratio: up to ca.1000, pore length: up to ca.100 μm) [94, 114, 115]. Furthermore, thanks to recent developments, the AAO templates are no longer limited to vertically aligned one-dimensional (1D) nanopores, but have been modulated into fascinating 3D structures such as 3D hierarchically branched nanopores [116–118], 3D interconnected nanotubular networks [119], and AAO microcavities [120], by cleverly tuning the anodizing voltage. Considering the easy-processable and size-tunable merits, AAO templates are selected as the nanostructure synthesis technique in this work. In particular, in terms of controlling the size and shape of the AAO pores, it is highly desirable to investigate how the nanostruture influences the solar cell performance.

Moreover, tremendous progress has been made regarding the pore-filling methods, including pressure injection[121, 122], the vapor-liquid-solid (VLS) method [123, 124], the vapor-solid-solid (VSS) method [123, 125], pulsed laser deposition [126, 127], the sol-gel method [128–130], electroless plating [131] and electrochemical deposition (ECD, also referred to as electrodeposition).[33, 132–135]. For the purpose of synthesizing metallic nanowires, pressure injection has been evidenced as a feasible method [121, 136], but this method requires expensive vacuum and high-pressure techniques. VLS, VSS, pulsed laser deposition, and sol-gel methods are commonly used for semiconductor nanowires (NWs) such as SiNWs, GaAs NWs and ZnO NWs [122, 123], but seldom for metallic nanowires, either due to the expense of the processes or the challenge of synthesizing the proper precursor. Electroless plating might intuitively be thought to be economical and straightforward, but in actuality too many parameters need to be adjusted. To the best of my knowledge (through personal discussions and attendance at an international conference on the subject), no paper regarding template-assisted electroless plating of metallic nanowires has been published yet. In contrast, in the case of electrochemical deposition (ECD), which provides an direct electric pathway along the pores which have conductive bases, a wealth of materials (e.g. metallic and semiconductor nanowires) can be deposited by this method.[132–135, 137–144] Therefore, the simple, low-cost, and scalable electrochemical deposition method [58, 145], assisted by AAO templates, is the best choice and most powerful tool for synthesizing metallic nanowires.

3.1.1.2. Electrodeposition of Silver Nanowires into Anodic Aluminum Oxide (AAO) Template on Rigid Substrates

Among all metals, silver possesses the highest electrical conductivity [146], making it an ideal material as an electrode. Moreover, silver electrodeposition technique has been developed over a century and widely used in industry in products such as mirrors, decorative coatings and electronic components.[147] Most of these traditional silver electrolytes contain highly toxic cyanide and have a pH of over 10, since cyanide electrolytes are not stable in acidic conditions.[147] However, AAO templates are only stable at a pH between 5.0 and 8.2 [148–150], otherwise the AAO template will dissolve in the electrolyte, introducing impurities to the silver nanowires (AgNWs). Unfortunately, the role of pH in AAO template-assisted silver electrodeposition has been widely neglected.[151–155]

Only recently, Riveros et al. [149] have carefully studied the electrochemical mechanism of the ECD of Ag into AAO templates and contributed to two important points. First, they emphasize that the pH of their electrolyte is 6.0-6.5, which is in the working range of AAO templates (pH 5.0-8.2). However, although they observed that the color of the electrolyte changes from transparent to yellow during the electrodeposition process, they did not realize the color change was due to the quick decrease of pH to around 2.0. In my PhD work, I have solved this problem by adding a proper

buffer solution, described in detail in Section 3.3.1.1. Second, they clearly point out that silver nitrite ($AgNO_3$) solution is not an appropriate choice for filling AAO pores by electrodeposition, due to poorly electroformed metal. Although quite a number of published papers [156, 157] show the possibility of obtaining reasonable SEM images of AgNW arrays on a small scale with silver nitrite electrolyte, it is unlikely that large-area and high-quality AgNW arrays will be achieved with silver nitrite. In contrast, silver complex (e.g. $Ag(SCN)^3_{2-}$) solution, containing silver sulfite (Ag_2SO_4) and potassium thiocyanate (KSCN), results in fine-grained and smoother Ag, and therefore is desirable for ECD of AgNWs.[149, 158] Importantly, this solution is also non-toxic. Therefore, Ag_2SO_4 and KSCN are finally chosen for ECD of AgNWs in my PhD work.

In terms of AAO templates, they were first introduced by Keller at al. in 1953.[159] Much research was later conducted to improve the formation and to fabricate AAO pores with various distances and diameters using thick ($\sim$ mm) bulk Al foil.[85] Recently, it has been shown that the production of AAO templates on transparent conducting substrates such as ITO glass is also possible. However, due to the chemical instability of ITO [160], limited work has been performed using ITO substrate as base for the AAO templates.[161–165] Chu et al. [161, 162] initially fabricated AAO templates directly onto ITO glass. Unfortunately, this treatment resulted in a spontaneous breakdown of ITO film and delamination of AAO templates. This issue was resolved by Musselman et al. [163], who overcame these problems by inserting adhesive layers (a 5-50 nm of tungsten layer and a 5 nm of titanium layer), allowing for the fabrication of large-area free-standing Ni, Cu, Cu_2O and TiO_2 nanowire arrays. However, fabricating large-area Ag nanowire arrays on both the pure and W/Ti modified surface, resulted in extremely uneven filling of the template.

In my PhD work, I have found that the AgNW arrays can be achieved by adding an in situ oxygen plasma process and a Ti layer to enhance the adhesion between the AAO template and the ITO glass, by inserting Au as a nucleation layer. The experimental details and discussion can be found in Section 3.2.

3.1.2. Electrochemical Methods and Theory

3.1.2.1. Brief Introduction of The Electrochemical Mechanism

The most interesting part of the electrochemical reaction typically happens at the electrode/electrolyte interface. In general, the interfacial reaction process can be classified into two categories. One is the Faradic process, where charges (e.g. electrons) are transferred across the electrode/electrolyte interface. Electron transfer causes reduction or oxidation to occur. The other is the non-Faradic ("capacitor") process, in which no charge transfer occurs, but ion adsorption/desorption dominates.[166]

Faradic Process To keep the model simple, let us consider a metal-electrode/electrolyte interface, illustrated in Figure 3.1. If the electrode potential (Fermi level) is lower than

the highest occupied orbitals (HOMO) of the electrolyte ions (Figure 3.1a), the electrons will be thermodynamically unfavorable and therefore unlikely to jump from the electrode to the electrolyte solution. However, by applying an external potential, the Fermi level of the electrode can be shifted. For example, Figure 3.1c displays a upwards shift of the Fermi level, when exerting a negative potential. This is such that the electrons will become thermodynamically favorable and will be more likely to transfer from the electrode to the electrolyte ions. Simultaneously the reduction of electrolyte ions ("deposition") on the electrode will occur. The critical potential at which this electron transfer process occurs is related to the standard electrode potential[1], E_0, for the specific chemical substances in the system (Figure 3.1b).[109, 166, 167]

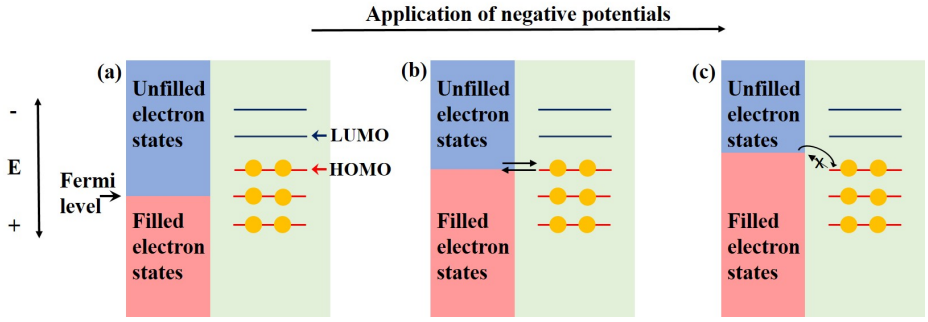

Figure 3.1.: Charge transfer at a metal-electrode/electrolyte-solution interface.

More generally, the redox potential under other conditions can be obtained by the Nernst equation:

$$E_{\text{redox}} = E_0 + \frac{RT}{zF}\ln\left(\frac{a_{\text{OX}}}{a_{\text{RED}}}\right) \tag{3.1}$$

where E_0 is the standard electrode potential, a_{OX} and a_{RED} are the chemical activities of the oxidized and reduced form of the substance, respectively. R is the gas constant, T is the absolute temperature, F is the Faraday's constant ($1F = 96485.3\,\text{C/mol}$), and z is the number of electrons involved in the redox reaction. Thermodynamically, the electrodeposition can proceed, when the applied potential (E) to the electrode is more negative than E_{redox} ($E<E_{redox}$) in case of a reduction, and $E>E_{redox}$ in case of an oxidation.[166, 168]

Furthermore, the amount of the electrodeposited materials can be quantified by the Faraday's first law [166]: "the amount of substance produced at an electrode is proportional to the quantity of electricity passed". The equation formula can be described

[1] Standard electrode potentials are given relative to the standard hydrogen electrode (SHE) under the conditions of $T = 298.15\,\text{K}$, $P = 1.01 * 10^5\,\text{Pa}$, and $c = 1\,\text{mol/L}$.

as:

$$n = \frac{Q}{zF} \tag{3.2}$$

where n is the amount of the substance produced at an electrode in mole, Q is the passed electricity in coulombs, z is the number of electrons involved in the redox reaction, and F is the Faraday's constant. This equation is practically useful for estimating the thickness of the electrodeposited materials.

Non-Faradic Process An electrical double layer (EDL) model is commonly used to describe the non-Faradic process, schematically depicted in Figure 3.2. Specifically, at the electrode/electrolyte interface there are two big regions of ion distributions. One is the Stern layer (or compact layer), which is closest to the electrode. And the other is the diffusion layer, where the solvated ions are diffused into a three-dimensional region driven by thermal motion. Moreover, based on different types of adsorbed ions, the Stern layer is further subdivided into two parts: i) between the electrode and inner Helmholtz plane (IHP), where so-called "specifically adsorbed ions" (i.e. usually anions, irrespective of the charge nature of the electrode) are strongly attached to the electrode; ii) between the IHP and outer Helmholtz plane (OHP), where there are "non-specifically adsorbed counterions". And from the OHP, the diffusion layer starts. In general, by exerting an electric field, the structure of the EDL can change through the adsorption/desorption process, resulting in the non-Faradic process.[166, 169]

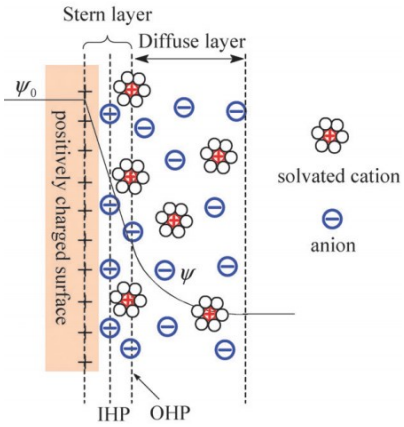

Figure 3.2.: An electrical double layer (EDL) model at an electrode/electrolyte interface. Reproduced from [169] with permission of The Royal Society of Chemistry.

3.1.2.2. Metal Electrochemical Deposition

Electrochemical deposition (ECD; also referred to as electrodeposition or electroplating) is a low-cost, fast and industry-applicable method. Moreover, ECD is easily adaptable for the fabrication of various nanomaterials (e.g. polymer, metal-oxide and metal).[170, 171] However, in this thesis, the focus is mainly on metal electrodeposition. A typical metal electrodeposition process consists of a series of steps [172, 173], illustrated in Figure 3.3.

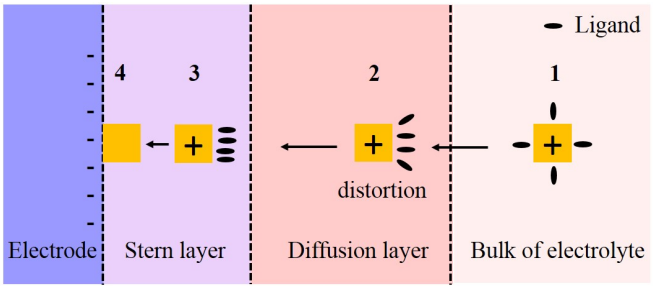

Figure 3.3.: A chematic illustration of a cathodic metal electrodeposition process.

- Step1 - mass transfer of the coordinated ions (e.g. $Ag(SCN)_3^{2-}$) through the bulk electrolyte to the diffusion region.
- Step2 - The ligand field becomes distorted in the diffusion region.
- Step3 - In the Stern layer, the metal ions are freed from their ligands.
- Step4 - The metal ions are neutralized. Hence, the metal is deposited on the cathode.

In terms of vertically aligned metallic nanowire fabrication, one can assume that, without any templates, nanowire could be obtained via electrodepositing metal on its seed layer. This is because the electric field between the metallic seed layer and the counter electrode is greater than that between the two electrodes, due to a shorter distance .[109] Therefore, growth is more possible on the seed layer. Furthermore, if the growth is favorable along only one direction, owing to a preferential crystal growth direction, vertically aligned metallic nanowires could be obtained. In fact, both ordered and disordered seed layers can be obtained by already mature techniques such as evaporating metal through the mask of a polystyrene sphere (PS) monolayer [100, 174] and the solution reduction approach [175]. However, fabrication of metallic nanowires without templates is hardly applied in practice since the growth control is very difficult. [109]

An example of this process is shown in Figure 3.4. A solution reduction approach was used to make silver seeds (diameter: 70-150 nm; height: ca. 20 nm) on ITO glass (Figure 3.4a). Consecutively, a potentiostatic deposition on the sample with the seed layer was employed. The results show that the nanoscaled silver seeds grow in three-dimensions into microscaled silver balls rather than wires (Figure 3.4b), indicating no

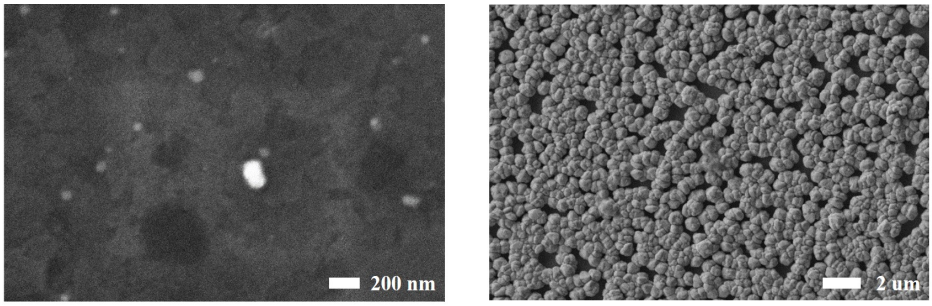

Figure 3.4.: (a) Silver seeds (bright dots) on a ITO glass (diameter: 70-150 nm). The seed layer was obtained by reducing silver nitrite with glucose (adding 100 μl of 0.5 M C6H12O6 (aq) into 100 μl of (0.1 M AgNO3(aq) + 0.8 M KOH(aq))). Afterwards, this mixture was left for 5 minutes, before being spin-coated on ITO glass at 200 rpm for 30 s. (b) Elctrodeposited silver on the silver seed layer with a deposition potential of -0.3 V vs. Ag/AgCl (3 M) after 2 min.

preferential crystal growth direction. Therefore, in order to achieve vertically aligned metal nanowires by electrodeposition method, templates with well defined channels (e.g. anodic aluminum oxide (AAO) template and block copolymer template) are necessary. In the following sections, the template-assisted electrodepositon of metallic nanowires will be discussed in detail.

3.1.2.3. Three-Electrode System

In most electrochemical experiments, a three-electrode system is adopted, and this is schematically illustrated in Figure 3.5. It consists of:

- A working electrode (WE): the electrode system of interest to this study.
- A counter electrode (CE): the electrode that assists current to pass between the WE and CE. It is worth noticing that the surface area of the CE is usually larger than the WE, to ensure that the half-reaction at the CE is fast enough not to limit the reaction process at the WE.[176]
- A reference electrode (RE): the electrode that remains a constant potential under changing conditions. Experimentally, the RE should be placed as close as possible to the WE to minimize the influence of the solution resistance R. If not, the R would cause a voltage drop iR (i is the current through a solution), resulting in a mismatch between the measured potential and actual potential on the WE.[176] In addition, there are different types of reference electrode such as Ag/AgCl, standard hydrogen electrode (SHE) and saturated calomel electrode (SCE). However, what reference electrode should be used depends on the properties of electrolyte (e.g. aqueous and non-aqueous) as well as the purpose of the study.

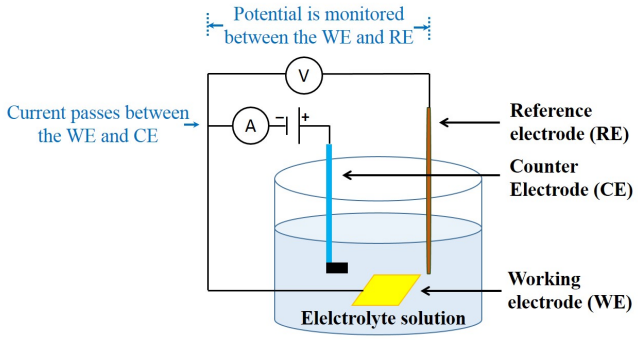

Figure 3.5.: Schematic demonstration of a three-electrode system.

3.1.2.4. Cyclic Voltammetry (CV)

Cyclic voltammetry (CV) is perhaps the most powerful tool for analyzing a new electrochemical system. Usually, a linear potential is scanned forward and backward between two values (i.e. V1 and V2), as shown in Figure 3.5a. The resulting current comes from redox reactions (Faradic current) as well as electrical double layer charging (non-Faradic current). One typical example is depicted in Figure 3.5b. This CV curve can be interpreted by considering the voltage and mass transport effects [166]:

- Stage 1 - In the beginning, the applied voltage is far away from the reduction potential (V0), no redox reactions happen and only non-Faradic current flows.
- Stage 2 - Upon reaching V0, the reduction process happens: O + e $\rightarrow$ R
- Stage 3 - The voltage becomes increasingly negative, resulting in the increasing current. The behavior of the current follows the Nernst equation (see in Section 3.1.2.1). Therefore, more reactant is converted.
- Stage 4 - The current reaches its peak, but also starts to decrease due to the depletion effect (i.e. the growing diffusion layer slows down the flux of the reactant to the electrode.[177]).
- Stage 5 - A reversed sweeping voltage is applied, the current begins to flow the other way (from the reactant to the electrode). The oxidation process occurs: R $\rightarrow$ O+e

If the reaction is ideally reversible, the CV curve could repeat round after round. However, the usual processes are not always reversible. Therefore, it is useful to calculate the cathodic to anodic charge ratio, by integrating the current over time, to determine the reversibility. It should also be noticed that the current changes with the varying scanning rate of the voltage.[177] For example, if the scan rate is slow, the diffusion layer near the electrode surface grows much further in comparison to a fast scan, therefore, the corresponding current decreases, and vice versa.

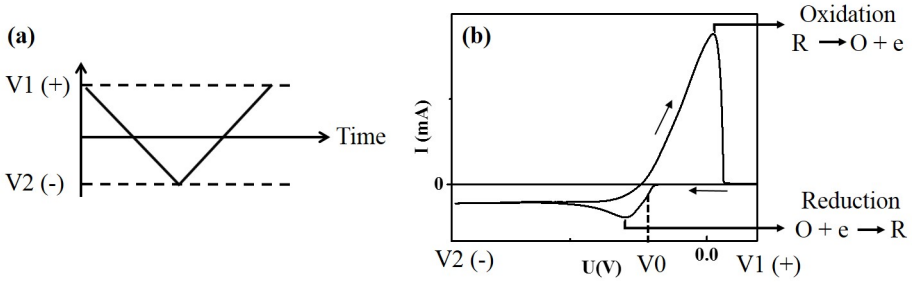

Figure 3.6.: (a) Applied potential vs. time. (b) A typical corresponding cyclic voltammetry curve.

3.2. Fabrication of Barrier-free AAO Templates on Rigid Substrates

3.2.1. Experimental Details

3.2.1.1. Sputter Deposition

Commercial ITO substrates (Praezisions Glas & Optik (PGO)) consist of a 180 nm thick ITO layer (approximately 10 Ω/sq) deposited on soda-lime-silica glass (14 x 14 x 1.1 mm). The substrates were cleaned in an ultrasonic bath for 10 min each with acetone and isopropanol prior to loading in the sputtering system. The sputtering system equipped with *in situ* oxygen plasma cleaning capabilities (AJA Orion 5) was typically pumped down to less than 2 x 10^{-7} Torr. The ITO substrates were cleaned with the *in situ* oxygen plasma cleaning process for 2 min at oxygen flow rate, power, and pressure of 15 sccm, 50 W and 10 mTorr, respectively. This cleaning process is crucial for enhancing the adhesion between ITO and subsequent layers. 99.95% pure Ti (5 nm) and Au (2 nm) were sputtered at a rate of 0.20 nm/s and 0.75 nm/s, respectively without breaking chamber vacuum. The Ti was radio frequency (RF) sputtered at a power and argon pressure of 100 W and 2 mTorr while the Au was direct current (DC) sputtered at a power and argon pressure of 20 W and 1.5 mTorr. The samples were subsequently taken out of the aforementioned sputtering system and transferred into the load lock chamber at 200°C for 5 min at approximately 10^{-5} Torr and then slowly cooled down to room temperature prior to being transported to the main chamber (Surrey NanoSystems Ltd.). This degassing process was used to remove the moisture bonded onto the sample surface due to breaking the vacuum. High-purity aluminum (99.999%)(150 nm) was DC sputtered at a power and argon pressure of 200 W and 5 mTorr with a rate of 0.05 nm/s. The Ti and Au targets were purchased from AJA International, Inc. and the Al target was purchased from Testbourne Ltd. All sputter were performed at room temperature. Commericial Si substrates (Active Business Company) is Boron-doped p-type with a crystal orientation of (100). There was no *in situ* oxygen plasma pre-cleaning process for Si substrates. The thickness of the sputtered Au layer was 30 nm. The other processes were exactly the same as those for the ITO substrates.

3.2.1.2. Anodization

The experimental setup for AAO anodization has been developed as shown in Figure 3.7. The setup is a two-electrode system in a jacketed beaker cooled by recirculating chiller. A power supply provided the constant anodizing potential, and a platinum wire ring (diam. 1 mm) counter electrode was placed in parallel to the Al film at a distance of 1-2 cm. For samples with ITO glass substrates, the power supply was Keithley 2400. The current was monitored throughout the anodization process by a self-written Labview program. For samples with Si substrates, the power supply was Easypower Supply EA-PS 8360-10 T, which provided higher output power (max. 1000 W; voltage accuracy <2%) than Keithley 2400 (max. 22 W; voltage accuracy <0.2%). The current was monitored by the incorporated program of the machine.

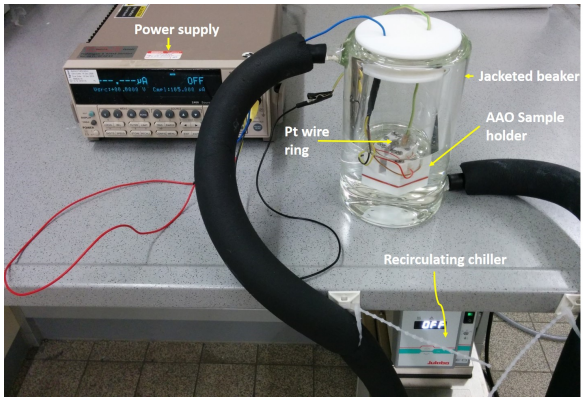

Figure 3.7.: Homemade anodization setup.

Figure 3.8 displays the homemade sample holder. It mainly consists of a Teflon container, which is inert to the used acid solution. The Al surface was pressed against a Viton O-ring, and the reverse of the substrate against a piece of silicone rubber, ensuring a leakage-free system. The samples were in contact with four gold pins, one at each corner, which provided a homogeneous current flow over the whole sample surface during the anodization process.

The anodization process was manually stopped, when vigorous gas bubbles uniformly spread out from the sample surface. It is important to stop the anodization process at the proper point because the barrier layer needs to be thinned for a sufficient duration, but the process should not be too long as this would damage the film.

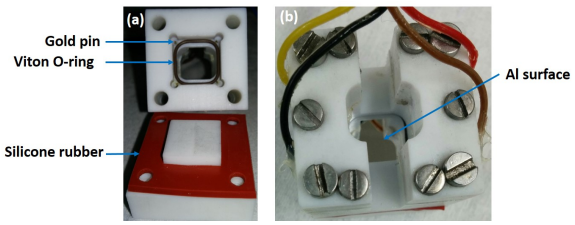

Figure 3.8.: The homemade leakage-free AAO holder

3.2.1.3. Pore-widening

The AAO pores widened in 5 wt.% phosphoric acid (Sigma-Aldrich) at room temperature. Meanwhile, the Al_2O_3 barrier layer beneath the pores was totally removed after a sufficient period of time. The pore widening time was typically between 35 min and 125 min, which depended on the anodizing voltages as well as the type of substrates.

3.2.1.4. Structural Characterization

The AAO templates were examined by SEM (see Chapter 2). The pore diameters, inter pore distances, and porosity were estimated by ImageJ software.

3.2.2. Results and Discussion

Figure 3.9 outlines the process used to fabricate the free-standing metallic nanowires. The mechanisms of the template formation and the electrodeposition are discussed in detail in the following sections.

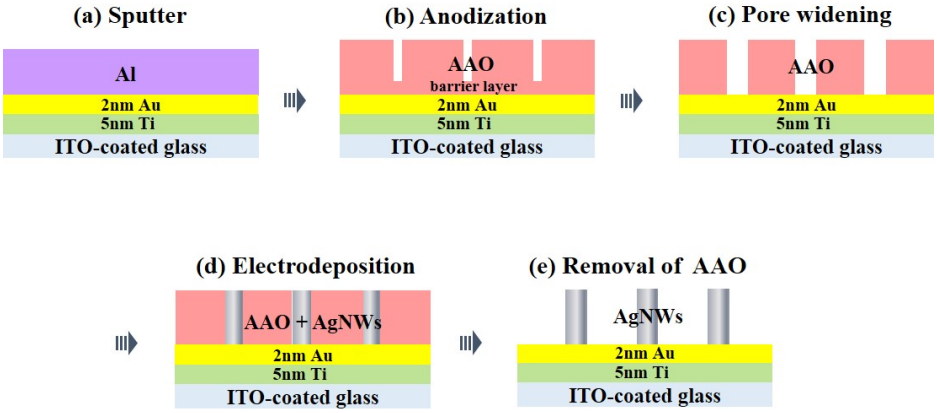

Figure 3.9.: Free-standing nanowire fabrication scheme.[33]

3.2.2.1. Critical Rule of Interlayers

Failed AAO Fabrication on ITO Glass without Interlayers

A 150 nm aluminum film was DC-sputtered on bare ITO glass. Attempts at anodizing the samples either at 40 V in oxalic acid or at 15 V in sulfuric acid encountered a severe peeling-off problem. Shortly after exerting a voltage, the corresponding current first decreased and then quickly jumped up, which caused rapid bubbling and peeling-off from the template. Only a small portion of the sample on the peeling-off edge turned transparent, which indicated the presence of AAO pores. This was then verified by SEM, as shown in Figure 3.10. However, a big portion (>80%) of the sample was shiny, indicating that most Al did not turn to AAO pores successfully.

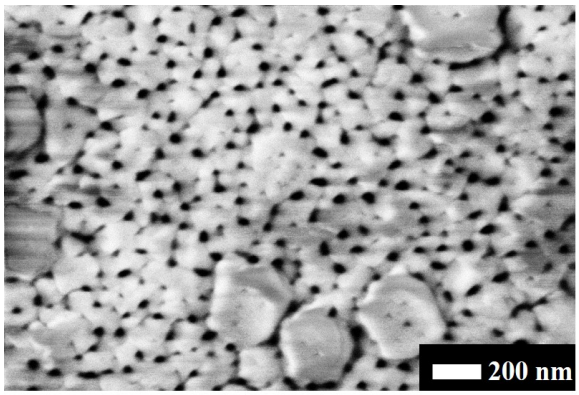

Figure 3.10.: SEM image of an AAO template on a bare ITO glass anodized at 40 V in oxalic acid. Only a small portion of the sample on the peeling-off edge had such transparent AAO template. The rest large area was till shiny Al.

AAO Fabrication on ITO Glass with Interlayers

Given the limited success of fabrication of AAO templates on bare ITO glasses, interlayers were used to greatly improve the quality of the AAO templates on ITO glasses. Experimentally, a 5 nm of Ti as an adhesive layer, 2 nm of Au and 150 nm of Al were deposited on ITO glass by sputtering. With such interlayers, the anodization process was slowed down, allowing the slower-forming pores to reach the bottom of the substrate without peeling-off of the film. Therefore, the Al film could turn entirely transparent over the whole substrate (with an area of 1.27 cm^2) without delamination (see Figure 3.11). Figure 3.12a shows an SEM image of a high-quality AAO template made by anodizing a 150 nm Al film on ITO glass at 60 V, followed by 80 min of pore-widening. The inset shows the pore diameter distribution. It is worth noticing that the in situ oxygen plasma pre-cleaning of the ITO surface is crucial for preventing the template from peeling off during the anodization process; high vacuum was maintained

between the pre-cleaning and the subsequent layer depositions. The ultrathin Au layer is transparent. Moreover this Au layer is not a continuous film but rather Au dots uniformly distributed over the ITO surface (see Figure 3.13). These Au dots are essential in providing nucleation sites for the silver electrodeposition (discussed in Section 3.3 in detail).

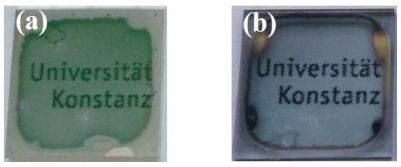

Figure 3.11.: (a) AAO template on ITO glass without pore-widening. (b) AAO template on ITO glass after pore widening.

To identify the stability of the ITO film in the anodization process, the sheet resistance was characterized by a four-point probe after removing the AAO template in NaOH (0.1 M) for 30 min. There was nearly no change between the remaining ITO (7.1 Ω sq^{-1}) and the pristine ITO film (6.9 Ω sq^{-1}).

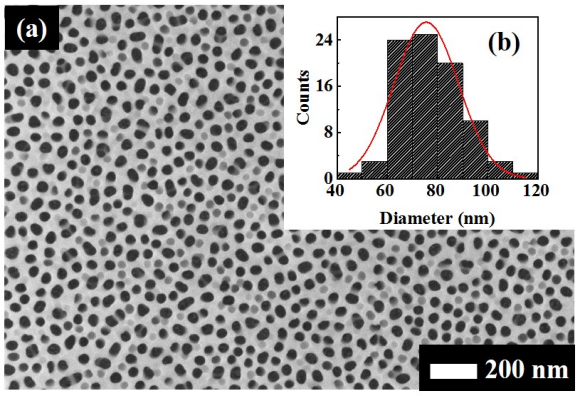

Figure 3.12.: (a) SEM image of an AAO template on an ITO glass substrate (with 5 nm Ti and 2 nm Au layers) by anodization in oxalic acid (0.1 M) at 60 V and pore-widening in 5 wt.% phosphoric acid for 80 min. (b) Pore diameter distribution: average pore diameter = 76 ± 13 nm, inter pore distance = 133 ± 15 nm and porosity = 5.5 x 10^9 cm^{-2}.[33]

3.2.2.2. Time-resolved Current Density of the AAO Anodization

Figure 3.14 shows a detailed plot of current density versus time (J-t) for the anodization at 60 V in 0.1 M oxalic acid. 0.1 M oxalic acid is used in this study instead of the more common 0.3 M oxalic acid [163] since the anodization process is too fast to stop in time when using the more concentrated acid for anodizating thin Al film. During the first

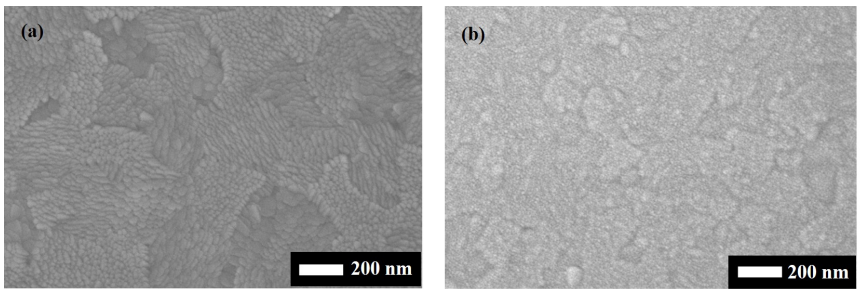

Figure 3.13.: SEM images of (a) a pure ITO glass surface, and (b) an ITO glass with 5 nm Ti and 2 nm Au. The ultrathin 2 nm Au is not a continuous film but Au dots distributed over the ITO surface.[33]

few seconds, a high current is detected while the surface of Al is oxidized. The current swiftly drops to a local minimum once the oxide layer is completely formed (1). The pores start to form due to local electric field enhancement induced by film roughness and cracks in the oxide layer.[163] The current increases during the progression of the pores through the Al film (2).

The subsequent significant current drop (3) is ascribed to a complete consumption of Al, first locally, and finally over the whole substrate, leaving an Al_2O_3 barrier layer at the bottom of the pores. At this point, the current reaches a local minimum (4). At the end of the anodization process, the current rapidly increases, accompanied by vigorous gas bubbles (5). These gas bubbles are likely due to the oxidation of O^{2-} ions, which migrate through the porous alumina barrier to the Au interface.[162] It is critical to stop the current at the proper point, because stopping too late would cause delamination of the template due to the pressure produced by the gas bubbles; however, since this process can also thin the barrier layer underneath the pores [162], stopping too early would leave too thick a barrier layer to be removed by 5 wt.% phosphoric acid. An example of the resulting product when the process is stopped too early can be seen in Figure 3.15.

3.2.2.3. Comparison of AAO Fabrication on ITO Glass and Si Substrate

The stopping current density thresholds, which should lead to a final barrier-free AAO template, varies significantly when the substrates are different (e.g. ITO glass vs. Si wafer). Figure 3.16a displays the J-t curve for the anodization of a 150 nm Al film at 40 V on a Si substrate. The stopping current density threshold (250 mA/cm^2) is approximately 20 times higher than that for ITO glass (12 mA/cm^2) under the condition of the same anodizing voltage (40 V). Such dramatic difference is attributed to the difference in surface roughness. Since the Si surface is much smoother ($R_{max} <$ 1 nm; R_{max}: maximum roughness) than ITO ($R_{max} < 5$ nm), the formed barrier layer

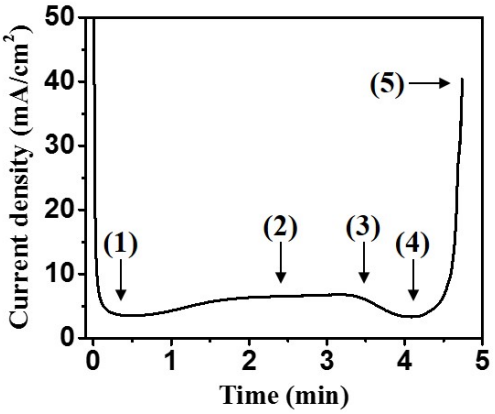

Figure 3.14.: Current density vs. time curve for the anodization at 60 V of a 150 nm Al on ITO glass (with 5 nm Ti and 2 nm Au layers) in oxalic acid (0.1 M).[33]

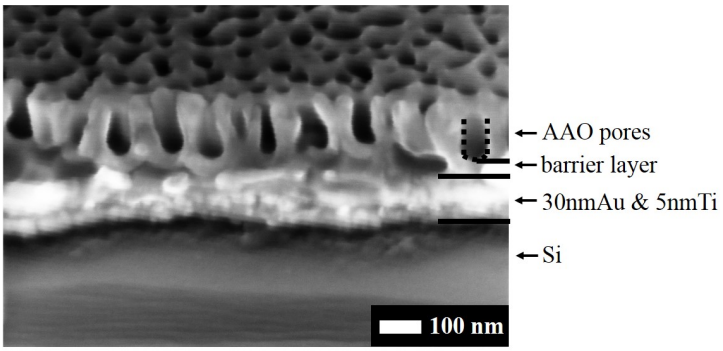

Figure 3.15.: Side view SEM image of an AAO template on Si substrate (with 30 nm Au and 5 nm Ti layers) by anodization in oxalic acid (0.1 M) at 40 V and pore-widening in 5 wt.% phosphoric acid for 30 min. Note that: This barrier layer hinders the electrodeposition into the AAO pores. However, if stopped at the right time, the AAO pores were opened at the bottom after the same pore-widening time (30 min) and successfully filled with Ag nanowires. This thinning barrier layer process is almost the same as on the ITO glass substrate.[33]

between the AAO pores and Si surface is more compact. Such a compact barrier layer needs higher electric field (higher current density) to be broken though. Figure 3.16b shows a top-view SEM image of a high quality and barrier-free AAO template on a Si substrate anodized at 40 V. The inset shows the pore diameter distribution (50±15 nm).

In order to highlight the crucial role of the surface roughness of the substrate, one extreme example is that the barrier-free AAO template was never successfully obtained when using a rougher ITO glass ($R_{max} < 35$ nm; purchased from LUMTEC, rather than from Praezisions Glas & Optik). The delamination of the AAO template on the rougher ITO started so early that barrier layer did not have sufficient time to be thinned.

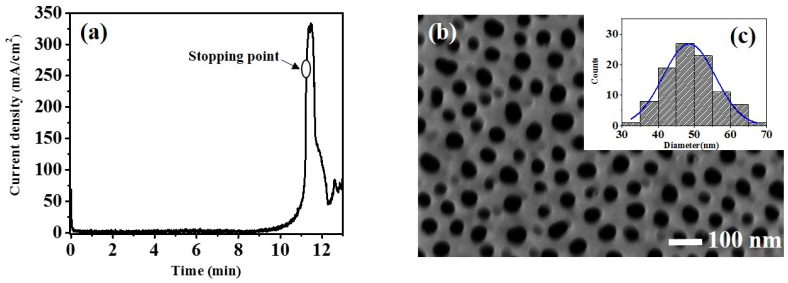

Figure 3.16.: (a) The current density vs. time curve for the anodization at 40 V of a 150 nm Al on Si substrate (with 5 nm Ti and 30 nm Au layers) in oxalic acid (0.1 M). (b) SEM image of an AAO template on a Si substrate after pore-widening in 5 wt.% phosphoric acid for 30 min. (c) Pore diameter distribution: average pore diameter = 50 ± 15 nm.

3.2.2.4. Anodization Voltage

Different voltages were used to anodize Al films to investigate the influence of this parameter. The stopping current density thresholds and pore widening times at different anodizing voltages (35 V, 40 V, 50 V and 60 V) are plotted in Figure 3.17 and summarized in Table 3.1.

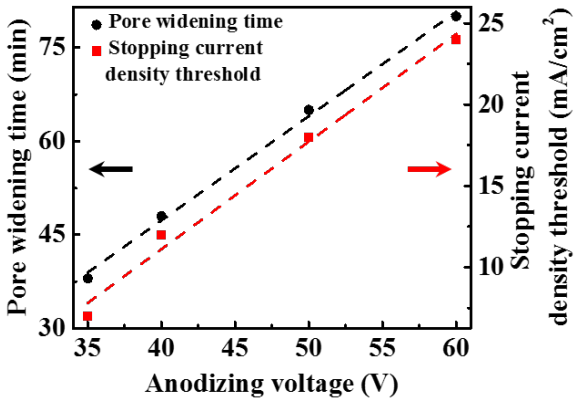

Figure 3.17.: Pore widening time and stopping current density threshold at different anodizing voltages.[33]

The AAO pores in this experiment were widened for a sufficient time so that the barrier layers at the bottoms were totally removed. Figure 3.17 shows that the stopping current density threshold and pore widening time are linearly dependent on the anodizing voltage. Since the barrier layer thickness linearly increases with respect to increasing anodizing voltage [178], higher electric currents to reduce the barrier layer thickness and longer pore widening times to completely open the bottom of the pores

Table 3.1.: AAO template parameters at different anodizing voltages. J: current density; PW: pore widening.[33]

Voltage (V)	Stopping J (mA/cm^2)	PW time (min)	Interpore distance (nm)	Pore diameter(nm)
35	7	38	84 ± 13	38 ± 3
40	12	48	96 ± 19	56 ± 13
50	18	65	112 ± 8	70 ± 5
60	24	80	133 ± 15	56 ± 13

are required. This linear relationship can help determine the stopping current density and pore widening time (see the equations below) at any anodizing voltage within the working range of the oxalic acid.

$$y_{\mathrm{SJ}} = 0.66x - 15.32; \qquad y_{\mathrm{PW}} = 1.67x - 19.54 \tag{3.3}$$

where x is the anodizing voltage, y_{SJ} is the stopping current density threshold and y_{PW} is the minimum pore widening time to completely remove the barrier layer.

The interpore distance and widened pore diameter at different anodizing voltage are examined from the SEM images (see Figure 3.18), and summarized in Table 3.1. It is found that the interpore distance depends linearly on the anodizing voltage with a proportionality constant of 1.9 nm/V (see Figure A1 in Appendix A). This agrees well with the reported data on conventional anodizing of bulk Al foils.[179]

However, the success rates of AAO templates formed at different anodizing voltages are not the same. At lower anodizing voltages, delamination of AAO film was occasionally observed. Higher anodizing voltages make the AAO formation process faster and reduce the occurrence of defects.[164] At 35 V to 40 V, the success rate was below 45%, whereas it increased to over 85% at 50 V to 60 V.

3.2.2.5. Overview of AAO Templates on Various Substrates

Except for acting as electrodeposition templates, AAOs on rigid substrates have numerous other applications. For example, such templates can be used for:

- Drug delivery through a sol-gel method of synthesizing SiO_2 nanotubes (cooperation with Dr. Xuecheng Chen, West Pomeranian University of Technology, Poland).
- Photophysics investigation of crystalline confined perovskite through AAOs (cooperation with Simon Bretschneider, Max-Planck-Institute for Polymer Research, Germany).

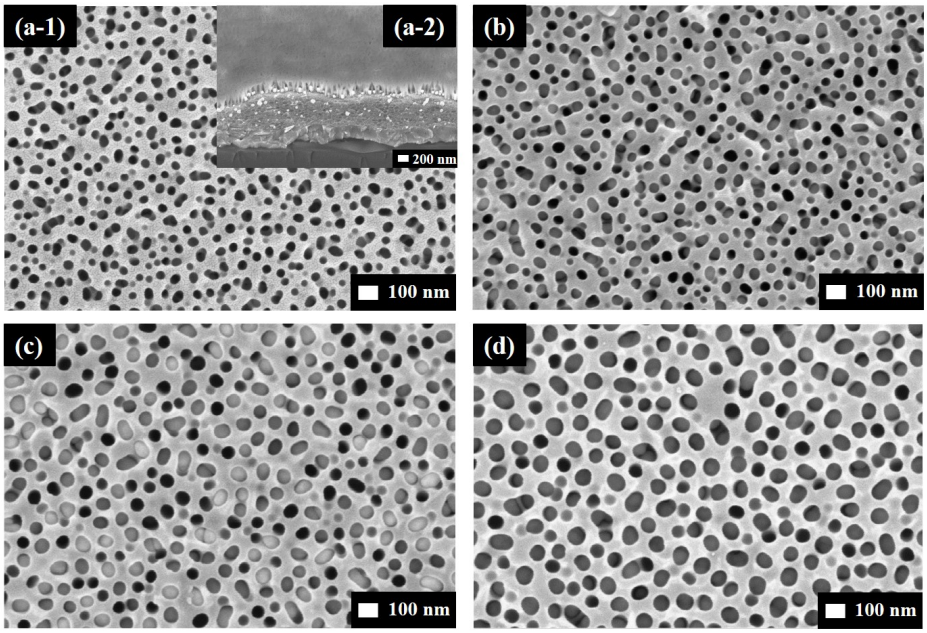

Figure 3.18.: (a-1), (b-d) are SEM top views of AAO templates filled with Ag nanowires at anodizing voltages of 35 V, 40 V, 50 V and 60 V, respectively. (a-2) is shown here since the Ag nanowires are too short to be seen from the top view.[33]

- Fabrication of nanostructures via laser-induced backward transfer method (cooperation with Matthias Feinaeugle, University of Southampton, UK).

For the aforementioned applications, the AAO fabrication process is easier since the barrier-free bottom is not essential, however different types of substrates are required. Table 3.2 gives an overview of which substrates are possible and which are not.

3.2.3. Conclusion

This study demonstrates the critical role of in situ surface plasma cleaning and interlayers (Ti and Au) for achieving well-attached barrier-free AAO templates on ITO glass. The stopping current point is important in the anodization process. Furthermore, dimension tunable barrier-free AAOs are obtained by varying the anodization voltages and linear regularities are found. Additionally, the possibility of AAOs on various substrates are provided, paving the way for many potential applications.

Table 3.2.: AAO template on different substrates. The diameter tuning range of different acids are [180]: sulfuric acid (D$\leq$ 65 nm), oxalic acid (D$\leq$ 100 nm), and malonic acid (D$\leq$ 300 nm).

Substrate	Sulfuric	Oxalic	Malonic
Glass (D263T; PGO)	work	work	work
Glass (Microscope Slides; Kittel)	failure	failure	failure
Quartz (PGO)	work	work	work
Si (B-doped (100); Active Business)	work	work	work
ITO (LUMTEC) with an interlayer of TiO_2(10-50 nm)	work	work	work
ITO (LUMTEC) with an interlayer of TiO_2($\geq$ 80 nm)	failure	failure	failure

3.3. Electrodeposition and Characterization of Metallic Nanowire Arrays

3.3.1. Experimental Details

3.3.1.1. Silver Electrolyte Preparation and Pulsed Electrodeposition

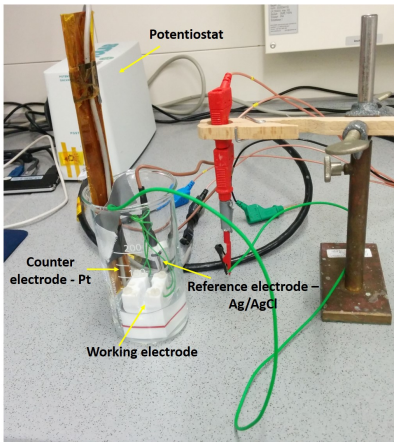

Figure 3.19.: Electrodeposition setup using a three-electrode system: AAO template (installed in the AAO holder) as a working electrode, Pt as a counter electrode and Ag/AgCl (3 M NaCl) as a reference electrode.

The pulsed electrodeposition was performed in a three-electrode system with an Autolab PGSTAT 101 Potentiostat/Galvanostat (see Figure 3.19). For Ag electrodeposition, the electrolyte solution was prepared using 50 ml of 0.05 M silver sulfate (Ag_2SO_4; Sigma-Aldrich) and 2.3 M potassium thiocyanate (KSCN; Sigma-Aldrich) in deionized water (pH 6.0). The pH of the solution was then adjusted to 4.2 by adding 40 ml of the acidic buffer 0.2 M monopotassium phosphate (KH_2PO_4; Sigma-Aldrich). Then, 20 ml of methanol was slowly added to the solution as a wetting agent. Finally, the pH of the

solution was stablized to 6.0 with 7 ml of the alkaline buffer 0.2 M dipotassium phosphate (K_2HPO_4;Sigma-Aldrich). The ratio of water to methanol in this electrolyte was about 1:5. The solution was stirred throughout the preparation process. The AAO samples was electrically connected as before in the leakage-free Teflon holder. An Ag/AgCl (3 M NaCl) electrode was used as a reference and a 2.25 cm^2 platinum counter electrode was employed. For pulse deposition, the following parameters were used: deposition voltage U_{pulse} = -0.5 V, pulse time t_{pulse} = 6 ms, relaxation voltage U_{off} = -0.157 V and relaxation time t_{off} = 1 s.

In addition, the electrodeposition of Au nanowires was also successful. The same pulsed electrodeposition concept was adopted: deposition voltage U_{pulse} = -0.7 V, pulse time t_{pulse} = 6 ms, relaxation voltage U_{off} = -0.157 V and relaxation time t_{off} = 1 s. The electrolyte solutions were prepared based on a recipe by Liew etal [173]: first, dissolve 0.42 M sodium sulphite (Na_2SO_3; Sigma-Aldrich) and 0.42 M sodium thiosulfate ($Na_2S_2O_3$; Sigma-Aldrich) together in deionized water. Then, slowly add 0.5 M chloroauric acid ($HAuCl_4$) to the solution while stirring.

3.3.1.2. Template Removal

The AAO templates were removed by etching in 0.1 M sodium hydroxide (NaOH; Sigma-Aldrich) for 30 min at room temperature. Subsequently, the samples were cleaned in deionized water, and dried carefully with a slight flow of nitrogen. Hence, free-standing Ag nanowire arrays on ITO glass were obtained.

3.3.1.3. Nanowire Characterization

The nanowire arrays were characterized using SEM (see Chapter 2) from top view and side view (angle of 54° with respect to the horizontal axis). The composition of nanowires was analyzed using XRD (see Chapter 2) and HR-TEM (high resolution transmission electron microscopy; JEOL, JEM 2200FS). Regarding the sample preparation for HR-TEM, the nanowires were scratched off the substrates and dispersed in absolute ethanol ($\geq$ 99.8%; Sigma Aldrich), before being suspended on a 400 mesh carbon-coated Cu grid.

3.3.2. Results and Discussion

Figures 3.9 d-e schematically illustrate the electrodeposition of silver into the AAO templates and the removal of AAO templates to obtain free-standing Ag nanowires.

3.3.2.1. Cyanide-free Electrolyte Development

To achieve uniform pore filling of Ag into the AAO pores, it is critical to choose a suitable electrolyte. Since cyanide electrolytes are not stable in acidic conditions, most traditional cyanide-based silver electrolytes are set to operate at PH $>$ 10.0. However, AAO templates are only stable at a pH between 4.0 and 8.0.[150] Considering the toxicity and poor compatibility with the AAO templates, it was necessary to develop a cyanide-free electrolyte.

Our previous attempts at using silver nitrate solutions were unsatisfactory as they resulted in poorly electroformed dendritic silver (see Figure B1 in Appendix B). Therefore, we chose to use a silver complex solution to obtain fine-grained and smoother Ag. The details of the silver electrolyte preparation are described in Section 3.3.1.1.

3.3.2.2. Overcoming the Challenges of Electrodeposition of Ag on Low-Surface-Energy ITO Glass

In order to form high-quality silver within the AAO templates on ITO glass, it is crucial to promote nucleation over the growth process. However, the nucleation of silver directly onto ITO glass is difficult because the low-surface-energy ITO is too smooth to allow the possibility of interlocking between the substrate and the electrodeposited silver.[181] It was observed that only sparse silver nuclei formed after a relatively long time of 10 min. To address this problem, various physical and chemical surface treatment methods were attempted, which are summarized in Table 3.3.

Based on the information in Table 3.3, homogenous electrodeposited Ag films could be successfully obtained by modifying the ITO surface through:

- Physical deposition of a thin metal or metal oxide film such as Au, Ag, and MgO, which have very small lattice mismatch with Ag ($<$3%). On the contrary, if the lattice mismatch is larger than 8%, the resulting electrodeposited Ag films are undesirable.
- Chemical grafting of a polar functional group (e.g. -SO_3, -COOH and -PO_3) onto the ITO surface. These functional groups should be well coordinated with the silver ions. If necessary, a cyclic voltammetry, scanning from 0.1 V to -0.5 V at 10 mV/s, could further promote nucleation over the growth process.

However, not all of these modified layers could be successfully incorporated to achieve high-quality AAO templates on ITO. For example, the thin Ag interlayer could not result in homogenous porous structures in an anodization process, likely due to the fast oxidation of Ag under a high potential (40 V). As shown before in Section 3.2.2.1, the problem of delamination was severe if fabricating AAOs on ITO glasses without interlayers. Therefore, post-treatments of the exposed ITO surface at the bottom of the AAO pores with chemical functional groups (e.g. -SO_3, -COOH and -PO_3) is invalid. Furthermore, MgO is unfavorable, because of its insulating property, which blocks to

Table 3.3.: Overview of electrodeposited Ag film quality after various surface pre-treatments. Note: in the table, CV refers to cyclic voltammetry, scanning from 0.1 V to -0.5 V with a scan rate of 10 mV/s; DPA refers to 1-decylphosphonic acid.

Surface treatment of the ITO glass (LUMTEC)	Results of the electrodeposited Ag
sputtered TiO_2 (5 nm)	inhomogenous Ag film
thermal evaporated Cr (5 nm)	severely incontinuous Ag film
thermal evaporated WO_3 (5 nm)	inhomogenous Ag film
sputtered Al_2O_3 (2 nm)	severely incontinuous Ag film
e-beam evaporated MgO (2 nm)	homogenous Ag film
sputtered Ag (5 nm)	homogenous Ag film
thermal evaporated Au (5 nm)	homogenous Ag film
spin-coated PEDOT:PSS (30 nm)	homogenous Ag film
30 min immersion in succinic acid (0.5 mM) without a CV	inhomogenous Ag film
30 min immersion in succinic acid (0.5 mM) with a CV	homogenous Ag film
30 min immersion in DPA(aq) (0.5 mM) without a CV	inhomogenous Ag film
30 min immersion in DPA(aq) (0.5 mM) with a CV	homogenous Ag film

some extent the contact between the Ag nanowires and ITO glass, interrupting the charge transfer process. Eventually, Au was found to be the most desirable material to act as a nucleation layer for Ag electrodeposition, and can also guarantee high-quality AAO templates.

3.3.2.3. Pulsed Electrodeposition and Morphologies of Nanowires

In order to determine the silver electrodeposition potential range, cyclic voltammetry was first performed on a flat gold film (30 nm Au on silicon substrate), as shown in Figure 3.20. It exhibits only one redox reaction in the potential range of -0.55 V to 0.1 V and the deposition peak for silver is -0.18 V. The anodic to cathodic charge ratio is close to 1, irrespective of the number of cycles. All potentials presented regarding electrodeposition in this paper refer to the Ag/AgCl (3 M NaCl) reference electrodes.

The pulsed electrodeposition of Ag into AAO pores is composed of modulated pulses in milliseconds (U_{pulse} = -0.5 V, t_{pulse} = 6 ms). An overpotential of -0.5 V was required instead of -0.18 V, because the bottoms of the AAO templates are more likely mesoporous alumina rather than fully exposed gold, which leads to higher resistivity than a pure gold. Therefore also the cyclic voltammetry curve should be shifted for AAO templates with a gold bottom rather than a planar gold film. A relatively long relaxation period subsequently takes place (t_{off} = 1 s with zero current at offset voltage applied of U_{pulse} = -0.157 V). A pulsed electrodeposition concept is adopted here for two reasons. First, it has been shown that pulsed electrodepostion can help achieve uniform and homogenous pore filling since a sufficient relaxation period assists the recovery of the silver ion concentration at the depostion interface.[182] Second, since the

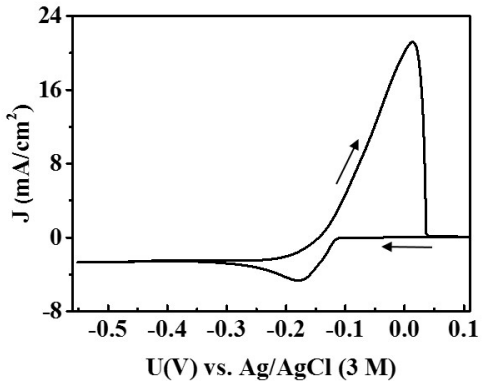

Figure 3.20.: Cyclic voltammetry of a gold electrode in the silver electrodeposition bath scanned from 0.1 V to -0.55 V. Scan rate: 10 mV/s. The anodic to cathodic charge ratio is 0.8074.[33]

silver electrodeposition rate is very high, to obtain short nanowires, the relaxation period of pulsed deposition can slow down the whole process. It is important to point out that prior to electrodeposition, the AAO templates are transparent. After electrodeposition, the surfaces become colorful (they change from brownish to purplish as the electrodeposition time is increased; one example is shown in Figure 3.26a). However, if the electrodeposition time is too long, the surfaces turn whitish, due to strong light scattering at the overgrown microstructured film. This change in the appearance of the surface of the AAO templates can be used to determine when a sufficient amount of silver has been deposited.

It is worthwhile to mention that potentiostatic deposition was tried previously, but after only a very short amount of time (< 1 s), the sample turned whitish, indicating extremely fast growth rate. Attempts at decreasing the temperature (ca. 1°C) did not effectively slow down the depositon rate. Moreover, decreasing the concentration of the electrolyte to reduce the deposition rate was not intuitively simple. When adding more water to the electrolyte, some "snow-like" compounds precipitated out, likely due to the change of the pH. Finally, the pulsed electrodeposition worked out as the most effective and controllable way to fabricate silver nanowires.

The crystal growth of the Ag nanowire arrays is shown by the X-ray diffraction (XRD; see Figure 3.21). The pattern shows the expected reflections for the silver material. Comparing the relative intensities of the silver reference pattern (JCPDS file No. 04-0783), one can conclude that the growth of Ag nanowires was successful. Additionally, HR-TEM studies further verify this conclusion (see Figure B2 in Appendix B).

Figure 3.22 displays side-view SEM images of the well-controlled different lengths of the Ag nanowires embedded in the AAO templates on ITO glass with increasing electrodeposition time from 5 s to 45 s. At times shorter than 10 s, only a few Ag nuclei

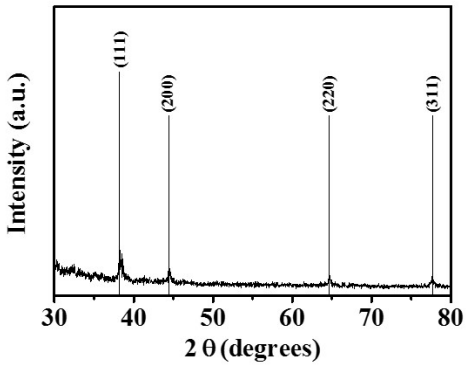

Figure 3.21.: An X-ray diffraction pattern of the Ag nanowire arrays embedded in an AAO template. Baseline noise is from the substrate and Al_2O_3.[33]

are observed as opposed to nearly full coverage after this critical time. Afterwards, the Ag uniformly deposits in the AAO pores resulting in Ag nanowires. All of the AAO templates discussed in Section 3.3.2.3 are anodized at 60 V, with an average diameter of 76 nm and an average interpore distance of 133 nm.

A prolonged current density versus time (J-t) pulsed electrodeposition curve is recorded, shown in Figure 3.23. The inset side-view SEM image displays the severe overgrowth of Ag nanowires. In the J-t curve, there are three main stages: I) transient stage for Ag nucleation; II) steady stage for Ag growing in the pores; III) increasing stage when hemispherical Ag caps start forming. This agrees with previously reported work on the electrodeposition of metal nanowires into polycarbonate membranes.[84] The process should be stopped at the transition point between stage II and III to obtain homogenous silver nanowires as overgrowth starts to dominate.

The length of the high-quality Ag nanowires, examined from the side-view SEM images of the samples, is linearly dependent on the charge collected on the sample, shown in Figure 3.24a. This agrees well with Faraday's law [62] and proves a uniform nanowire growth under the applied electrodeposition conditions. Since only a small portion of AAO pores are filled with Ag at the beginning of the electrodeposition, which is seen from the SEM image (Figure 3.22a), the examined length here is the average value of these few Ag nuclei. Therefore, the linear mapping starts at approximately 90 nm rather than 0 nm. In addition, this linear mapping can in turn be used to estimate the lenght of the Ag nanowires of good quality. Note that the same length of Ag nanowires is not necessarily obtained with the same electrodeposition time, since the current density always changes with different samples due to the inevitable fluctuations at the bottom of the AAO pores.

In rare cases, overgrowth of Ag nanowires happens even when the average length of

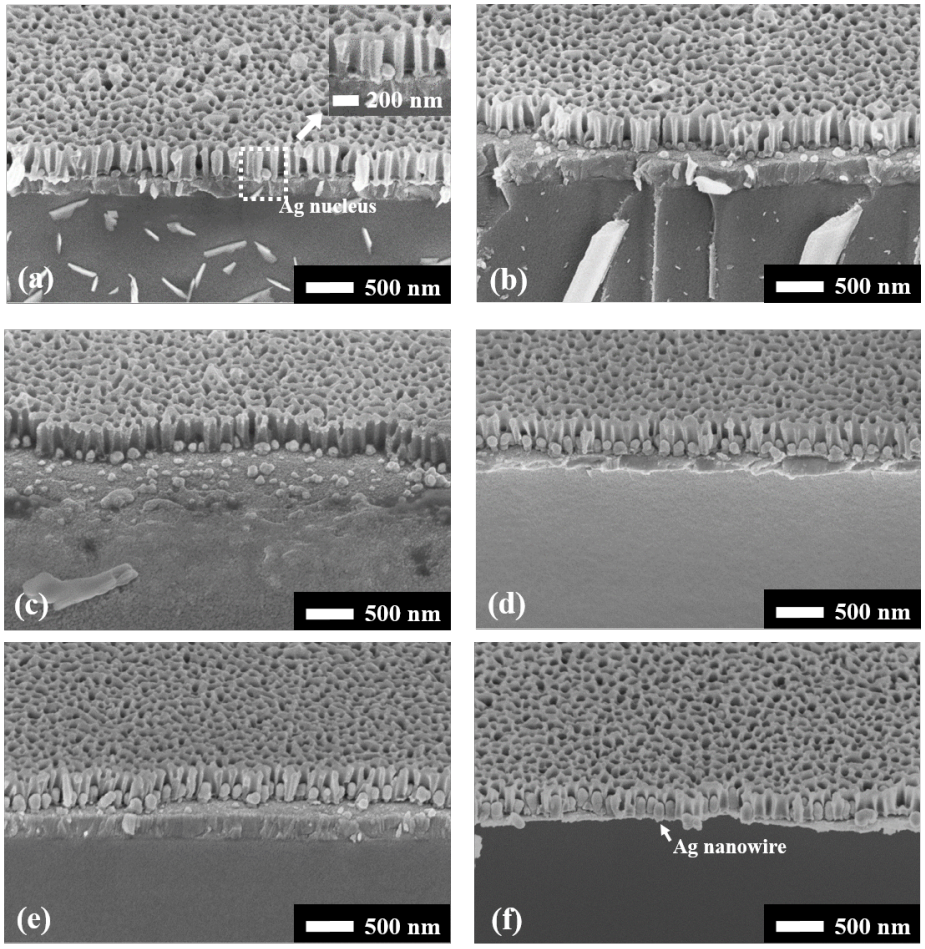

Figure 3.22.: SEM side view of electrodeposited silver nanostructures into AAO templates, anodized at 60 V, with an average diameter of 76 nm and interpore distance of 133 nm. The electrodepositing times and charges are: a) 5 s, 1.58 mC, b) 10 s, c) 15 s, 10.95 mC, d) 22 s, 33.64 mC, e) 30 s, 47.01 mC, and f) 45 s, 59.85 mC. The stage angle is $54°$.[33]

the Ag nanowires is still short. This is undesirable for certain device fabrications such as organic and hybrid solar cells because it causes an electrical short-circuit between the two electrodes. One poor quality Ag nanowire sample is presented in Figure 3.24a, which does not fit the linear relationship of the nanowire length and deposited charge. Its side-view SEM image is displayed in Figure 3.24b. It is assumed that this inhomogenous overgrowth is due to the uneven barrier layer at the bottom of the AAO pores. Hence, homogenous barrier layer quality of AAO templates is essential for uniform pore filling.

Figure 3.25 displays SEM images of the samples after removel of the AAO templates. The high quality of the Ag nanowires is shown in the lower magnification image of Figure 3.25a. The $90\,\mu^2$ area is uniform and free of collapsed nanowires, and is repre-

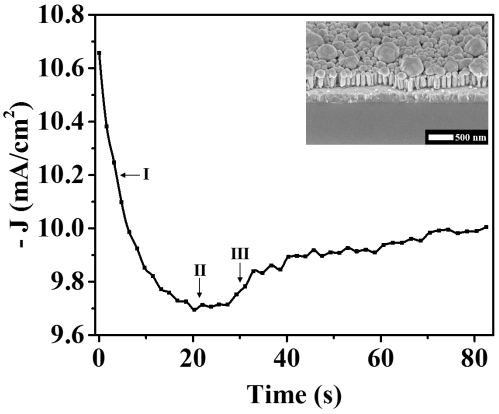

Figure 3.23.: Current vs. time curve for pulsed electrodeposition of silver into AAO templates on ITO glass. It displays the recorded data when the pulse is on, which mainly determines the silver nanowire growth.[33]

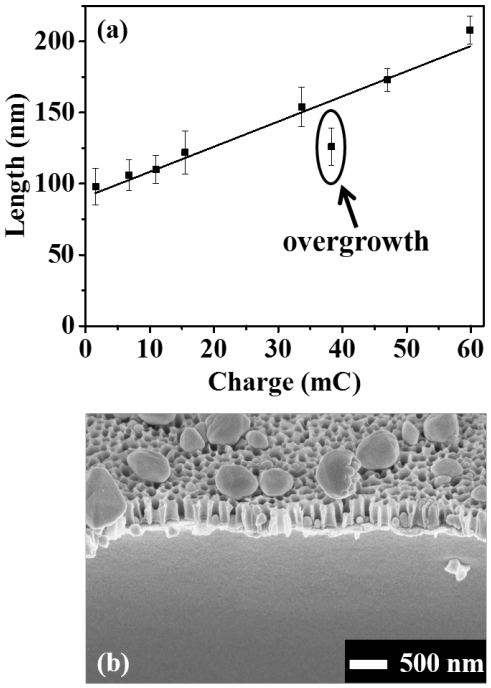

Figure 3.24.: (a) Mean and standard deviation of the silver nanowires' length with respect to the charge collected on the samples. The straight line represents a linear fit to the data. (b) A side-view SEM image of one overgrown silver nanowire sample embedded in the AAO template.[33]

sentative of the entire 1.27 cm^2 sample area (see Figure 3.26b).

Additionally, electrodeposition of gold nanowires has also been successfully achieved by using a similar pulsed electrodeposition method (experimental details are described in 3.3.1.1). The side-view SEM image of gold nanowires embedded in an AAO template is shown in Figure 3.27.

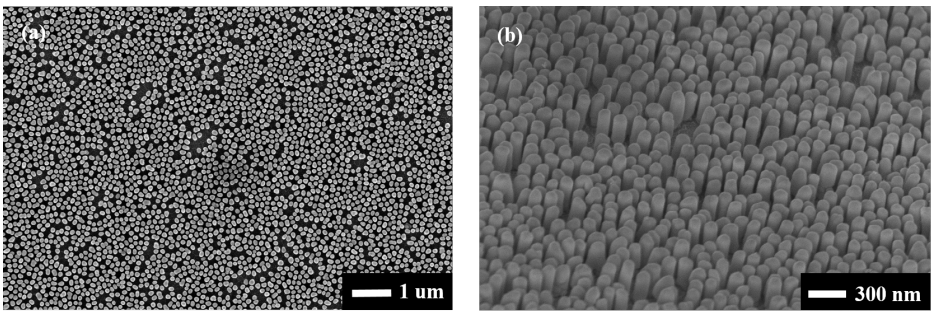

Figure 3.25.: SEM images of free-standing silver nanowires on ITO glass substrates: (a) top view, (b) side view at an angle of 54°.[33]

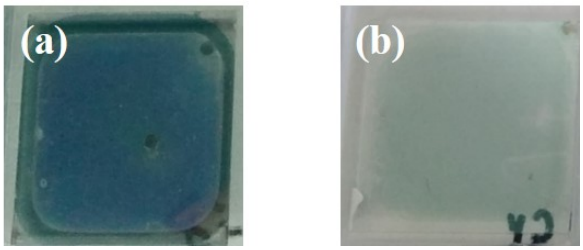

Figure 3.26.: (a) Silver nanowires embedded into the AAO template on an ITO glass. (b) Free-standing Ag nanowires after removal of the AAO template on an ITO glass. These two samples were fabricated with the same parameters in the same batch.

3.3.3. Conclusion

In summary, in order to achieve a successful growth of AgNWs into AAO templates by an electrodeposition method, a novel cyanide-free silver electrolyte based on silver-sulfate complex has been developed, which is compatible with the AAO templates, and more importantly, is stable long term. Furthermore, the ultrathin gold layer is found to be a desirable nucleation layer for the electrodeposition of Ag nanowires. The length of the Ag nanowires can be estimated from the linear mapping of the length versus collected charge. However, the length of the Ag nanowires is not linearly dependent on the electrodeposition time, because the electrodepositing current density always changes with different samples due to the inevitable fluctuations at the bottom of the

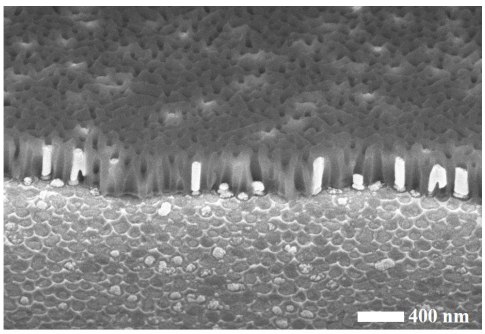

Figure 3.27.: A side view SEM image of gold nanowires embedded into an AAO template, anodized at 60 V, with an average diameter of 76 nm and interpore distance of 133 nm. The electrodeposition time is 30 s. The stage angle is 54°.

AAO pores. In addition, gold nanowire arrays have been also successfully obtained using the AAO templates and pulsed electrodeposition concept.

3.4. Optical Properties of Metallic Nanowire Arrays

3.4.1. Ultra Violet-Visible Light (UV-Vis) Characterization of Free-Standing Silver Nanowires

The optical properties of free-standing AgNWs were examined by a UV-Vis-NIR spectrometer with an integrating sphere. Figure 3.28 shows the absorbance for different lengths of Ag nanowire arrays at an incident angle of 25°. For each length of Ag nanowire arrays, there are two distinct peaks: one is related to transverse resonance of the Ag nanowires; the other is at the longer wavelength and is associated with the longitudinal axis of the Ag nanowires.[183] With diameter remaining almost constant, the transversal peak stayed nearly the same at 370 nm. However, with length increasing from 183 nm to 212 nm, the longitudinal peak red shifts considerably by 52 nm and its absorbance decreases by 20%. It is expected that this reduction in absorbance for the 212 nm nanowires originates from the lower AgNW density in comparison to the 183 nm nanowires. This indicates that by changing the dimension of the silver nanowires, the resonance peaks can be tuned in the UV-Vis range to, for example, meet the needs of enhancing the electromagnetic field at specific wavelengths in the applications in SERS, biosensing and many other areas.

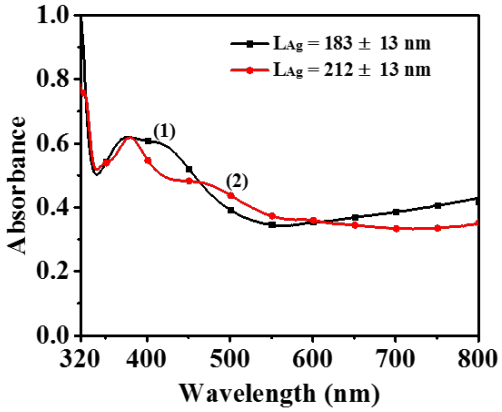

Figure 3.28.: Absorption spectra at an incident angle of 25° of free-standing Ag nanowires with diameter = 76 ± 13 nm, interpore distance = 133 ± 15 nm. (1) length = 183 ± 13 nm, aspect ratio = 2.2, (2) length = 212 ± 13 nm, aspect ratio = 2.6.[33]

3.4.2. Surface Enhanced Raman (SERS) Effects of Silver Nanowire Arrays

The Raman experiments were preliminarily examined by the Raman setup equipped with a 488 nm laser from the group of Prof. Maret, University of Konstanz. Benzenethiol (BT) was used as a Raman probe. The AgNWs embedded in AAO templates on Si substrate (AgNWs-AAO; diameter: 60 nm, interpore distance: 100 nm, AgNW-length: 200 nm) was first etched in 0.1M NaOH for 30 s, and then immersed in 1 mM ethanolic benzenethiol (BT) solution for 15 min, followed by Raman test. Next, the same sample was further immersed in 1 mM ethanolic BT solution for plus 180 s (total 210 s), and then followed by Raman test.

The SERS spectra of BT adsorbed AgNWs-AAO on Si substrate with etching times of 30 s and 210 s are shown in Figure 3.29. We can see the characteristics of BT at 996, 1020, 1075, 1574 cm^{-1}, where are consistent with the reported data in the previous literature.[184–187] As the etching time increasing from 30 s to 210 s, the Raman intensity increases $\sim$ 3-fold. This is resulted from larger exposed AgNW surface to BT with increasing etching time. However, this preliminary test cannot tell much about the localized surface plasmon (LSP) induced Raman enhancement, since the wall-to-wall distance in this system is $\sim$ 40 nm, much larger than the typical gap dimension of the hot spot $\sim$ 2 nm.[188–195] Therefore, further research needs to be done regarding reducing the wall-to-wall distance. Two approaches are suggested: first, increasing the pore-widening time for AAO templates; second, sputtering Ag on free-standing AgNWs. It is very promising to use this AgNW-AAO system to systematically investigate the relationship between the LSP and SERS by tunning the gap dimension in a controllable way. Moreover, this AgNW-AAO SERS system is robust, reproducible and immune to contamination until it is ready to use [185].

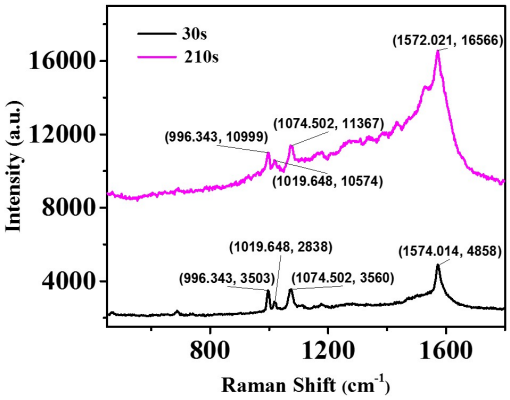

Figure 3.29.: Surface-enhanced Raman scattering (SERS) spectra of benzenethiol adsorbed AgNWs-AAO on Si substrate (diameter: 60 nm, interpore distance: 100 nm, AgNW-length: 200 nm). The AgNWs-AAO is etched in 0.1M NaOH for 30 s and 210 s, respectively. The excitation wavelength is 488 nm and the acquisition time is 2 s.

3.5. Summary and Future Work

In this chapter of the thesis, a novel processing route for the fabrication of free-standing uniform noble (e.g. Ag and Au) nanowire arrays on ITO (and other) substrates has been developed. In particular, free-standing AgNWs on ITO glass has been studied in detail. In situ oxygen plasma cleaning of the ITO surface and the sputtered Ti layer provide excellent adhesion during the anodization process. The ultrathin gold layer (2 nm) is found to be a desirable nucleation layer for the electrodeposition of Ag. Furthermore, a stable cyanide-free electrolyte compatible with the AAO templates is developed. The diameter of the Ag nanowires, and the separation between them can be controlled by the AAO template. The length can be estimated from the linear curve of the length versus collected charge.

In terms of optical properties of the Ag nanowire arrays, they present tunable plasmon resonance effects in the UV-Vis region. Furthermore, the preliminary Raman measurement paves the way for the promising SERS application in the future.

4. Solar Cells Based on Nanostructured Electrodes

In this chapter, the free-standing silver nanowires are quasi-conformally coated with a ZnO shell, forming a hybrid metal-semiconductor core-shell nanowire array electrode. This electrode is then integrated into both of a traditional opaque and semi-transparent bulk heterojunction organic solar cells. Furthermore, the in-depth investigation of the device physics in terms of external quantum efficiency, charge collection, and recombination indicate a clearer general design route for ultimately achieving highly efficient and low cost solar cells.

4.1. Optimization of Flat Organic Solar Cells

Basic Organic Solar Cell Fabrication The architecture of flat organic solar cells is schematically shown in Figure 4.1. The ITO-coated glass substrates (LUMTEC; 15 Ω/sq) were cleaned in an ultrasonic bath of dish-washing detergent, acetone, and isopropanol for 10 min successively and dried with nitrogen. Then, they were treated with oxygen plasma for 7 min. After that, a 0.5 M ZnO sol-gel solution was spin-coated on top. The solution was prepared by dissolving 0.328 g zinc acetate ($[Zn(CH_3COO)_2 \cdot 2H_2O]$; Sigma-Aldrich) in 3 ml of 2-methoxyethanol (Sigma-Aldrich) solvent containing 100 ul of ethanolamine (Sigma-Aldrich) as a stabilizer. Then, the samples were heated at 250°C for 10 min in the air. After the samples cooled down to room temperature, P3HT:PCBM (P3HT - Rieke, M_W=69 kDa; [60]PCBM - Nano · C; P3HT:PCBM=1:0.8 by weight ratio) dissolved in organic solvent was spin-coated on the ZnO layer, followed by thermal annealing. Finally, a 5 nm of WO_3 layer and a 120 nm of Ag were thermally evaporated consecutively on top of the organic film.

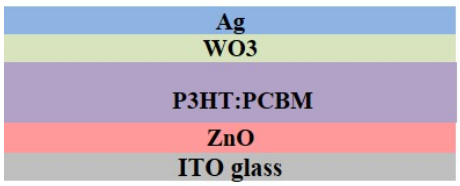

Figure 4.1.: Architecture of flat organic solar cells.

ZnO Layer Adjustment ZnO layer is used as a selective electron transport layer in the solar cells. The thickness of ZnO needs to be carefully controlled, because it needs to be thick enough to fully cover the ITO surface to prevent current leakage, but a too thick ZnO layer will decrease the solar cell performance. On the one hand, a thicker film might have a rougher morphology, leading to worse contact between the ZnO layer and active layer, which will result in an increased sheet resistance.[196] On the other hand, as the ZnO layer also acts as an optical spacer [197–199], its thickness would affect the spacial distribution of the optical electric-field in the device. In this study, the thickness of the ZnO layer is adjusted by changing the spin-coating speed (usually higher spin-coating speed leads to thinner film). In particular, two-step spin-coating was performed (i.e. spin-coating one layer, then annealing at 250°C for 10 min, then spin-coating the second layer, and finally annealing at 250°C for 10 min), which is assumed to have a better coverage on the ITO surface than one-step spin-coating. Note that the thickness range of the ZnO layer is 30-60 nm, verified by SEM.

In Figure 4.2, the influence of the ZnO layer thickness on the solar cell performance is displayed. The maximum power conversion efficiency (PCE) shows 1.962% under this spin-coating condition: 4000 rpm for 40 s + 2000 rpm for 40 s; acceleration 1000 rpm/s. If the layer is too thin ((6000 rpm + 4000 rpm) or (6000 rpm + 2000 rpm)), the photocurrent density and open-circuit voltage decrease significantly, which is assumed to be due to only partial of the ITO surface. However, if the layer is too thick (2000 rpm + 2000 rpm), the fill factor and photocurrent decrease slightly, which is assumed to be due to rougher ZnO surface as well as less than perfect optical electric-field distribution in the device.

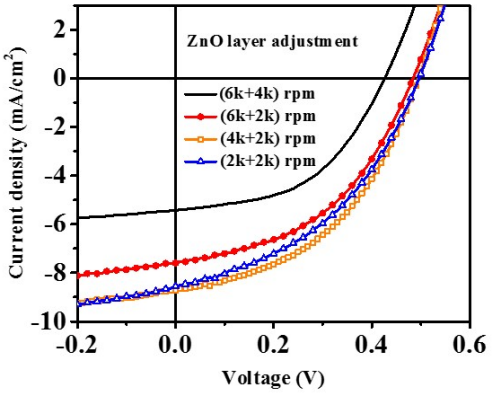

Device Description	PCE (%)	FF (%)	V_{oc} (V)	J_{sc} (mA/cm²)
(6k+4k) rpm ZnO	1.137	49.1	0.4263	5.429
(6k+2k) rpm ZnO	1.679	45.4	0.4843	7.594
(4k+2k) rpm ★ ZnO	1.962	45.1	0.4954	8.735
(2k+2k) rpm ZnO	1.812	42.3	0.4964	8.562

Figure 4.2.: Influence of ZnO layer thickness on device performance.

Active Layer Adjustment

Influence of Solvent The choice of the organic solvents is crucial for the device perfor-

mance, since evaporation rate directly affects the morphology of the active layer.[200] So far, the most commonly used solvents for P3HT:PCBM are chlorobenzene (CB; boiling point: 131.0°C) and 1,2-dichlorobenzene (DCB; boiling point: 180.5°C). However, there is no universal conclusion as to which solvent is the best.[201, 202] For a new device architecture and fabrication environment, comparative experiments needed to be conducted to decide the best solvent. Specifically, a 54 mg/ml solution of P3HT:PCBM in CB and DCB were prepared, respectively. They were spin-coated at a rate of 1000 rpm for 1 min with 500 rpm/s acceleration, and then annealed by raising the temperature from 60°C to 125°C in the air. The device performance is shown in Figure 4.3. Apparently, CB performs overwhelmingly better than DCB. CB shows better photocurrent density and open-circuit voltage, which is assumed to be due to a better crystallinity of P3HT as well as a superior phase separation [203] between P3HT and PCBM.

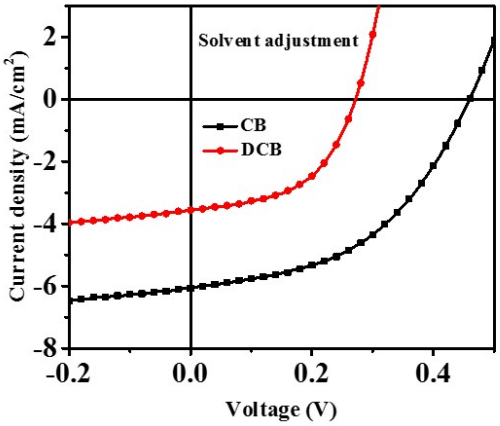

Device Performance	CB	DCB
PCE (%)	1.296	0.4556
FF (%)	46.8	49.8
Voc (V)	0.4594	0.2578
Jsc (mA/cm²)	6.069	3.546

Figure 4.3.: Influence of the solvent on device performance

Influence of Thermal Annealing It was found that the device performance could benefit from a thermal annealing treatment after spin-coating the active layer, mainly due to the increase of photocurrent density and fill factor. It is expected that with thermal annealing PCBM strongly diffuses through the softened P3HT matrix and forms an efficient percolation paths, promoting charge transfer.[13, 200, 204] Comparative experiments of annealing the P3HT:PCBM layer before and after the electrode deposition were conducted. The results are that pre-annealing always yields better PCE than post-annealing.

Furthermore, the influence of pre-annealing on the solar cell efficiency is summarized in Figure 4.4. We can see that:

- For a constant temperature treatment in the air (No.1 - No.5), a maximum in efficiency is found when using a temperature of 125°C with a duration of 5 min (No.4). A higher temperature (140°C) tends to decrease the overall efficiency dramatically.

- For a rising temperature treatment in the air (No.7 - No.9), a maximum efficiency is obtained by raising the temperature from 60°C to 110°C (Stuart hotplate), and then naturally cooling to room temperature (No.7).
- For a rising temperature treatment in nitrogen glovebox (No.10 - No.11), a maximum efficiency is achieved by raising the temperature from 60°C to 140°C (Stuart hotplate), and then naturally cooling to room temperature (No.11).

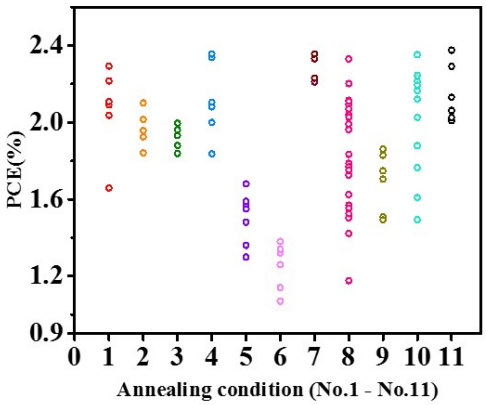

No.1 - 110°C 5 min	No.7 - rising from 60°C to 110°C in air
No.2 - 125°C 1 min	No.8 - rising from 60°C to 125°C in air
No.3 - 125°C 3 min	No.9 - rising from 60°C to 140°C in air
No.4 - 125°C 5 min	No.10 - rising from 60°C to 125°C in GB
No.5 - 140°C 5 min	No. 11 - rising from 60°C to 140°C in GB
No.6 - 140°C 10 min	note: GB is glovebox

Figure 4.4.: Influence of the thermal annealing on device performance. Eleven different annealing conditions are described in the right-hand table.

Overall, either No.4 or No.7 or No.11 can lead to nearly the same maximum PCE. Interestingly, if we compare No.11 with No.7, it needs higher temperature (140°C) in the nitrogen glovebox than in the air (110°C). This is presumed to be due to different evaporation rates of solvents in different environments, that is, in a glovebox the ventilation is slower than that in the air in a fume hood, resulting in a slower evaporation rate of solvents. Therefore, the annealing needs longer duration and higher temperature in the glovebox to form the best nanomorphology. Finally, it is preferable to choose No.11 as the optimized condition to get more reproducible devices, since the humidity is much more stable in the glovebox than that in the air.

Influence of Thickness Generally, a thicker active layer absorbs more photons. However, due to the low charge carrier mobilities in organic polymers, the layer needs to be thin enough to minimize recombination.[205] Additionally, in multilayer devices, the optical interference between the incident light and light reflected from the Ag back electrode could also play a big role. It has been demonstrated that such optical interference leads to an oscillatory behavior in the total absorption in the device as a function of the active layer thickness.[13, 206–209] Given these reasons, the active layer thickness needs to be optimized to reach a maximum PCE.

The thickness of the active layer was varied by changing the concentration of the blend polymer, while keeping the spin-coating conditions the same (1000 rpm for 1 min with

500 rpm/s acceleration). As seen from Figure 4.5b-c, the high concentration (54 mg/ml) results in a 400 nm layer, and the low concentration (27 mg/ml) results in a 120 nm layer. The measured J-V characteristics for the solar cells is displayed in Figure 4.5a. With thickness decreasing from 400 nm to 120 nm, the FF significantly increases and also the V_{OC} slightly increases, due to a lower series resistance of the thinner active layer. But the J_{SC} decreases a bit mainly due to the decreased absorption. Overall, the PCE increases by 18%. Hence, the PCE of our final optimized champion solar cell reaches 2.779%.

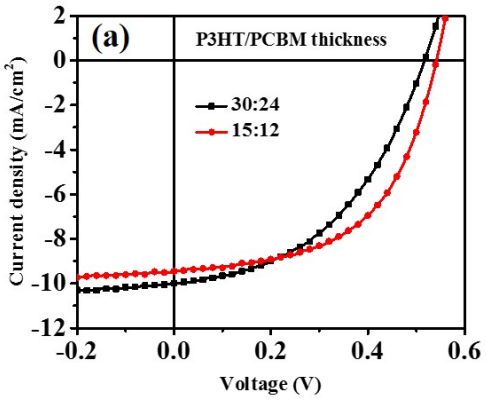

Device Performance	30:24	15:12
PCE (%)	2.352	2.779
FF (%)	45.7	54.5
Voc (V)	0.5172	0.5418
Jsc (mA/cm²)	9.994	9.454

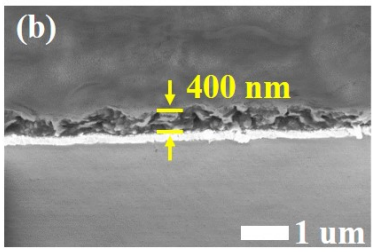

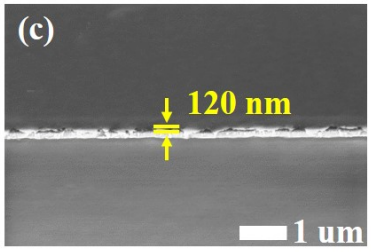

Figure 4.5.: (a) J-V characteristics of the solar cells with different thicknesses of P3HT:PCBM. (b) Cross-section SEM image of a P3HT:PCBM layer produced by spin-coating a 54 mg/ml solution. (c) Cross-section SEM image of a P3HT:PCBM layer produced by spin-coating a 27 mg/ml solution.

In summary, the optimized conditions were found to be as follows:

1. ZnO spin-coating conditions: 1st step - 4000 rpm for 40 s with 1000 rpm/s acceleration, then anneal in the air at 250°C for 10 min; 2nd step - 2000 rpm for 40 s with 1000 rpm/s acceleration, then anneal in the air at 250°C for 10 min.
2. solvent: chlorobenzene.
3. thermal annealing conditions: raising the temperature from 60°C to 140°C (Stuart hotplate), and then naturally cooling to room temperature in the nitrogen glovebox.
4. thickness of the active layer: 120 nm.

4.2. Preparation of Core-Shell Silver Nanowire Organic Solar Cells

Device Architecture and Final Fabrication Process

A schematic illustration of the fabrication process for free-standing silver nanowire-based organic solar cells is shown in Figure 4.6a-c, along with the SEM images (Figure 4.6d-f). Both opaque solar cells and semi-transparent solar cells have been successfully fabricated. Specifically, the free-standing AgNW electrodes (Figure 4.6d) were obtained by dissolving nanowire-embedded AAO templates in 0.1 M NaOH for 50 min. Immediately after, they were immersed in deionized water, ethanol (Sigma-Aldrich; purity $\geq$ 99.8%) and isopropanol (Sigma-Aldrich; purity $\geq$ 99.8%) consecutively, and then dried carefully with a slight flow of nitrogen.

Then, four cycles of spin-coating were performed, using a 0.5 M ZnO sol-gel solution (i.e. drop 40 ul of ZnO sol-gel solution on the AgNW sample, and wait for 1 min, then spin-coat at 5000 rpm for 40 s with 1000 rpm/s acceleration, then anneal it at 250°C for 10 min. Repeat this process for four cycles). The ZnO coated AgNWs core-shell structures are shown in Figure 4.6e.

As can be seen from the SEM image, the diameter of the core-shell nanowire is larger than the pure AgNW, indicating a successful quasi-conformal coating process of ZnO on AgNWs. After the samples cooled down from 250°C to room temperature, they were wetted in chlorobenzene for 4 min. Then a P3HT:PCBM (weight ratio of 1:0.8) solution, 54 mg/ml or 45 mg/ml in chlorobenzene, was spin-coated on top. The spin-coating process consisted of two steps: 1) spin-coat at a very low speed with 50 rpm (acceleration of 50 rpm/s) for 2 min, in order to fully infiltrate into nanowire arrays; 2) spin-coat at a high speed with 1500 rpm (acceleration of 500 rpm/s) for 1 min to form a homogenous film. The success of polymer infiltration is indicated by a cross-sectional SEM image in Figure 4.6f.

Finally, for opaque solar cells, a 5 nm of WO_3 and a 120 nm of Ag were thermally evaporated at a base pressure of around 10^{-6} mbar as a top electrode. For semi-transparent solar cells, a multilayer of MoO_3 (3 nm) /Al (1 nm) /Ca:Ag (mixing ratio 2:1; 9 nm) /Alq_3 (60 nm) electrode was thermally evaporated at a base pressure of around 10^{-8} mbar. This transparent top electrode was made by Yoonseok Park in Prof. Karl Leo's group in Dresden University of Technology.

Overcoming Leakage and Shorting Challenges in Silver Nanowire Organic Solar Cells

Metal Oxide Shell The ZnO layer in the nanowire solar cells not only acts as a selective electron extraction layer, but also passivates the AgNW electrode [210] to avoid shunt pathways in the device, due to its relative resistive property. Such effects

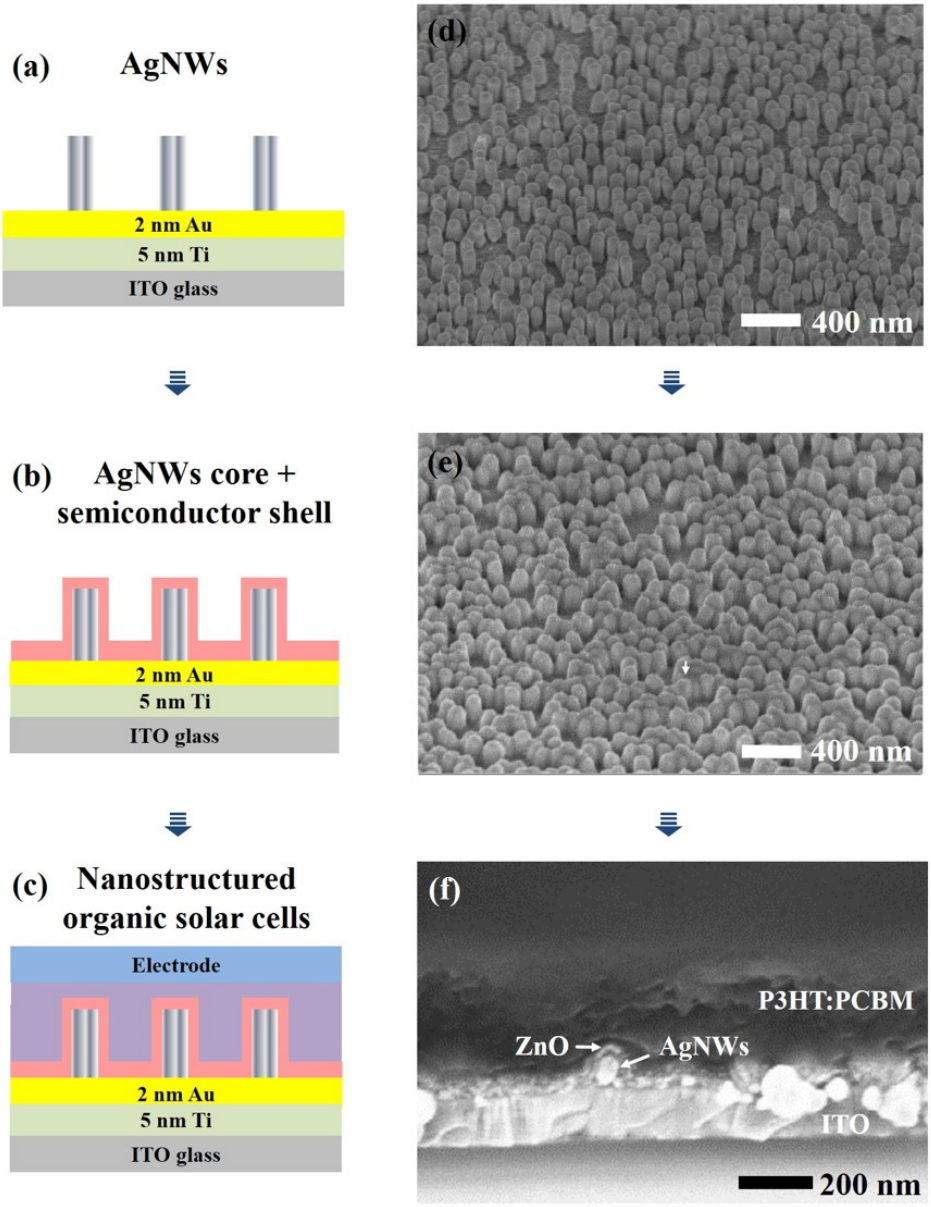

Figure 4.6.: (a-c) Schematic illustration of the fabrication process of the free-standing silver nanowire-based organic solar cells. (d) Side-view SEM image of free-standing AgNWs on an ITO glass. (e) Side-view SEM image of AgNWs-ZnO core-shell structure. (f) Side-view SEM image of the cleaved surface of a P3HT:PCBM coated sample. All SEM images were taken at an angle of $54°$ with respect to the horizontal axis.

are demonstrated in Figure 4.7, the JV curves showing severe shorting or leakage problems without proper coating of ZnO layers. The black curve shows totally linear IV characteristics. In this case, only a two-cycle spin-coating of ZnO was performed. When

another cycle of spin-coating of ZnO was performed, the shorting problem disappeared, although severe current leakage still existed (red curve in Figure 4.7). The extremely low J_{SC} and V_{OC} are likely due to the poor coverage of ZnO (with many pinholes) on the free-standing AgNW electrode, resulting in strong charge recombination. Finally, the four-step spin-coating plus pre-wetting, as described in "Device Architecture and Final Fabrication Process", is the best process optimized by far. This method gives an around 30 nm of ZnO layer on AgNWs (see Figure 4.6f). It is presumed that the pre-wetting assists the ZnO sol-gel to infiltrate the nanowire arrays, and the multi-step spin-coating leads to a nearly pinhole-free coating of ZnO on the AgNWs.

In addressing the passivation function of the metal oxide, it is important to mention one extreme example. I attempted to make non-inverted nanowire solar cells with an architecture of ITO /free-standing AgNWs /P3HT:PCBM /LiF /Al. However, the cells always had either shorting or severe leakage problems, despite using the optimized polymer spin-coating parameters. The main reason is probably the lack of a metal-oxide passivating layer, resulting in an easy short pathway between AgNWs and the top electrode.

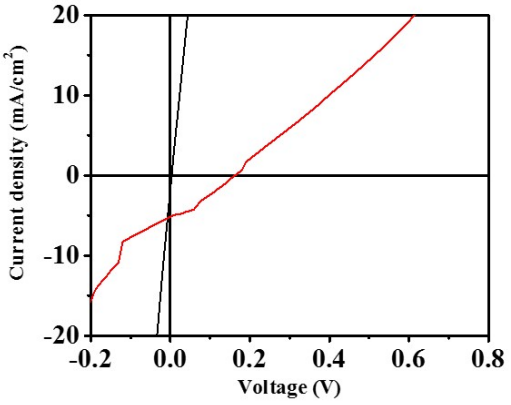

Figure 4.7.: Shorting and leakage problems with an improper spin-coated ZnO layer in AgNWs organic solar cells.

Additionally, TiO_2 is often considered to be an alternative for ZnO, due to its better chemical stability and band-gap similarity to ZnO.[211–213] A sputtered 50 nm of TiO_2 seems to fully cover the AgNWs, as show in Figure 4.8. We can see that the average diameter of the TiO_2 coated AgNWs (90 nm) is much larger than that of the pure AgNWs (50 nm). Likewise, the average length of such nanostructures increases from 150 nm to 190 nm after sputtering. Interestingly, the AgNW-TiO_2 core-shell nanostructure looks more like a baseball bat, due to the anisotropic coating. Unfortunately, using such core-shell nanostructures for organic solar cells led to a severe shorting problem. It

is presumed that the sputtered TiO_2 have too many pinholes to block hole transport towards ITO, resulting in severe charge recombination.

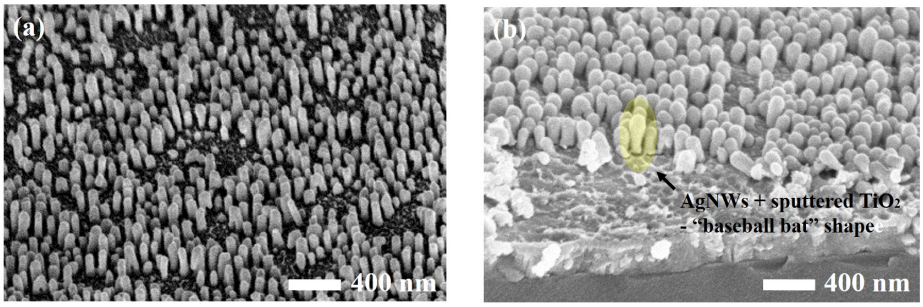

Figure 4.8.: (a) Pure free-standing AgNWs on Si substrate. (b) Quasiconformal coating of sputtered TiO_2 on AgNWs on Si substrate.

Pore Infiltration and Thickness of Polymer Complete filling of the pores in the nanostructured solar cells is critical in determining the efficiency.[214–216] Without proper pre-wetting, it is difficult for the polymer to fully penetrate into the pores of the free-standing AgNW arrays; many voids can be observed in the cross-sectional SEM image in Figure 4.9. Such incomplete pore filling leads to low current-density and poor fill factor, due to much longer charge paths, i.e., charges have to travel within the thin polymer film and then follow the shape of the nanowires. It was found that two steps of pre-wetting, described in "Device Architecture and Final Fabrication Process", ultimately led to complete pore filling, as shown in Figure 4.6f. In this case, the first pre-wetting in chlorobenzene (CB) enables the following polymer, dissolved in CB, to penetrate into the pores of the nanowire arrays.

Furthermore, a proper thickness of polymer is also crucial to achieve successful solar cells. A relatively thick polymer film dramatically prevents the AgNWs from touching the other electrode. For example, statistic experimental results show that with a thicker polymer (400 nm) film, the success rate of the device is much higher (over 50%; 68 pieces worked in 117 pieces of cells) than with a thinner film (290 nm). The success rate for the latter case was below 3%; only 1 piece worked in 36 pieces of cells.

Removal of Overgrown AgNWs Given that overgrown AgNWs easily contact the other flat electrode, it is important to remove overgrown AgNWs to achieve higher device success rate. Various methods were attempted and summarized in Table 4.1. As we can see, either finger sonication or Ar etching is able to partly remove the overgrown Ag without inhomogeneously destroying the AAO templates. It is worth noting that after Ar plasma treatment, the heads of AgNWs were to some extent damaged, and became branched heads, as displayed in Figure 4.10. Finally, a combination method of finger sonication and Ar etching was adopted, that is, first treating samples with Ar etching, then, exposing samples to finger sonication. It is assumed that the following

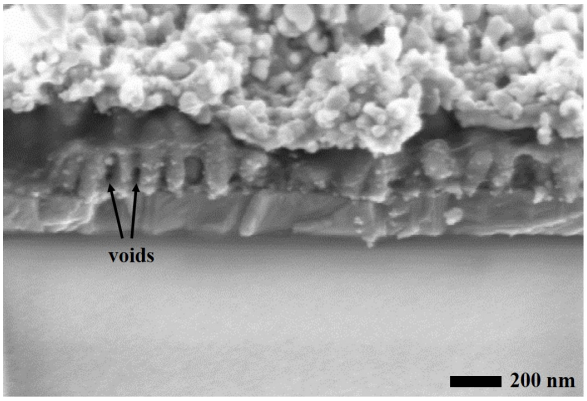

Figure 4.9.: Poor infiltration of polymer without pre-wetting.

finger sonication not only further removes partly overgrown AgNWs, but also cleans out the loosened Ag particles triggered by Ar etching.

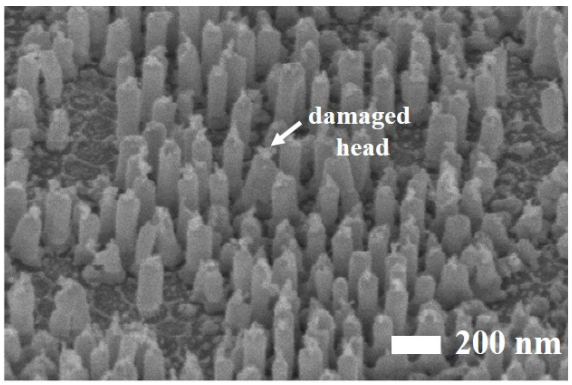

Figure 4.10.: Free-standing AgNWs with damaged heads due to Ar etching.

Perspectives on the Further Improvement of the Fabrication Process

Succeeding with working AgNWs-based solar cells is a big milestone, however further optimization is still needed.

- Despite that Ar etching and finger sonication are able to partly remove the overgrown AgNWs, in order to further increase the device success rate, the Au sputtering process needs further improvement. Because a homogeneous sputtered thin Au layer (2 nm) in batch is critical to guarantee reproducible high quality of AAO templates with evenly opened pores. With such AAO templates, AgNWs tend

Table 4.1.: Various attempts to remove the overgrown AgNWs. Note: 1) optimized parameters for finger sonication: 1.5 s pulse-on with 40% power and 4.5 s pulse-off, duration 5-10 min, the distance between the tip and sample was ca.2 mm; 2) Ar etching parameters: Ar flow rate 10 sccm, pressure 0.05 mbarr, power 300 W, duration 0.5-2 min.

Method	Result
Kapton tape lift-off	too weak to remove the overgrown Ag
traditional ultrasonication	too weak to remove the overgrown Ag
polishing by diamond abrasive paper (diameter: $1\,\mu$m)	so strong as to destroy the AAO templates
polishing by alumina abrasive paper (diameter: $1\,\mu$m or $0.3\,\mu$m)	so strong as to destroy the AAO templates
finger sonication (Bandelin Sonopuls HD3200)	partly removed the overgrown Ag
Ar etching (RIE SENTECH SI 220)	partly removed the overgrown Ag

to grow simultaneously to avoid inhomogeneous overgrowth. However, despite decreasing the sputtering deposition rate (0.75 nm/s) through reducing the sputtering power (to 20 W, which is nearly the minimum power for sputtering Au when using the AJA Orion 5; normally 36 pieces in a batch), plus increasing the rotation rate of the susceptor (70 rpm/min), inhomogeneous Au films were occasionally detected by eye. This technological challenge might be solved by modifying the recent sputtering system or using a more advanced machine.

- In terms of the metal oxide layer, the sol-gel method is not the final solution, since the precursor wetting process only leads to quasi-conformal coating, i.e., the top of the AgNW is covered by less ZnO compared to the bottom of the AgNW. Furthermore, the multi-step process of spin-coating plus pre-wetting, followed by immediate post-annealing requires not only time, but also much care in precise time control. Therefore, it is more desirable to use an atomic layer depostion (ALD) method to conformally coat the AgNWs. This method is also more applicable in industry. Such an ALD machine is under construction in our lab.
- In terms of the aforementioned unsuccessful non-inverted nanowire solar cells, ITO /free-standing AgNWs /P3HT:PCBM /LiF /Al, a relative resistive metal oxide hole extraction (HEL) layer urgently needs to cover the AgNWs in order to prevent the problem of shorting. Fortunately, it is possible to use some developed techniques from other groups, e.g. sol-gel methods for making V_2O_5 [217, 218], WO_3 [219] and MoO_3 [220].

4.3. Comparison of Flat and Core-Shell Silver Nanowire Organic Solar Cells

4.3.1. Opaque Organic Solar Cells

The opaque inverted AgNW-OSC and reference flat-OSC architectures are depicted in Figure 4.11a and Figure 4.11b, respectively. In this case, the fabrication process for

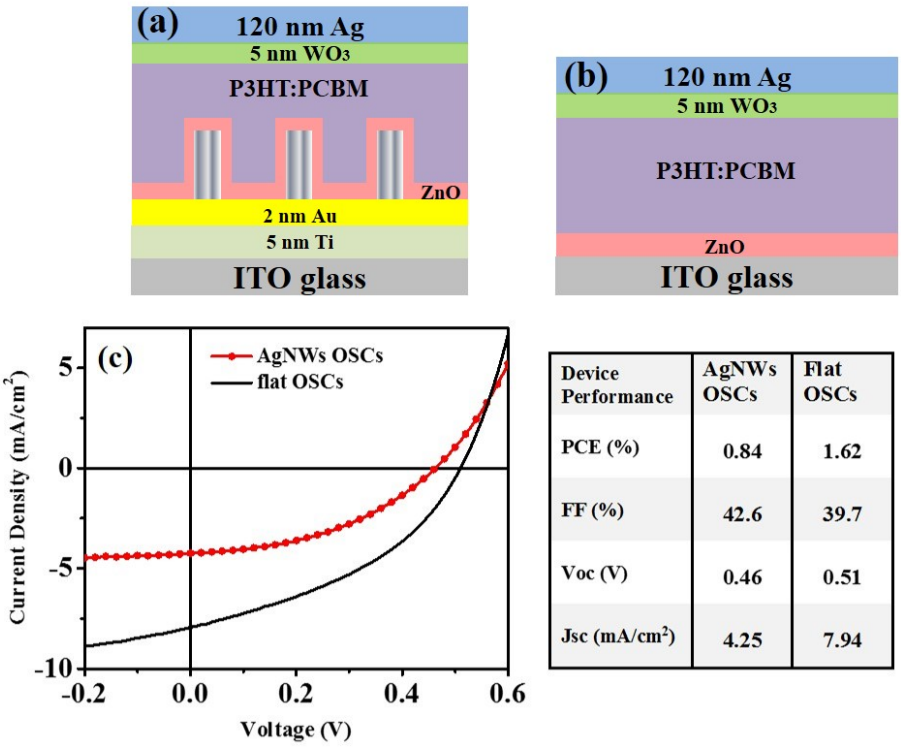

Device Performance	AgNWs OSCs	Flat OSCs
PCE (%)	0.84	1.62
FF (%)	42.6	39.7
Voc (V)	0.46	0.51
Jsc (mA/cm^2)	4.25	7.94

Figure 4.11.: (a) Schematic illustration of the inverted opaque AgNWs based OSCs. (b) Schematic illustration of the reference opaque flat-OSCs, wich is without Au and Ti layers. (c) J-V characteristics of opaque inverted OSCs with/without AgNWs.

both architectures (e.g., pre-wetting time, spin-coating parameters, etc.) were exactly the same. In other words, the thickness of ZnO and P3HT:PCBM for both architectures were comparably the same (ZnO - ca. 30 nm, and P3HT:PCBM - ca.400 nm). In this case, the average length of AgNWs is 150 nm. The resulting J-V curves and main characteristic values are shown in Figure 4.11c on both of the left and right sides.

The open circuit voltage (V_{OC}) of 0.46 V of AgNW-OSCs is 9.8% lower than that of the reference flat-OSCs (0.46 V). Such difference is attributed to the introduction of a 5 nm of Ti (part of Ti might become TiO_2 after the anodization process) and a 2 nm of Au layer in the device, which may influence the energy-level alignment on contact and, therefore, the V_{OC}. [221–223] This is further verified by comparative experiments of reference flat-OSC with and without Ti and Au layers, which present a similar difference of V_{OC}, that is, among 42 pieces of comparative solar cells, the V_{OC} exhibits $(8 \pm 0.9)\%$ decrement when introducing Ti and Au layers. Use of either alternative inter-layers with the same ability to act as an adhesive layer and a nucleation layer for AAO anodization and Ag electrodeposition, or advanced surface modification of the already developed Ti and Au inter-layers, but with more suitable energy-level alignment on contact for these solar cells, is an area for further investigation to achieve an

optimum V_{OC}. In addition, the V_{OC} of AgNW-OSCs drops slightly more (9.8%) than the upper limit of the flat-AuTiITO-OSCs (8.9%), which is expected to be due to the introduction of AgNWs, which further alters the energy alignment in the device.

The short circuit density (J_{SC}) of 4.25 mA/cm^2 of AgNW-OSC is unfortunately considerably low (46% decrement), resulting in a slightly higher geomcetric fill factor (FF) of 42.6%. Taking all characteristic parameters into account, a power conversion efficiency of $\eta = 0.84\%$ of AgNW-OSCs is achieved, which is 48% lower than that of the reference flat-OSCs. In order to get a better insight into the main limiting factor (low J_{SC}), total absorption and external quantum efficiency (EQE) measurements were carried out in a series of batch experiments.

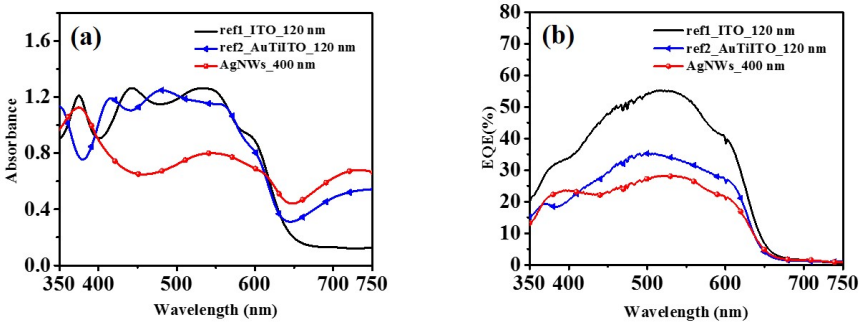

Figure 4.12.: (a) Total absorption measurements of the 1st reference flat-OSCs on pure ITO glass, the 2nd reference flat-OSCs on Au (2 nm) and Ti modified (5 nm) ITO glass, and AgNW-OSCs. In this case, the optimized P3HT:PCBM concentration (27 mg/ml) was used for the 1st and 2nd reference cells, whereas, a higher concentration of P3HT:PCBM (54 mg/ml) was used for AgNW-OSCs to ensure working nanowire solar cells. (b) Corresponding external quantum efficiency (EQE) measured under a short-circuit condition without additional bias illumination for these three types of solar cells. EQE is normalized to the measured J_{SC}.

In the case below, two types of optimized (the polymer concentration of 27 mg/ml, resulting a film of 120 nm) reference solar cells are introduced: ref1 is P3HT:PCBM solar cells on bare ITO glass; ref2 is P3HT:PCBM solar cells on Ti (5 nm) and Au (2 nm) modified ITO glass. For AgNW-OSCs, its thickness remains at 400 nm.

In the case of total absorption, a reflection-mode measurement inside an integrating sphere was carried out. In other words, $A_{tot} = 1 - R_{tot}$, where A_{tot} is the total absorption, and R_{tot} is the total reflection. Specifically, an additional 100 nm Ag film as a back-reflective mirror was evaporated to fully cover the Ag-electrode-side of the device, in order to receive a big incident light spot (ca. 4 mm $*$ 3 mm). This sample was positioned in the middle of the integrating sphere with an incident angle of 10°, ensur-

ing that the direct reflection of the device did not escape the integrating sphere but scattered off the sphere surface. Figure 4.12a depicts the total absorption of the three types of solar cells. In the main absorption region of the device (i.e., 350 nm to 650 nm), ref1 exhibits four absorption peaks at 375 nm, 440 nm, 550 nm and 600 nm. In comparison, ref2 exhibits four peaks at 420 nm, 480 nm, 560 nm and 600 nm. This oscillating feature results from the constructive and destructive interference between incident light and reflected light in the solar cell cavity.[224–226] Interestingly, the integrals of the absorption of ref1 and ref2 from 350 nm to 650 nm are almost the same (with only a slight drop of 3% for ref2), indicating that the reflection-off-device effect of the thin Au and Ti layers is negligible. In contrast, the AgNW-OSCs absorb considerably less, the integral of which is 23% lower than that of ref2, in spite of a thicker active layer. This is mainly due to the strong front reflection-off-device effect of the dense AgNW arrays, since Ag has the highest reflectance among all metals.[227–229] Moreover, the number of distinguished peaks is reduced to two, partly due to the suppression of the resonant Fabry-Perot mode as a result of nanostructures [230], and also partly due to the thicker active layer, in which most incident light is absorbed before reaching the other reflective electrode, resulting in a smaller interference effect.[224] It is worth noting that the positions of the two peaks (at 375 nm and 550 nm) correspond with the localized surface plasmonic resonance positions of AgNW arrays as shown in Section 3.4.1, if considering red-shift effect after filling dielectric materials into the AgNW arrays [231], indicating that the surface plasmonic effects could play a role in terms of the total absorption in AgNW-OSCs.

The corresponding EQE results are shown in Figure 4.12b. Surprisingly, the overall EQE level (the integral from 350 nm to 650 nm) of ref2 is significantly lower than that of ref1, dropping around 36%, while their overall values of total absorption are nearly the same. It is found that such dramatic difference is mainly a result of the parasitic absorption (the absorption that does not contribute to the photocurrent [226]) of Au and Ti layers, which is verified by the transmittance spectrum of Au and Ti modified ITO glass, as shown in Figure C1 in Appendix C. Furthermore, oscillating behavior in the absorption disappears in the EQE, due to the influence of the electronic properties of the organic layer.[232] In terms of the AgNW-OSCs, the two EQE peaks (at ca. 375 nm and 550 nm) correspond with the absorption peaks in the left graph. Particularly, at ca. 375 nm, the EQE of AgNW-OSCs is higher than that of ref2, while the same trend can be seen in the absorption graph, indicating a good optical match. It should be mentioned that a slight wavelength mismatch (ca. 10 nm) is due to the spectral mismatch of the lamps in different setups. Most interestingly, compared to ref2, the overall EQE of AgNW-OSCs decreases only 15%, but its total absorption decreases much more (23%), indicating that AgNWs play a positive role in terms of the electronic properties of the device, compensating for the optical loss. In order to better understand the role of AgNWs in the electronic properties of the device, it is necessary to analyze the internal quantum efficiency (IQE), absorbed photon to electron conversion, since it separates electronic properties from optical properties.

Figure 4.13 shows the IQE curves of ref2 and AgNW-OSCs. The IQE of AgNW-OSCs

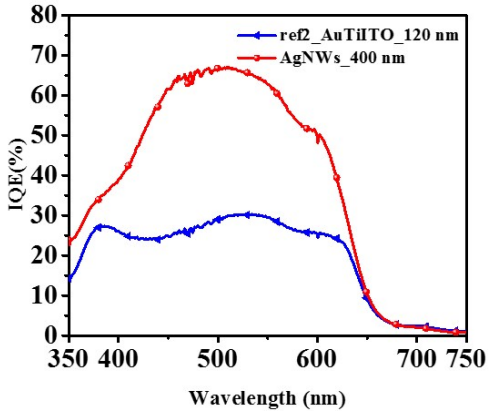

Figure 4.13.: Internal quantum efficiency (IQE) of the 2nd reference flat-OSCs on Au (2 nm) and Ti modified (5 nm) ITO glass and AgNW-OSCs, calculated using IQE=EQE/A_{tot}. Here the parasitic absorption of ITO glass, Au, and Ti layers is neglected [225, 226], since it does not affect comparative analysis of these two types of solar cells.

far outweighs ref2 in the whole wavelength range, indicating a superior electron collection efficiency due to the direct path channels provided by vertically aligned AgNWs. [17, 233, 234] This high IQE further confirms that the power conversion efficiency loss of AgNW-OSCs is mainly due to the optical reflection-off-device effect of AgNWs.

To address the optical loss problem, one solution could be to reduce the density of AgNWs. Going back to the fabrication process of free-standing AgNWs, by significantly reducing the diameter of the AgNWs while keeping the inter-pore distance the same is not practical, since the pore-widening time should be long enough to remove the barrier layer at the bottom of the AAO pores in order to ensure successful electrodeposition. A novel idea, discussed recently with Prof. Andre ten Elshof, is coating a layer of nanoporous block copolymer onto the AAO template to block parts of AAO pores, and then performing electrodepositon of AgNWs. This method is worthy of further work. Another solution could be to use a top transparent electrode instead of an opaque thick Ag film electrode. In this case, the incident light would pass through the top transparent electrode, then the polymer layer, and finally would be reflected back by the free-standing AgNWs electrode. This semi-transparent architecture would not only eliminate the drawback of the front reflection-off-device effect of AgNWs, but is also appealing in applications for power generating windows in cars and buildings.[235, 236] This type of solar cell will be discussed in detail in Section 4.3.2.

In addition, from the IQE of AgNW-OSCs we cannot see two distinctive peaks (expected at 375 nm and 550 nm, related to the absorption curve in Figure 4.12a), corresponding to the transversal and longitudinal plasmonic resonances. The reason for this is that

the intervening thick ZnO layer (30 nm) between the AgNWs and polymer inhibit the near-field enhancement.[237] In another words, the enhanced plasmonic electric field near the AgNWs does not act on the polymer to enhance photocurrent generation, due to a thick ZnO layer in between. It is believed that the weak peak at 375nm was not due to the plasmonic effect of the AgNWs, but from the absorption of the functional layers, since the ref2 also shows a peak at the same position.

4.3.2. Semi-Transparent Organic Solar Cells

As mentioned above, replacing the traditional 100 nm of Ag electrode with a transparent top electrode provides the attractive possibility of not only eliminating the drawback of the front reflection-off-device effect of AgNWs, but also would allow for novel applications in power generating windows in cars and buildings.[235, 236] This section will illustrate this great potential and also deal with challenges of semi-transparent organic solar cells based on free-standing silver nanowires.

The architectures of semi-transparent AgNW-OSCs and reference flat-OSCs are depicted in Figure 4.14a-b, respectively. In this case, the fabrication process for both architectures were exactly the same, with a 30 nm of ZnO layer and a 400 nm of P3HT:PCBM layer . The transparent top electrode (MoO_3 (3 nm) /Al (1 nm) /Ca:Ag (mixing ratio 2:1, 9 nm) /Alq3 (60 nm)) was thermally evaporated at a base pressure of around 10^{-8} mbar, by Yoonseok Park in Prof. Karl Leo's group in Dresden University of Technology. The interval time between polymer spin-coating and device characterization was around 8 days, but in most cases the samples were kept in nitrogen containers in order to minimize degradation.

For the details of the excellent optoelectronic properties of this electrode, I recommend the reader to refer to the recently published paper [238, 239] by Prof.Karl Leo's group. At first, their group applied this electrode to the small molecular organic solar cells. Later on, for this project, their electrode also worked successfully for our bulk heterojunction polymer:fullerene organic solar cells. The resulting power conversion efficiency (PCE) of the champion solar cells fabricated by a standard process (flat solar cell with a 120 nm of P3HT:PCBM layer), exhibits 1.01% through ITO glass illumination, and 0.74% through Ca:Ag illumination. The main reason for the 27% difference of PCE is that the metallic Ca:Ag electrode acts as a better back-reflector than the ITO electrode, resulting in an enhanced optical absorption in the active layer when the solar cells are bottom illuminated through ITO glass.[240] The details of J-V characteristics are shown in Figure C1 in Appendix C.

Figure 4.14c-d presents a comparison of J-V characteristics between AgNW (130 nm)-OSCs and reference flat-OSCs. In the case of bottom illumination through ITO glass, V_{OC} for AgNW (130 nm)-OSCs is lower (7%) than the reference flat-OSCs. One reason

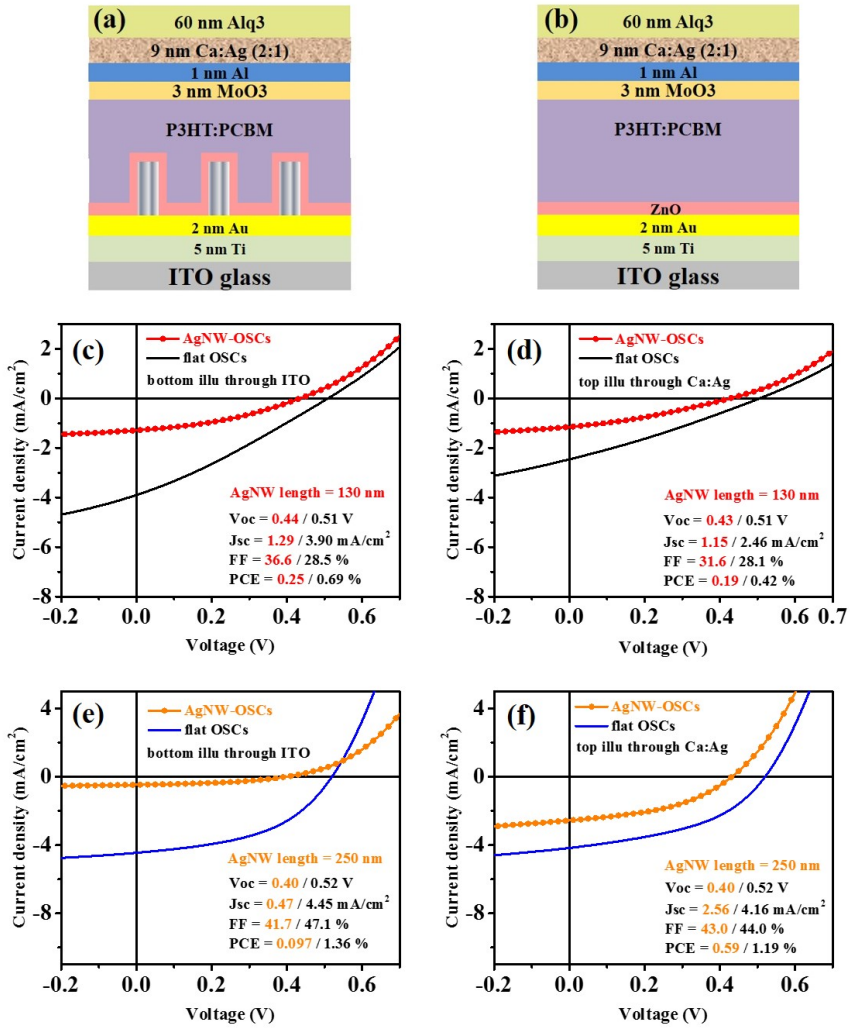

Figure 4.14.: (a) Schematic illustration of the semi-transparent AgNWs based OSCs (AgNW-OSCs). (b) Schematic illustration of the reference semi-transparent OSCs (flat OSCs), which is with Au and Ti layers. (c) J-V curves and characteristic values of semi-transparent OSCs with/without AgNWs (130 nm) under bottom illumination through ITO glass. (d) J-V curves and characteristic values of semi-transparent OSCs with/without AgNWs (130 nm) under top illumination through Ca:Ag top electrode. (e) J-V curves and characteristic values of semi-transparent OSCs with/without AgNWs (250 nm) under bottom illumination through ITO glass. (f) J-V curves and characteristic values of semi-transparent OSCs with/without AgNWs (250 nm) under top illumination through Ca:Ag top electrode. The illumination light intensity is ca. 80 mW/cm^2. Moreover, (c-d) and (e-f) were fabricated in two batches.

for this is that the insertion of AgNWs may change the energy level alignment in the device, hence the V_{OC}. Another reason could be the Au and Ti modified ITO substrates for AgNW (130 nm)-OSCs and reference flat-OSCs were sputtered in different batches, possibly leading to a fluctuation of Au and Ti's thickness, which in turn changes the

energy level alignment in the device. On the other hand, the J_{SC} for AgNW (130 nm)-OSCs is significantly lower (67%) than the reference flat-OSCs. This is as expected, since the front reflection-off-device of AgNWs causes a big optical loss. Accordingly, the significantly lower J_{SC} for AgNW (130 nm)-OSCs results in a higher geometric FF of 36.6%, compared with 28.5% for flat-OSCs. The difference of the FF is 22%. Considering all characteristic parameters, PCE for AgNW-OSCs ($\eta = 0.25\%$) is 64% lower than for flat-OSCs ($\eta = 0.69\%$).

In the case of top illumination through Ca:Ag electrode, the V_{OC} for AgNW (130 nm)-OSCs and flat-OSCs shows no significant change compared with the former case (i.e. bottom illumination through ITO glass). However, compared with the flat-OSCs, the J_{SC} for AgNW (130 nm)-OSCs drops only 53%, rather than 67% shown in the former case, owing to the back-reflection effect of AgNWs. Accordingly, with a smaller drop of J_{SC} for AgNW (130 nm)-OSCs, the geometric FF has a smaller increase of 11%, rather than 22% shown in the former case. Consequently, the PCE for AgNW (130 nm)-OSCs ($\eta = 0.19\%$) is 55% lower than for flat-OSCs ($\eta = 0.42\%$). This is less than the 64% drop shown in the former bottom illumination, indicating a benefit from the back-reflection effect of AgNWs.

In order to confirm the validity of the above solar cell data, results from a second statistically independent set of solar cells with longer AgNWs (250 nm) were analysed. This second set showed a similar trend in terms of V_{OC} and J_{SC} (see Figure 4.14e-f). In other words, V_{OC} is independent of the direction of illumination. And the J_{SC} for AgNW (250 nm)-OSCs drops less (38%, referenced to flat-OSCs) under top illumination than that under bottom illumination (89%). It is worth noting that increasing the AgNW length reduces the V_{OC}. This can be associated with the increased recombination across the high-interface-area.[241, 242] It is also expected that longer AgNWs increase the chance of shorting paths in the device, leading to reduced V_{OC}. Moreover, longer AgNWs lead to a starker contrast of J_{SC} for AgNW-OSCs in terms of changing the illumination direction. This may be attributed to the stronger reflection effect of longer AgNWs, due to the higher effective thickness (the ratio of volume of AgNWs to device's surface area). However, FF shows an opposite trend, i.e. FF for AgNW-OSCs being always lower than that for flat-OSCs, mainly because of the series resistance. It seems that the series resistance relates to charge carrier transport effects [243–245], but how this effect contributes to the opposite FF behavior remains unclear. Taking all these characteristic parameters into consideration, the PCE drops less (50%, $f(\eta_{\text{flat-OSC}} - \eta_{\text{AgNW-OSCs}})/\eta_{\text{flat-OSCs}}$) under top illumination than it does under bottom illumination (93%).

However, compared with the reference flat-OSCs under the same illumination direction, the PCE for AgNW-OSCs is always lower. To fundamentally understand how AgNWs affect the device performance, in order to ultimately realize their full potential in solar cells, further investigations are required, as shown in the following discussions.

In Figure 4.15a-b the results of the EQE measurements for AgNWs (130 nm)-OSCs

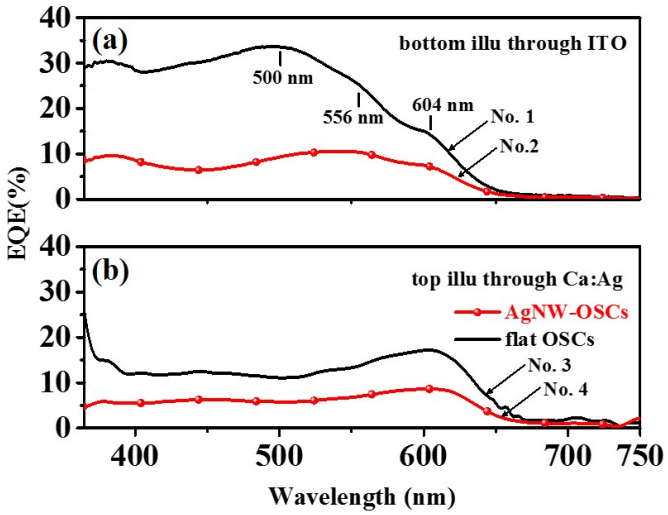

Figure 4.15.: (a) Normalized EQE of flat-OSCs (No. 1) and AgNW (130 nm)-OSCs (No. 2) under bottom illumination through ITO glass. (b) Normalized EQE of flat-OSCs (No. 3) and AgNW (130 nm)-OSCs (No. 4) under top illumination through Ca:Ag electrode.

and flat-OSCs from different illumination directions are shown. In the case of bottom illumination through ITO glass (Figure 4.15a), the EQE for flat-OSCs (No. 1) shows a maximum peak at 500 nm and two shoulders at 556 nm and 604 nm, which are characteristics of crystalline P3HT.[246–248] Meanwhile, the spectrum at shorter wavelengths below 500 nm is overlapped with PCBM.[246] On the other hand, for AgNW-OSCs (No. 2), except for the overall EQE decreasing, the maximum peak at 500 nm also decreases. This can mainly be attributed to the strong reflection-off-device effect of AgNWs. It also seems that the reflection of AgNWs at around 500 nm is stronger than that at other wavelengths in the range of 360-650 nm.

In the case of top illumination through Ca:Ag electrode (Figure 4.15b), for both flat-OSCs (No. 3) and AgNW-OSCs (No. 4), two characteristic peaks of P3HT at 500 nm and 556 nm decreased significantly. Moreover, in both cases (No. 3 and No. 4), the overall EQEs are lower than that of bottom illumination. This could be attributed to the non-optimized optical spacer (MoO_3), leading to a non-optimized cavity mode for top illumination.[249] Further optimization of the thickness of MoO_3 should be performed. Another reason could be that the extreme slow solidification process of P3HT:PCBM film (i.e., step 1: spin-coat at 50 rpm for 2 min; step 2: spin-coat at 1500 rpm for 1 min) resulted in a vertically graded-composition of the active layer [250, 251], leading to this asymmetric behavior of EQE.

Figures 4.16a-b show the charge collection probability (CCP) as a function of applied

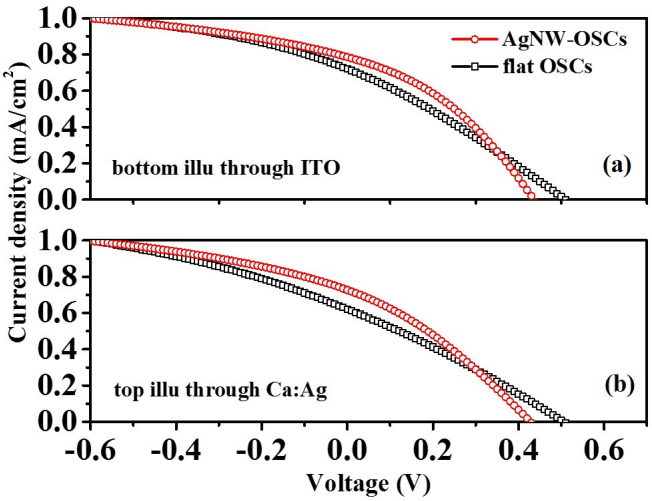

Figure 4.16.: (a) Charge collection probability (CCP) for AgNW (130 nm)-OSCs and flat-OSCs under bottom illumination through ITO glass, normalized with the reverse saturation current at -0.6 V. (b) Charge collection probability (CCP) for AgNW (130 nm)-OSCs and flat-OSCs under top illumination through Ca:Ag electrode, normalized with the reverse saturation current at -0.6 V.

voltage. The CCP is calculated by:

$$CCP(V) = \frac{J(V)}{J(-0.6\,\mathrm{V})} \tag{4.1}$$

where $J(V)$ is the measured current density under light illumination, and $J(-0.6\,\mathrm{V})$ is the reverse saturation current at $V = -0.6\,\mathrm{V}$. It is worth noting that the measured current density under illumination is directly used here as photogenerated current rather than "the" photocurrent density ($J_{\mathrm{photo}}(V) = J(V) - J_{\mathrm{dark}}(V)$) used in Cowan et al. [252] and Street et al. [253], since very recently Würfel et al. [254] showed that the photocurrent density ($J_{\mathrm{photo}}(V) = J(V) - J_{\mathrm{dark}}(V)$) lacks physical meaning in organic solar cells. From Figures 4.16a-b, we can see that the charge collection probability in AgNW-OSCs is generally larger than that of the reference flat-OSCs under each illumination direction, except that at near 0.4 V the CCP for AgNW-OSCs drops below its reference flat-OSCs, due to the low V_{OC} of AgNW-OSCs. Hence, it could be predicted that if the V_{OC} issue for AgNW-OSCs was overcome, the CCP for AgNW-OSCs would outweigh that for flat-OSCs over the whole applied voltage range. It should be mentioned that so far I cannot conclude with certainty that AgNWs enhance the charge collection probability in organic solar cells, since in another independent batch this behavior is not apparent. The reproducibility of the AgNW-OSCs needs further improvement.

To gain further insight into the physics of AgNW-OSCs and flat-OSCs and to quantify the limiting factors, the light-intensity dependence of the current density has been

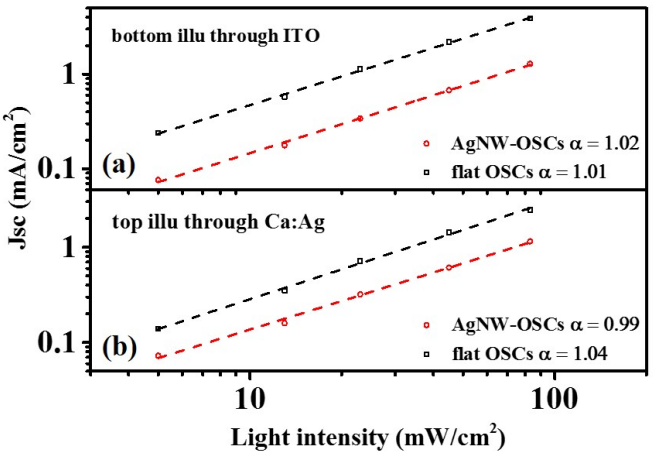

Figure 4.17.: (a) Light intensity dependence of short-circuit current density (J_{SC}) for AgNW (130 nm)-OSCs and flat-OSCs under bottom illumination through ITO glass. The straight lines show the power law fits to $J_{SC} \propto I^{\alpha}$ on a log-log scale. (b) Light intensity dependence of short-circuit current density (J_{SC}) for AgNW (130 nm)-OSCs and flat-OSCs under top illumination through Ca:Ag electrode. The straight lines show the power law fits to $J_{SC} \propto I^{\alpha}$ on a log-log scale.

studied. Using a set of neutral density filters, the light intensities ranging from 5 to 83 mW/cm^2 were created. The light-intensity dependent J-V curves are displayed in Appendix C4. Generally, the generation rate (G) of e-h pairs is proportional to the light intensity (I).[255, 256] Quantitatively, the photogenerated current density (J) follows the power law [252]:

$$J_{SC} \propto I^{\alpha} \tag{4.2}$$

where $\alpha = 0.75$ in the case of the ideal space-charge limit, and $\alpha = 1$ in the case of space-charge-free limit.[256–259] Figures 4.17a-b display that α is always close to 1 for all types of solar cells on a log-log scale, irrespective of the illumination directions. This demonstrates that there is no space-charge limit under short-circuit condition for both AgNW-OSCs and flat-OSCs.

Furthermore, the space-charge/non-space-charge limit effect at varying applied bias is also examined based on Blom et al.'s [257, 258] and Rose et al.'s [260, 261] model:

$$J \propto G^{3/4} \cdot {V_{eff}}^{1/2} \tag{4.3}$$

where J is the photogenerated current, G is the generation rate of e-h pairs, and V_{eff} is the effective voltage, i.e. V_{OC}-$V_{applied}$ ($V_{applied}$ is simplified as V in the following text). Hence, the pure space-charge-limit photogenerated current is characterized by a square-root dependence on effective voltage and a three quarter dependence on light

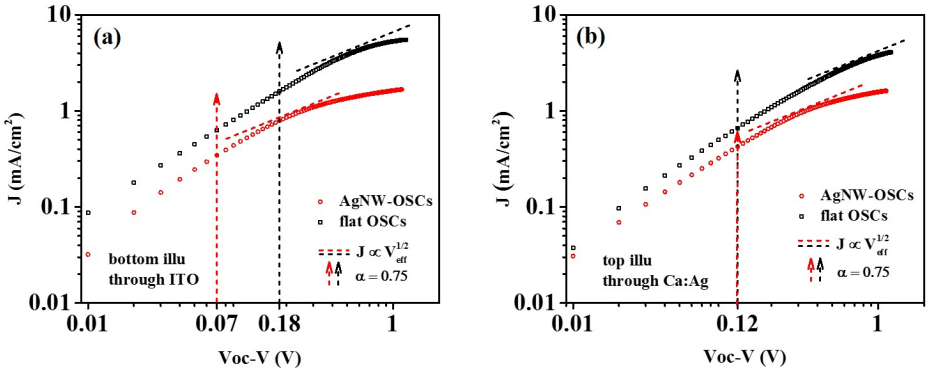

Figure 4.18.: (a) Photogenerated current density J as a function of the effective voltage V_{OC}-V, for AgNW (130 nm)-OSCs and flat-OSCs under bottom illumination through ITO glass. (b) Photogenerated current density J as a function of the effective voltage V_{OC}-V, for AgNW (130 nm)-OSCs and flat-OSCs under top illumination through Ca:Ag electrode. The illumination light intensity is 83 mW/cm^2. The dashed lines indicate the square-root dependence on V_{OC}-V, which is extracted from the first derivative of the J-(V_{OC}-V) curve, as shown in Appendix C5. The arrows indicate fits of the light intensity dependence $J_{SC} \propto I^{3/4}$, i.e., $J_{SC} \propto G^{3/4}$.

intensity.[257, 258]. In Figure 4.18a-b, the photogenerated current J is plotted as a function of the effective voltage, V_{OC}-V, on a log-log scale. However, it is not possible to find a point where the current J fits both a square-root dependence on effective voltage and a three quarter dependence on light intensity, implying that there is no apparent space-charge limit effect between the open- and short-circuit points. This can be attributed to the balanced electron and hole transport in the device (i.e. the mobility imbalance between e and h is smaller than two orders of magnitude.[262]). Besides, in this batch, the different shape of the J-(V_{OC}-V) curves between AgNWs-OSCs and flat-OSCs in the higher effective voltage regime demonstrates that the different J-V curves of AgNW-OSCs and flat-OSCs under illumination cannot be attributed only to their different open-circuit voltage, but also other unknown factors.[263] However, in another independent batch, as shown in Appendix C6, the shape of the J-(V_{OC}-V) curves is near identical, indicating a solely open-circuit voltage attribution to the different J-V curves of AgNW-OSCs and flat-OSCs.[263] Therefore, so far, the explanation in this thesis for the shape of the J-(V_{OC}-V) is not yet conclusive. However, a conclusion that can be drawn is that there is no apparent space-charge limit effect between the open- and short-circuit points in both AgNW-OSCs and flat-OSCs.

Excluding the effect of the space-charge limit, other limiting factors are examined by exploring the light-intensity dependence of the open-circuit voltage. Since for open-circuit conditions the drift and diffusion current balance out and all the photogenerated charge carriers recombine, the properties of solar cells strongly depend on the recombination processes.[264, 265] Blom et al. [264] has demonstrated that in polymer:fullerene bulk

heterojunction solar cells V_{OC} fits the law:

$$V_{OC} \propto n\frac{kT}{q}ln(I) \tag{4.4}$$

where k is the Boltzmann constant, T is the temperature, q is the elementary charge, kT/q is 0.025 eV at room temperature, I is the light intensity, and n is the ideality factor. With different values of n, different recombination processes dominate with an assumption of equal capture across sections of electrons and holes [266]:

- $n = 0.5$, absence of band bending in the vicinity of non-ohmic contacts.[267]
- $n = 1$, recombination via band tail states, namely, shallow trap-state-mediated recombination.[266, 268]
- $n = 2$, recombination via midgap states, namely, deep trap-state-mediated recombination.[266, 268]
- $n > 2$, either tunneling-enhanced bulk recombination [266, 269], or recombination due to local nonlinear shunts [266, 270], or recombination at extended defect sites.[266, 271]

It is worth mentioning that Nguyen et al. [272] suggest that before fitting the V_{OC} vs. light intensity, we should first check the dependence of fill factor (FF) on the light-intensity (see Figure C7a in Appendix C). If the FF starts dropping with light-intensity, the slope of the V_{OC} vs. light-intensity will be misleading.[272] As is demonstrated in Figure C7a in Appendix C, the FF does not drop with decreasing light-intensity in the whole range of 5-83 mW/cm^2 for the batch of AgNW (130 nm)-OSCs and flat-OSCs. Therefore, the fitting of the V_{OC} vs. light-intensity in Figure 4.19 is valid. The results show that for both AgNW-OSCs and flat-OSCs, the ideality factor n is always over 2. However, it has been shown that for a standard flat P3HT:PCBM solar cell with a thickness of 100-250 nm, n is close to 1 [252], which is attributed to a shallow trap-state-mediated recombination.[266] The much higher value of n over 2 in my case is probably due to the polymer film's thickness (400 nm) and its vertically graded properties. This might lead to extended defect sites for recombination.[266, 271] In addition, the factor that n is over 2 is also evidenced in another independent batch of solar cells, shown in Figure C8 in Appendix C.

4.4. Summary and Future Work

Organic solar cells (OSCs) based on metal-semiconductor (AgNW-ZnO) core-shell nanowire arrays have been successfully fabricated after overcoming the challenges of the infiltration of polymer into the pore, and shorting pathways in the device. The in-depth investigation into the device characteristics indicate that the AgNWs seem to enhance the charge collection efficiency. However, using too thick a polymer film (which is necessary to ensure a working device) combined with the increased nanowire-polymer interface, introduces extended defect sites for recombination, which limits the efficiency

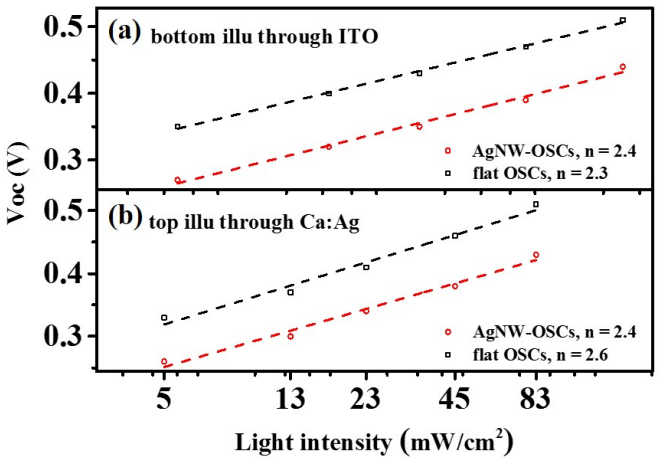

Figure 4.19.: (a) Light intensity dependence of open-circuit voltage (V_{OC}) for AgNW (130 nm)-OSCs and flat-OSCs under bottom illumination through ITO glass on a linear/logarithmic ($ln(I)$) scale. The straight lines show fits to $V_{OC}(I) \propto 0.025 \cdot n \cdot ln(I)$. (b) Light intensity dependence of open-circuit voltage (V_{OC}) for AgNW (130 nm)-OSCs and flat-OSCs under top illumination through Ca:Ag electrode on a linear/logarithmic ($ln(I)$) scale. The straight lines show fits to $V_{OC}(I) \propto 0.025 \cdot n \cdot ln(I)$.

of the nanowire solar cell. An ideal architecture would use a proper semiconductor layer with low recombination rate as well as a very thin polymer layer to conformally coat the AgNW nanowire arrays, making use of the charge collection and light trapping advantages, but minimizing recombination.[19] It should be mentioned that due to poor reproducibility of the AgNW-OSCs, the analysis is based on a few successful solar cell data. To draw a solid conclusion, more statistic data is needed. In the future, the reproducibility needs further improvement, for example, from the aspects of removing the overgrown stones of AgNWs. Moreover, the thickness of MoO_3 should be tuned towards an optimally matched cavity mode. Furthermore, the techniques of coating semiconductor and polymer also need further improvement.

On the other hand, attempts at applying AAO templates for the recently emerging perovskite (PVK) solar cells indicate a new promising direction for the future. Two AAO systems have been tried with Hao Hu: (1) ITO / Ti/ Au/ AAO/ PVK / C60/ LiF/ Ag; (2) ITO / TiO_2 / AAO/ PVK / C60/ LiF/ Ag. The system-1 encountered shorting problems, indicating a blocking layer of TiO_2 is necessary for the PVK solar cells. In contrast, the system-2 had no shorts, but the currents were too low (4 mA/cm^2) compared with the values obtained by others in the field.[273–275] This is attributed to the aluminum oxide barrier layer at the bottom of the AAO pores, blocking the charge extraction. In the future, further new techniques need to be developed such as a step-wise reducing voltage method [276] to remove the aluminum oxide barrier layer. This AAO-PVK solar cell system is very promising systematically investigating how charge

transport behaves in AAO-confined PVK film by tuning the size of AAO pores.

5. Conclusion and Outlook

5.1. Conclusion

The aim of this work was to explore free-standing silver nanowire arrays as electrodes for ultimately enhancing the efficiency of organic solar cells. For this purpose, a first prerequisite is developing a novel technique for reproducibly synthesizing large-area free-standing silver nanowire arrays on ITO glass. I have found that an in situ oxygen plasma cleaning of the ITO surface and a sputtered Ti layer provide excellent adhesion during the anodization process. An ultrathin gold layer (2 nm) is a desirable nucleation layer for the electrodeposition of Ag. Furthermore, a stable non-toxic electrolyte compatible with the AAO templates has been developed. Finally, an unprecedented high level of uniformity and control of the nanowire diameter, spacing and length has been achieved.

Moreover, a sol-gel spin-coating process has been developed to quasi-conformally coat the silver nanowire arrays with a ZnO shell, forming a hybrid metal-semiconductor (AgNWs-ZnO) core-shell nanowire arrays. Furthermore, these AgNWs-ZnO core-shell nanostructures have been successfully incorporated into organic solar cells (OSCs) by solving the common challenges in the nanowire solar area, i.e. shorting and leakage problems. At first, the AgNWs-ZnO nanowires were applied in opaque organic solar cells. Encouragingly, comparison of AgNWs-OSCs and flat-OSCs' internal quantum efficiency (IQE) data indicate an increased charge collection in AgNWs-OSCs. However, due to a strong incident light reflection-off-device effect of the dense AgNWs, the overall power conversion efficiency (PCE) of AgNWs-OSCs is lower than flat-OSCs.

To address the optical loss problem, a high-quality of transparent top electrode (technique from Prof. Karl Leo group) was introduced to replace the opaque thick Ag film (120 nm), forming a semi-transparent organic solar cells. Hence, it is possible to illuminate light from the transparent top electrode and treat AgNWs as a back-reflection electrode. An in-depth investigation of the device physics in terms of external quantum efficiency, charge collection, and recombination has been performed. The results indicate that the AgNWs seem to enhance the charge collection efficiency also in the semi-transparent OSCs. However, using too thick a polymer film (which is necessary to ensure a working device) combined with the increased nanowire-polymer interface, introduces extended defect sites for recombination, which limits the efficiency of the nanowire solar cell. Finally, my work yields a clearer design route for AgNW-OSCs, suggesting the use of a proper semiconductor layer with low recombination rate as well as a very thin polymer layer to conformally coat the AgNW nanowire arrays. In this

way, the nanowire solar cells not only make use of the charge collection and light trapping advantages of AgNWs, but also minimize recombination losses.

5.2. Outlook

This work has presented the significant progress in the free-standing silver nanowires (AgNWs) used as an electrode for organic solar cells. Yet, there are still room for further improvement and also ideas of new directions. For surface enhanced Raman scattering (SERS) application of AgNW arrays and further improvement of AgNW-OSCs, the details are described in the Section of "Summary and Future Work" in Chapter 3 and Chapter 4, respectively. Here I would like to present two new directions.

5.2.1. Low-Temperature Plamonics of Metallic Nanowire Arrays

Plasmonic effects of metallic nanostructures have increasingly drawn scientists' attention due to their important applications in the field of biosensing [277–279], gas detecting [280] and quantum information processing [281, 282]. The majority of the efforts have been focused on manipulating the spectral response by changing the permittivity of the surrounding dielectric.[277–279] However, very limited work has been concerned with low-temperature plasmonic behaviors of metallic nanostructures. Zayats et al.'s have recently found that the excitation of plasmonic free-standing gold nanowires can be efficiently controlled with temperature, i.e., the transmission changes by approximately a factor of 10 from room temperature to the liquid nitrogen temperature (77 K).[283] However, they did not go further to even lower temperature (i.e. liquid helium (4 K)) to investigate the interesting electrical conductivity saturation regime.[284] Furthermore, they have only reported the lower-temperature behavior of AuNWs, but not AgNWs. Generally, silver exhibits superior plasmonic effects than gold due to its longer surface plasmon–polariton length.[285] Therefore, it is worth to investigate the wide-range temperature-dependence (from room temperature to the liquid helium temperature) of plasmonic silver nanowire arrays.

Preliminarily, I have built a temperature&angle-resolved UV-Vis setup with Prof. Paul Leiderer, as shown in Figure D1a-b in Appendix D. Furthermore, the preliminary results of the temperature-dependent transmission and angle-dependent reflection spectra of a AgNWs-AAO sample, as shown in Figure D2a-b in Appendix D, tell us that we have a measurable setup. However, more work regarding wavelength calibration and aberration correction needs to be done in order to get reliable and reproducible results. Given that AuNW arrays on ITO glass have been also successfully fabricated, as described in Section 3.2.1, ultimately it would be very interesting to compare the low-temperature physics of plasmonic AgNW and AuNW arrays.

5.2.2. Control of the Space-Charge Region in Hybrid Solar Cells via AgNW-semiconductor Arrays

In contrast to bulk heterojunction organic solar cells, the new concept of organic-inorganic hybrid solar cells combines the advantages of organic (e.g. low cost and flexible) and inorganic (e.g. chemically stable and tunable band gap) materials to further push forward the frontiers of the solar cell technology. But so far, the efficiencies of hybrid solar cells are relatively low. Numerous research efforts have been made to better understand these hybrid systems and ultimately improve the power conversion efficiency. One of the most heavily investigated standard systems is based on the combination of metal-oxide (e.g. TiO2 and ZnO) and conjugated polymer (i.e. P3HTand PCPDTBT). This system is ideal for investigating the interfacial electron transfer dynamics and engineering the interface to reduce recombination.

However, the role of the space-charge limited (SCL) photocurrent has been widely neglected in organic/inorganic hybrid solar cells. In 1971 Goodman et al. predicted the occurrence of a fundamental electrostatic limit for photocurrent in semiconductors at high light intensities.[260] In 2005 Blom et al. both theoretically and experimentally demonstrated that the photocurrent in bulk heterojunction organic solar cells blend can be limited by the build-up of space-charge, even under normal operational conditions equivalent to 1 sun illumination.[257] In 2006 Mihailetchi et al. demonstrated an efficiency increase of a P3HT: PCBM solar cell by diminishing the SCL photocurrent through thermal annealing.[256]

Given that hybrid solar cells typically consist of inorganic n-type semiconductors with high electron mobility (e.g. TiO_2 (0.1-1 cm^2 V^{-1} s^{-1}) [286], ZnO (200-300 cm^2 V^{-1} s^{-1}) [287]), and organic polymers with low hole mobility (e.g. P3HT ($10^{-6} - 10^{-4}$ cm^2 V^{-1} s^{-1}) [288, 289], PCPDTBT ($10^{-4} - 10^{-3}$ cm^2 V^{-1} s^{-1}) [290], they therefore exhibit a large mobility discrepancy in the system. This raises the question as to how the charge carrier mobility influences the space-charge formation as well as the device performance.

Our former group members have successfully developed various semiconductor nanowire arrays and applied them in hybrid solar cells. In particular, James Dorman et al. have developed an interest in improving exciton dissociation at organic/inorganic interface via semiconductor Sn:TiO_2|TiO_2 core-shell nanowires, which has beneficial cascading energy levels.[37] Very recently, Chaw loon Thu et al. have found space-charge limit current effects in Sn doped ZnO (Sn: ZnO) nanowire based hybrid solar cells, due to unbalanced charge transport in the device.

To gain further insight into space-charge limit current effects, the novel free-standing silver nanowire arrays would be the best choice. This is because AgNW arrays presents

unique possibilities to tune their own electronic properties. For example, when placed under sulfur vapor atmosphere, the color of AgNWs changed from blue-greenish to dark, indicating the formation of Ag_2S. The absorption spectra of the pure AgNW arrays and sulfurized AgNW arrays are shown in Figure D3a in Appendix D. For the sulfurized AgNW curve, there is a clear absorption taking off sharply at 800 nm, indicating the bandgap of this material is ca. 1.55 eV (Tauc relation). Hence, this simple sulfurization method dramatically changed the metallic nanowires to semiconducting nanowires. Another example is that the electronic property of the AgNWs can also be tuned via short time exposure to O_2 plasma. The photoemission spectroscopy measurement results (Figure D3b in Appendix D) show that the surface ionization potential is changed from 4.77 eV to 5.14 eV after 1.2 s of O_2 plasma treatment, indicating that a AgOx shell is formed. Preliminary experiments open new possibilities to combine the electronic tunable AgNWs with charge transport studies of hybrid solar cells. In the future, it would be interesting to systematically control of charge carrier mobility in hybrid solar cells by using a core-shell nanowire with a Ag core and varying shells (e.g. Ag_2S, AgOx, TiO_2 and ZnO), in order to draw general conclusions about how an ideal hybrid interface should be designed to overcome current limitations.

A. Appendix to Section 3.2

Figure A1a shows the linear relationship of pore widening speed with respect to time (0.72 nm/min), and Figure A1b shows the linear relationship of interpore distance with respect to anodizing voltage (1.9 nm/V) for AAO templates on ITO glass.

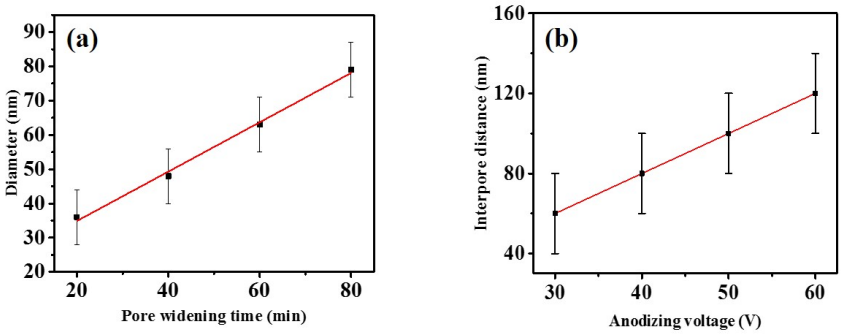

Figure A1.: (a) Diameter vs. pore-widening time at room temperature for AAOs on ITO glass anodized at 60 V.(b) Interpore distance vs. anodizing voltage for AAOs on ITO glass.

B. Appendix to Section 3.3

Figure B1 shows electroformed dentritic silver. Such rough microstructures are undesirable for homogeneously filling the nano-AAO pores. However, it could be useful as e.g. electrodes for thick polymer solar cells due to its good charge collection efficiency.[291]

Figure B2 shows a HR-TEM image of the electrodeposited silver nanowires. The distance between two neighboring lines is 0.234 nm, which is identical to the d-spacing value (0.234 nm) along the (111) direction for silver. This result further verifies the successful growth of the silver nanowires.

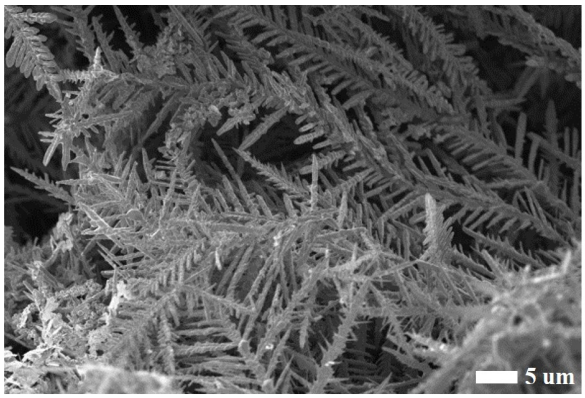

Figure B1.: SEM top view of potentiostatically deposited silver micro-leaves on ITO glass from 3 mM $AgNO_3$ + 0.2 M KNO_3 (aq) at -0.15 V for 30 min.

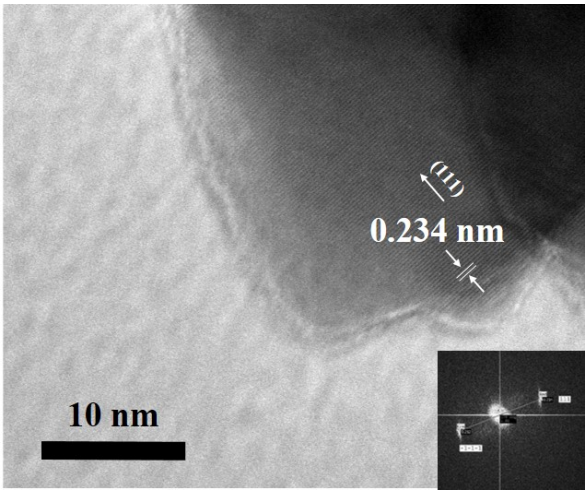

Figure B2.: HR-TEM image of the electrodeposited silver nanowires. The distance between two neighboring lines is 0.234 nm, which is identical to the d-spacing value (0.234 nm) along the (111) direction for silver.

C. Appendix to Section 4.3

Figure C1 shows the transmittance of Au (2 nm) /Ti (5 nm) /ITO glass, referring to 100% transmittance of pure ITO glass. With additional Au and Ti layers, the overall transmittance level (integral from 350 nm to 650 nm) losses 34% in comparison to pure ITO glass. Such loss percentage is comparable to the EQE loss (36%). The slight difference could be attributed to the fluctuation of the sputtered Au and Ti's thickness in different batches.

Figure C2 shows the J-V curves and characteristic values of the standard semi-transparent P3HT:PCBM solar cells. The fabrication procedure follows the optimized conditions described in Section 4.1, except for the transparent top electrode, which was made by Yoonseok Park in Prof. Karl Leo's group in Dresden University of Technology. The J-V characteristics show no significant difference in terms of V_{OC} and FF when the solar cells are illuminated from different directions. However, J_{SC} for top illumination through Ca:Ag electrode (3.33 mA/cm^2) is lower than the 4.40 mA/cm^2 for bottom illumination through ITO glass. The reason for such 30% difference of J_{SC} is that the metallic Ca:Ag electrode acts as a better back-reflector than ITO electrode, resulting in an enhanced optical absorption in the active layer when the solar cells are bottom illuminated through ITO glass.[240] Consequently, the power conversion efficiency (PCE) for top illumination through Ca:Ag electrode (0.74%) is lower than the 1.01% for bottom illumination through ITO glass (i.e., 27% of efficiency drop).

Figure C3 display the normalized EQE of AgNW (250 nm)-OSCs and flat-OSCs from bottom and top illumination directions.

Figure C4 display the J-V characteristics of AgNW-OSCs and flat-OSCs from different illumination directions as a function of incident light intensity.

Figures C5a-b display the first derivatives of the J-(V_{OC}-V) curves from Figure 4.18, calculated by a self-written Matlab program, using a loop of a polyfit, $y = ax + b$, at each three adjacent points.

Figures C6a-b display the photogenerated current density J as a function of the effective voltage V_{OC}-V, and the corresponding first derivative curves for AgNW (250 nm)-OSCs and flat-OSCs.

Figures C7a-b display the dependence of the FF on the light-intensity for two different batches of solar cells. In Figure C7a for AgNW (130 nm)-OSCs and flat-OSCs,

the FF does not drop with decreasing the light-intensity in the whole range of 5-83 mW/cm^2, and therefore the fitting of the V_{OC} vs. light-intensity in Figure 4.19 from 5 to 83 mW/cm^2 is valid. However, in Figure C7b for AgNW (250 nm)-OSCs and flat-OSCs, the FF starts dropping below 44 mW/cm^2 for AgNW (250 nm)-OSCs, and therefore the fitting range of V_{OC} vs. light-intensity is chosen as above 44 mW/cm^2.[272]

Figures C8 shows the experimental and fitting data of the V_{OC} vs. light-intensity for AgNW (250 nm)-OSCs and flat-OSCs. The ideality factor n is over 2 for all cases.
dsdsf

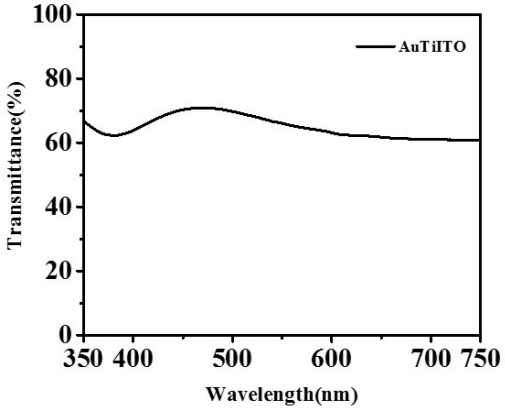

Figure C1.: The transmittance spectrum of Au (2 nm) /Ti (5 nm) /ITO glass, referring to 100% transmittance of pure ITO glass.

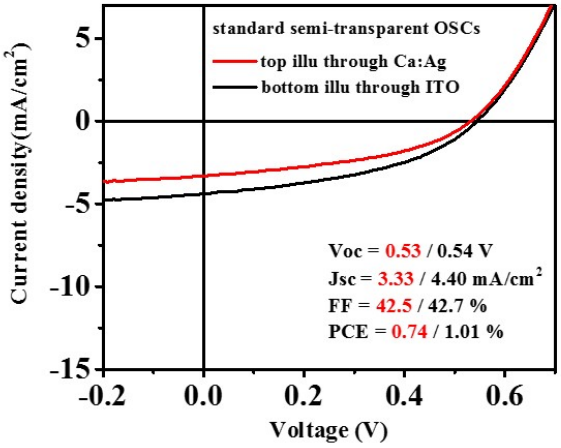

Figure C2.: The J-V curves and characteristic values of the standard semi-transparent P3HT:PCBM solar cells.

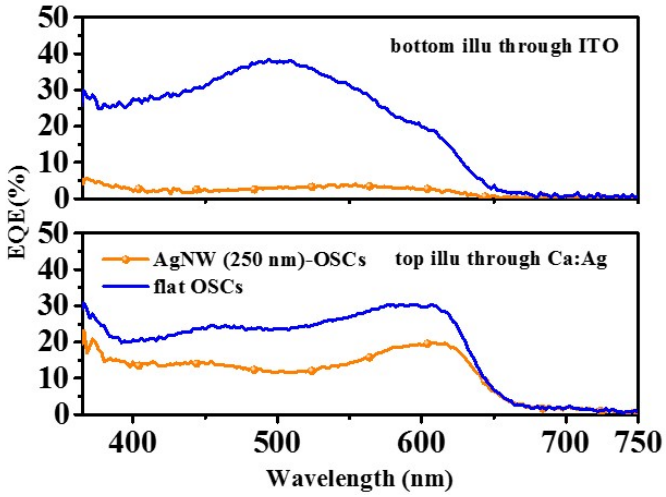

Figure C3.: Normalized EQE of AgNW (250 nm)-OSCs and flat-OSCs from bottom and top illumination directions.

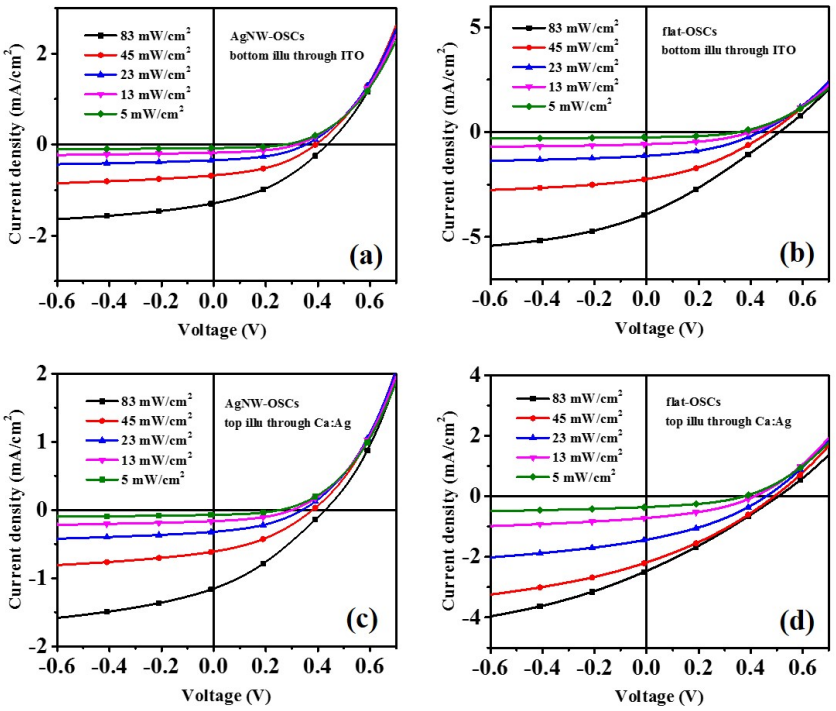

Figure C4.: (a) J-V characteristics of AgNW (130 nm)-OSCs under bottom illumination through ITO glass as a function of incident light intensity. (b) J-V characteristics of flat-OSCs under bottom illumination through ITO glass as a function of incident light intensity. (c) J-V characteristics of AgNW (130 nm)-OSCs under top illumination through Ca:Ag as a function of incident light intensity. (d) J-V characteristics of flat-OSCs under top illumination through Ca:Ag as a function of incident light intensity.

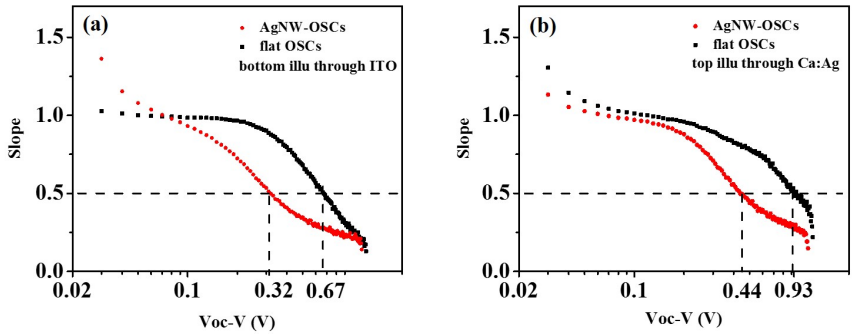

Figure C5.: The first derivatives of the J-(V_{OC}-V) curves from Figure 4.18, calculated by a self-written Matlab program, using a loop of a polyfit, $y = ax + b$, at each three adjacent points. The dashed lines mark the square-root dependent points. (a) AgNW (130 nm)-OSCs and flat-OSCs under bottom illumination through ITO glass. (b) AgNW (130 nm)-OSCs and flat-OSCs under top illumination through Ca:Ag electrode.

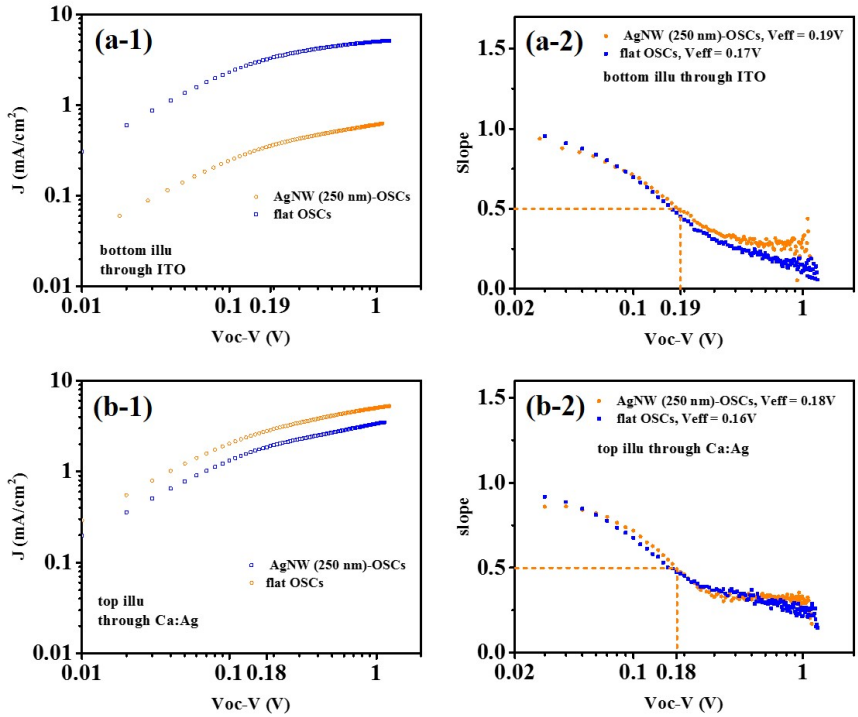

Figure C6.: (a-1) Photogenerated current density J as a function of the effective voltage V_{OC}-V, for AgNW (250 nm)-OSCs and flat-OSCs under bottom illumination through ITO glass. (a-2) The first derivatives of the J-(V_{OC}-V) curve in (a-1). (b-1) Photogenerated current density J as a function of the effective voltage V_{OC}-V, for AgNW (250 nm)-OSCs and flat-OSCs under top illumination through Ca:Ag electrode. (b-2) The first derivatives of the J-(V_{OC}-V) curve in (b-1). The illumination light intensity is 80 mW/cm^2.

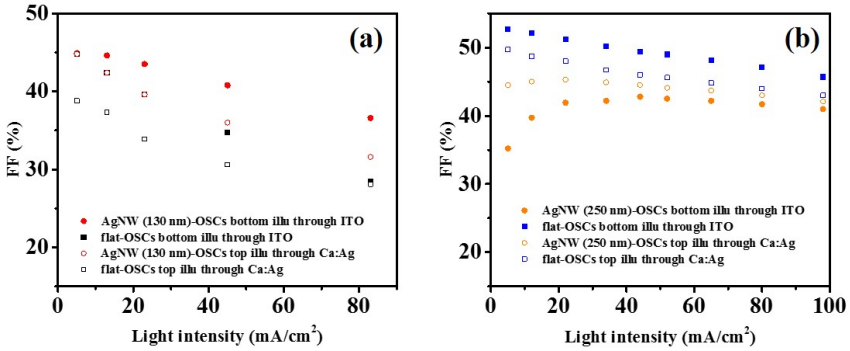

Figure C7.: (a) Light-intensity dependence of fill factor (FF) for AgNW (130 nm)-OSCs and flat-OSCs from different illumination directions. (b) Light intensity dependence of fill factor (FF) for AgNW (250 nm)-OSCs and flat-OSCs from different illumination directions. The results of these two batches of solar cells are statistically independent, as they were made on different days.

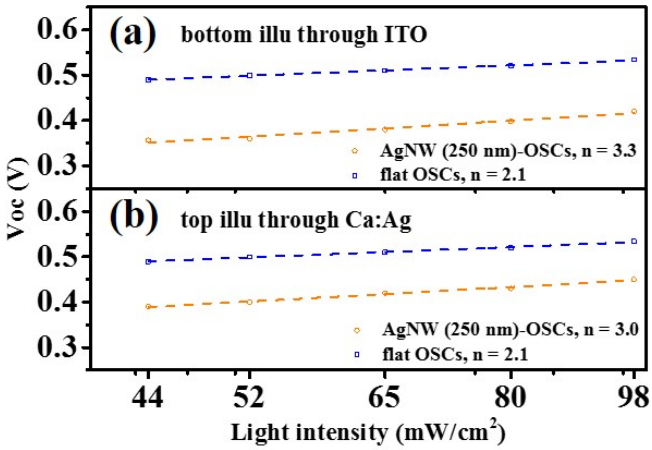

Figure C8.: (a) Light intensity dependence of open-circuit voltage (V_{OC}) for AgNW (250 nm)-OSCs and flat-OSCs under bottom illumination through ITO glass on a linear/logarithmic ($ln(I)$) scale. The straight lines show fits to $V_{OC}(I) \propto 0.025 \cdot n \cdot ln(I)$. (b) Light intensity dependence of open-circuit voltage (V_{OC}) for AgNW (250 nm)-OSCs and flat-OSCs under top illumination through Ca:Ag electrode on a linear/logarithmic ($ln(I)$) scale. The straight lines show fits to $V_{OC}(I) \propto 0.025 \cdot n \cdot ln(I)$.

D. Appendix to Section 5

Figures D1a-b demonstrate our homemade temperature-resolved UV-Vis setup in a both of a schematic and real status way.

Figures D2a shows the temperature-dependent transmission of a AgNWs-AAO sample, measured under a transmission mode. Figures D2b shows the angle-dependent reflection of a AgNWs-AAO sample, measured under a reflection mode at room temperature. Note that the actual temperature on the sample surface is expected a bit higher than room temperature due to the heating effect of the incident light beam.

Figure D3a shows absorption spectra of free-standing AgNWs before and after sulfurization (30 min), respectively. We can see that for the sulfurized AgNWs, there a clear absorption taking off sharply at 800 nm, indicating a bandgap of 1.55 eV. Therefore, the simple sulfurization method can dramatically change the metallic nanowire arrays to semiconductor nanowire arrays.

Figure D3b shows photoelectron spectroscopy in air (PESA) spectra of free-standing AgNWs before and after O_2 plasma (1.2 s) treatment. We can see that with a short time of O_2 plasma treatment, the surface ionization potential for nanowire arrays increases from 4.77 eV to 5.14 eV, indicating a formation of AgOx shell.

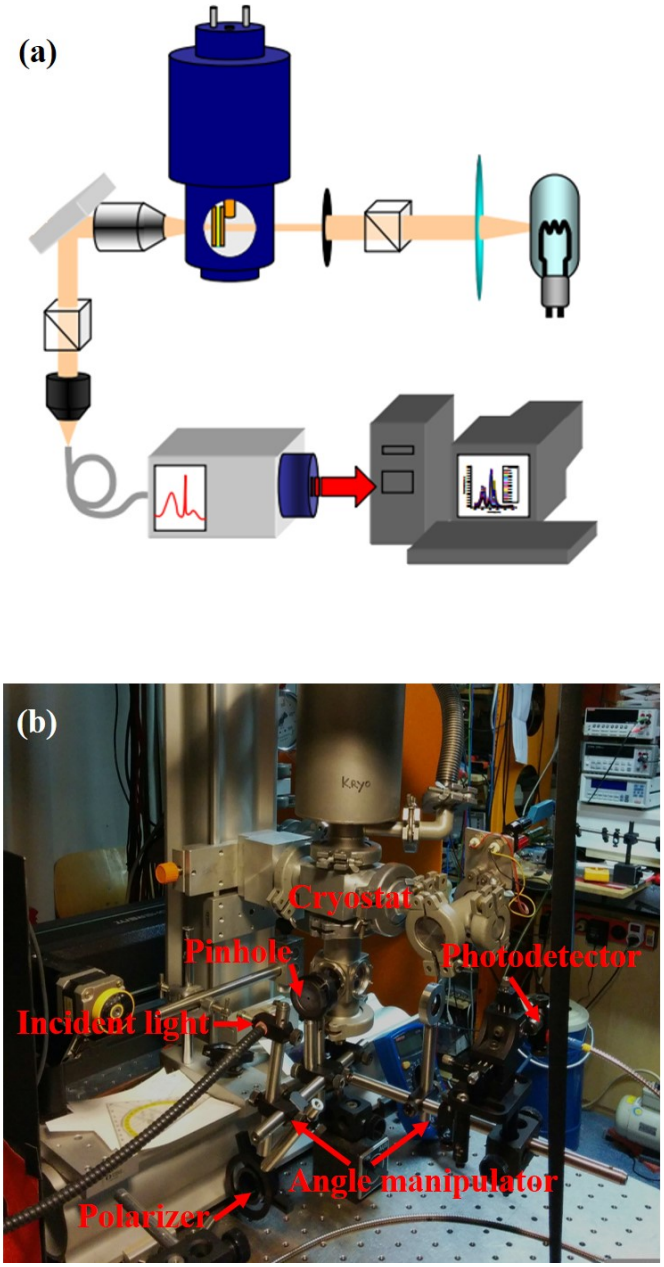

Figure D1.: (a) Schematic illustration of temperature&angle-resolved UV-Vis setup, adapted from Bouillard et al.[283] A light beam from a Tungsten lamp passes through a polarizer before illuminating the sample. The pinhole is used to reduce the beam size. The sample is installed inside of a cryostat. In the case of the transmission mode, the transmitted light is focused by a lens and then collected by a wavelength-resolved photodetector. In the case of the reflection mode, the reflected light from the sample surface is focused by a lens and then collected by a wavelength-resolved photodetector. (b) Photo of the homemade temperature-resolved UV-Vis setup.

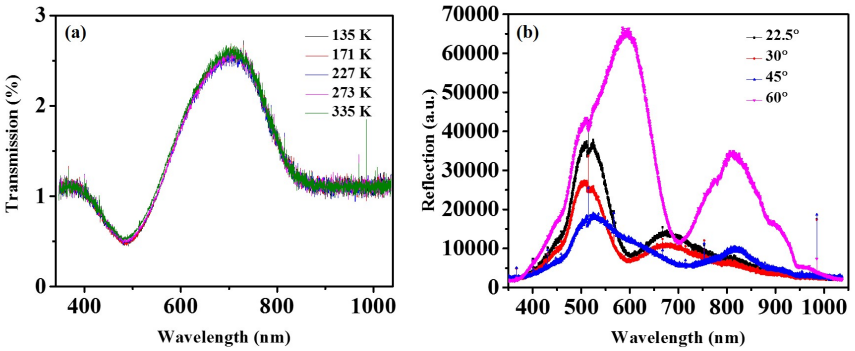

Figure D2.: (a) Temperature-dependent transmission of a AgNWs-AAO sample, measured using non-polarized light at 135,171,227,273, and 335 K. (b) Reflection spectra measured of a AgNWs-AAO sample using p-polarized incident light for various of angle of incidence at 22.5°, 30°, 45°, and 60° at room temperature.

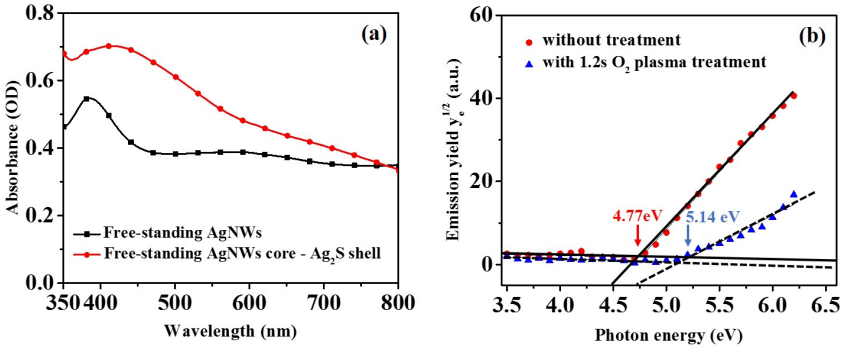

Figure D3.: (a) Absorption spectra of free-standing AgNWs before and after sulfurization (30 min), respectively. (b) Photoelectron Spectroscopy in Air (PESA) spectra of free-standing AgNWs before and after O_2 plasma (1.2 s) treatment. The ionization potential is calculated from the two intersections of the background line and the signal regression line.

Bibliography

[1] Michael Graetzel. Solar energy conversion by dye-sensitized photovoltaic cells. *Inorganic chemistry*, 44(20):6841–6851, 2005.

[2] International Energy Agency. Renewables information (2016 edition).

[3] Qiaoqiang Gan, Filbert J Bartoli, and Zakya H Kafafi. Plasmonic-enhanced organic photovoltaics: Breaking the 10% efficiency barrier. *Advanced materials*, 25(17):2385–2396, 2013.

[4] Matthew C Beard, Joseph M Luther, and Arthur J Nozik. The promise and challenge of nanostructured solar cells. *Nature nanotechnology*, 9(12):951–954, 2014.

[5] Peter Peumans, Aharon Yakimov, and Stephen R Forrest. Small molecular weight organic thin-film photodetectors and solar cells. *Journal of Applied Physics*, 93(7):3693–3723, 2003.

[6] Konarka thin film solar cells. `http://evworld.com/news.cfm?rssid=26699`. Accessed: 18.10.2016.

[7] Smart forvision. `http://bright-cars.com/photo/smart-forvision/09/default.html`. Accessed:18.10.2016.

[8] Swisstech convention center. `http://www.cute.kiwi/swiss-tech-convention-center/`. Accessed: 18.10.2016.

[9] Zhicai He, Biao Xiao, Feng Liu, Hongbin Wu, Yali Yang, Steven Xiao, Cheng Wang, Thomas P Russell, and Yong Cao. Single-junction polymer solar cells with high efficiency and photovoltage. *Nature Photonics*, 9(3):174–179, 2015.

[10] Corsin Battaglia, Andres Cuevas, and Stefaan De Wolf. High-efficiency crystalline silicon solar cells: status and perspectives. *Energy & Environmental Science*, 9(5):1552–1576, 2016.

[11] Girish Lakhwani, Akshay Rao, and Richard H. Friend. Bimolecular recombination in organic photovoltaics. *Annual Review of Physical Chemistry*, 65(1):557–581, 2014.

[12] Antonio Facchetti. Polymer donor–polymer acceptor (all-polymer) solar cells. *Materials Today*, 16(4):123–132, 2013.

[13] Gilles Dennler, Markus C Scharber, and Christoph J Brabec. Polymer-fullerene bulk-heterojunction solar cells. *Advanced Materials*, 21(13):1323–1338, 2009.

[14] R. A. J. Janssen and J. Nelson. Factors limiting device efficiency in organic photovoltaics. *Advanced Materials*, 25(13):1847–1858, 2013.

[15] L. Schmidt-Mende and J. Weickert. *Organic and Hybrid Solar Cells: An Introduction*. De Gruyter, 2016.

[16] Heinz Baessler and Anna Koehler. Charge transport in organic semiconductors. In *Unimolecular and supramolecular electronics I*, pages 1–65. Springer, 2011.

[17] Jun Hong Noh, Hyun Soo Han, Sangwook Lee, Jin Young Kim, Kug Sun Hong, Gil-Sang Han, Hyunjung Shin, and Hyun Suk Jung. Nanowire-based three-dimensional transparent conducting oxide electrodes for extremely fast charge collection. *Advanced Energy Materials*, 1(5):829–835, 2011.

[18] Zhiyong Fan, Haleh Razavi, Jae-won Do, Aimee Moriwaki, Onur Ergen, Yu-Lun Chueh, Paul W. Leu, Johnny C. Ho, Toshitake Takahashi, Lothar A. Reichertz, Steven Neale, Kyoungsik Yu, Ming Wu, Joel W. Ager, and Ali Javey. Three-dimensional nanopillar-array photovoltaics on low-cost and flexible substrates. *Nat Mater*, 8(8):648–653, 2009. 10.1038/nmat2493.

[19] Diana C Iza, David Munoz-Rojas, Kevin P Musselman, Jonas Weickert, Andreas C Jakowetz, Haiyan Sun, Xin Ren, Robert LZ Hoye, Joon H Lee, Haiyan Wang, et al. Nanostructured conformal hybrid solar cells: a promising architecture towards complete charge collection and light absorption. *Nanoscale research letters*, 8(1):1, 2013.

[20] Ching-Mei Hsu, Corsin Battaglia, Celine Pahud, Zhichao Ruan, Franz-Josef Haug, Shanhui Fan, Christophe Ballif, and Yi Cui. High-efficiency amorphous silicon solar cell on a periodic nanocone back reflector. *Advanced Energy Materials*, 2(6):628–633, 2012.

[21] Ken Xingze Wang, Zongfu Yu, Victor Liu, Yi Cui, and Shanhui Fan. Absorption enhancement in ultrathin crystalline silicon solar cells with antireflection and light-trapping nanocone gratings. *Nano letters*, 12(3):1616–1619, 2012.

[22] Dong Liang, Yijie Huo, Yangsen Kang, Ken Xingze Wang, Anjia Gu, Meiyueh Tan, Zongfu Yu, Shuang Li, Jieyang Jia, Xinyu Bao, et al. Optical absorption enhancement in freestanding gaas thin film nanopyramid arrays. *Advanced Energy Materials*, 2(10):1254–1260, 2012.

[23] Tao Song, Fute Zhang, Xiaofei Lei, Yonglan Xu, Shuittong Lee, and Baoquan Sun. Core–shell structured photovoltaic devices based on pbs quantum dots and silicon nanopillar arrays. *Nanoscale*, 4(4):1336–1343, 2012.

[24] Anastassios Mavrokefalos, Sang Eon Han, Selcuk Yerci, Matthew S Branham, and Gang Chen. Efficient light trapping in inverted nanopyramid thin crystalline silicon membranes for solar cell applications. *Nano letters*, 12(6):2792–2796, 2012.

[25] Sangmoo Jeong, Erik C Garnett, Shuang Wang, Zongfu Yu, Shanhui Fan, Mark L Brongersma, Michael D McGehee, and Yi Cui. Hybrid silicon nanocone–polymer solar cells. *Nano letters*, 12(6):2971–2976, 2012.

[26] Qingfeng Lin, Bo Hua, Siu-fung Leung, Xicheng Duan, and Zhiyong Fan. Efficient light absorption with integrated nanopillar/nanowell arrays for three-dimensional thin-film photovoltaic applications. *ACS nano*, 7(3):2725–2732, 2013.

[27] Hao Lin, Ho-Yuen Cheung, Fei Xiu, Fengyun Wang, SenPo Yip, Ning Han, TakFu Hung, Jun Zhou, Johnny C Ho, and Chun-Yuen Wong. Developing controllable anisotropic wet etching to achieve silicon nanorods, nanopencils and nanocones for efficient photon trapping. *Journal of Materials Chemistry A*, 1(34):9942–9946, 2013.

[28] Qingfeng Lin, Siu-Fung Leung, Linfeng Lu, Xiaoyuan Chen, Zhuo Chen, Haoning Tang, Wenjun Su, Dongdong Li, and Zhiyong Fan. Inverted nanocone-based thin film photovoltaics with omnidirectionally enhanced performance. *ACS nano*, 8(6):6484–6490, 2014.

[29] Jeong-Gil Kim, Hyungryul J Choi, Kyoo-Chul Park, Robert E Cohen, Gareth H McKinley, and George Barbastathis. Multifunctional inverted nanocone arrays for non-wetting, self-cleaning transparent surface with high mechanical robustness. *Small*, 10(12):2487–2494, 2014.

[30] Jonas Weickert, Ricky B Dunbar, Holger C Hesse, Wolfgang Wiedemann, and Lukas Schmidt-Mende. Nanostructured organic and hybrid solar cells. *Advanced Materials*, 23(16):1810–1828, 2011.

[31] Erik C Garnett, Mark L Brongersma, Yi Cui, and Michael D McGehee. Nanowire solar cells. *Annual Review of Materials Research*, 41:269–295, 2011.

[32] Qifeng Zhang and Guozhong Cao. Nanostructured photoelectrodes for dye-sensitized solar cells. *Nano Today*, 6(1):91–109, 2011.

[33] Yuyi Feng, Kwang-Dae Kim, Clayton A Nemitz, Paul Kim, Thomas Pfadler, Melanie Gerigk, Sebastian Polarz, James A Dorman, Jonas Weickert, and Lukas Schmidt-Mende. Uniform large-area free-standing silver nanowire arrays on transparent conducting substrates. *Journal of The Electrochemical Society*, 163(8):D447–D452, 2016.

[34] N. O. V. Plank, H. J. Snaith, C. Ducati, J. S. Bendall, L. Schmidt Mende, and M. E. Welland. A simple low temperature synthesis route for zno mgo core shell nanowires. *Nanotechnology*, 19(46), 2008.

[35] Lori E. Greene, Matt Law, Benjamin D. Yuhas, and Peidong Yang. Zno tio2 core shell nanorod/p3ht solar cells. *The Journal of Physical Chemistry C*, 111(50):18451–18456, 2007.

[36] Matt Law, Lori E. Greene, Aleksandra Radenovic, Tevye Kuykendall, Jan Liphardt, and Peidong Yang. Zno al2o3 and zno tio2 core shell nanowire dye sensitized solar cells. *The Journal of Physical Chemistry B*, 110(45):22652–22663, 2006.

[37] James A. Dorman, Jonas Weickert, Julian B. Reindl, Martin Putnik, Andreas Wisnet, Matthias Noebels, Christina Scheu, and Lukas Schmidt-Mende. Control of recombination pathways in tio2 nanowire hybrid solar cells using sn4+ dopants. *The Journal of Physical Chemistry C*, 118(30):16672–16679, 2014.

[38] Ricky B Dunbar, Thomas Pfadler, Niraj N Lal, Jeremy J Baumberg, and Lukas Schmidt-Mende. Imprinting localized plasmons for enhanced solar cells. *Nanotechnology*, 23(38):385202, 2012.

[39] Lin Li Sam Zhang and Ashok Kumar. *Materials Characterization Techniques*. CRC Press, 2009.

[40] J.O. Agumba. *Design and fabrication of a simple four point probe system for electrical characterization of thin films*. PhD thesis, Kenyatta University, 2010.

[41] H.C.Hesse. *Supramolecular assembly and nanoscale morphologies for organic photovoltaic devices*. PhD thesis, 2011.

[42] Eugen Zimmermann, Philipp Ehrenreich, Thomas Pfadler, James A Dorman, Jonas Weickert, and Lukas Schmidt-Mende. Erroneous efficiency reports harm organic solar cell research. *Nature Photonics*, 8(9):669–672, 2014.

[43] Henry J Snaith. How should you measure your excitonic solar cells? *Energy & Environmental Science*, 5(4):6513–6520, 2012.

[44] J Manara, M Reidinger, M Rydzek, and M Arduini-Schuster. Polymer-based pigmented coatings on flexible substrates with spectrally selective characteristics to improve the thermal properties. *Progress in Organic Coatings*, 70(4):199–204, 2011.

[45] Erin P Stuckert, Roy H Geiss, Christopher J Miller, and Ellen R Fisher. In-depth view of the structure and growth of sno2 nanowires and nanobrushes. *ACS Applied Materials & Interfaces*, 2016.

[46] Philipp Paulitschke, Norbert Seltner, Alexander Lebedev, Heribert Lorenz, and Eva Maria Weig. Size-independent young's modulus of inverted conical gaas nanowire resonators. *Applied Physics Letters*, 103(26):261901, 2013.

[47] Habib Hamidinezhad, Ali Akbar Ashkarran, and Zulkurnain Abdul-Malek. The role of silane gas flow rate on pecvd-assisted fabrication of silicon nanowires. *Applied Physics A*, 122(3):1–7, 2016.

[48] David A Gregory, Yu Zhang, Patrick J Smith, Xiubo Zhao, and Stephen J Ebbens. Reactive inkjet printing of biocompatible enzyme powered silk micro-rockets. *Small*, 12(30):4048–4055, 2016.

[49] GAO Yuan, Yuanjing Lin, CHEN Jiaqi, Qingfeng Lin, Yue Wu, SU Wenjun, Wenli Wang, and Zhiyong Fan. Three-dimensional nanotube electrode arrays for hierarchical tubular structured high-performance pseudocapacitors. *Nanoscale*, 2016.

[50] Zhe Gui, Eleanor Gillette, Jonathon Duay, Junkai Hu, Nam Kim, and Sang Bok Lee. Co-electrodeposition of ruo 2–mno 2 nanowires and the contribution of ruo 2 to the capacitance increase. *Physical Chemistry Chemical Physics*, 17(23):15173–15180, 2015.

[51] Thomas Pfadler, Mihael Coric, Claudia M Palumbiny, Andreas C Jakowetz, Karl-Philipp Strunk, James A Dorman, Philipp Ehrenreich, Cheng Wang, Alexander Hexemer, and Rui-Qi Png. Influence of interfacial area on exciton separation and polaron recombination in nanostructured bilayer all-polymer solar cells. *ACS nano*, 8(12):12397–12409, 2014.

[52] Lukas Schmidt-Mende and Judith L MacManus-Driscoll. Zno–nanostructures, defects, and devices. *Materials today*, 10(5):40–48, 2007.

[53] Andreas Wisnet, Katarina Bader, Simon B Betzler, Matthias Handloser, Philipp Ehrenreich, Thomas Pfadler, Jonas Weickert, Achim Hartschuh, Lukas Schmidt-Mende, Christina Scheu, et al. Defeating loss mechanisms in 1d tio2-based hybrid solar cells. *Advanced Functional Materials*, 25(17):2601–2608, 2015.

[54] Qiu Yang, Zhiyi Lu, Junfeng Liu, Xiaodong Lei, Zheng Chang, Liang Luo, and Xiaoming Sun. Metal oxide and hydroxide nanoarrays: Hydrothermal synthesis and applications as supercapacitors and nanocatalysts. *Progress in Natural Science: Materials International*, 23(4):351–366, 2013.

[55] Hongkuan Wang, Wenzao Li, Huifang Fei, Liping Guo, Jinkui Feng, Lijie Ci, and Shenglin Xiong. Facile hydrothermal growth of vo 2 nanowire, nanorod and nanosheet arrays as binder free cathode materials for sodium batteries. *RSC Advances*, 6(17):14314–14320, 2016.

[56] Matthew R. Jones, Kyle D. Osberg, Robert J. Macfarlane, Mark R. Langille, and Chad A. Mirkin. Templated techniques for the synthesis and assembly of plasmonic nanostructures. *Chemical Reviews*, 111(6):3736–3827, 2011.

[57] Yiding Liu, James Goebl, and Yadong Yin. Templated synthesis of nanostructured materials. *Chemical Society Reviews*, 42(7):2610–2653, 2013.

[58] Umair Yaqub Qazi and Rahat Javaid. A review on metal nanostructures: Preparation methods and their potential applications. *Advances in Nanoparticles*, 5(01):27, 2016.

[59] Reginald M. Penner and Charles R. Martin. Preparation and electrochemical characterization of ultramicroelectrode ensembles. *Analytical Chemistry*, 59(21):2625–2630, 1987.

[60] H. Schwanbeck and U. Schmidt. Preparation and characterisation of magnetic nanostructures using filtration membranes. *Electrochimica Acta*, 45(27):4389–4398, 2000.

[61] S. Valizadeh, J. M. George, P. Leisner, and L. Hultman. Electrochemical synthesis of ag/co multilayered nanowires in porous polycarbonate membranes. *Thin Solid Films*, 402(1-2):262–271, 2002.

[62] IU Schuchert, ME Toimil Molares, D Dobrev, J Vetter, R Neumann, and M Martin. Electrochemical copper deposition in etched ion track membranes experimental results and a qualitative kinetic model. *Journal of the Electrochemical Society*, 150(4):C189–C194, 2003.

[63] Jinglai Duan, Jie Liu, Yongliang Zhang, Christina Trautmann, and Dang Yuan Lei. Surface plasmonic spectroscopy revealing the oxidation dynamics of copper nanowires embedded in polycarbonate ion-track templates. *Journal of Materials Chemistry C*, 4(18):3956–3962, 2016.

[64] Falk Muench, Eva-Maria Felix, Markus Rauber, Sandra Schaefer, Markus Antoni, Ulrike Kunz, Hans-Joachim Kleebe, Christina Trautmann, and Wolfgang Ensinger. Electrodeposition and electroless plating of hierarchical metal superstructures composed of 1d nano-and microscale building blocks. *Electrochimica Acta*, 202:47–54, 2016.

[65] David A Olson, Liang Chen, and Marc A Hillmyer. Templating nanoporous polymers with ordered block copolymers†. *Chemistry of Materials*, 20(3):869–890, 2007.

[66] Jeong In Lee, Shin Hyo Cho, Su-Moon Park, Jin Kon Kim, Jai Kyeong Kim, Jae-Woong Yu, Young Chul Kim, and Thomas P. Russell. Highly aligned ultrahigh density arrays of conducting polymer nanorods using block copolymer templates. *Nano Letters*, 8(8):2315–2320, 2008.

[67] Edward JW Crossland, Marleen Kamperman, Mihaela Nedelcu, Caterina Ducati, Ulrich Wiesner, Detlef-M Smilgies, Gilman ES Toombes, Marc A Hillmyer, Sabine Ludwigs, Ullrich Steiner, et al. A bicontinuous double gyroid hybrid solar cell. *Nano letters*, 9(8):2807–2812, 2008.

[68] Julie NL Albert and Thomas H Epps. Self-assembly of block copolymer thin films. *Materials Today*, 13(6):24–33, 2010.

[69] Hideaki Komiyama, Motonori Komura, Yuka Akimoto, Kaori Kamata, and Tomokazu Iyoda. Longitudinal and lateral integration of conducting polymer nanowire arrays via block-copolymer-templated electropolymerization. *Chemistry of Materials*, 27(14):4972–4982, 2015.

[70] Hideaki Komiyama, Tomokazu Iyoda, and Takanobu Sanji. Metal nanodot arrays fabricated via seed-mediated electroless plating with block copolymer thin film scaffolding. *Nanotechnology*, 26(39):395302, 2015.

[71] Parvaneh Mokarian-Tabari, Catalina Vallejo-Giraldo, Marc Fernandez-Yague, Cian Cummins, Michael A Morris, and Manus JP Biggs. Nanoscale neuroelectrode modification via sub-20 nm silicon nanowires through self-assembly of block copolymers. *Journal of Materials Science: Materials in Medicine*, 26(2):1–5, 2015.

[72] Wei Wei, Leith Samad, Jonathan W Choi, Yongho Joo, Austin Way, Michael S Arnold, Song Jin, and Padma Gopalan. Synthesis of molybdenum disulfide nanowire arrays using a block copolymer template. *Chemistry of Materials*, 2016.

[73] B Notario, J Pinto, and MA Rodriguez-Perez. Nanoporous polymeric materials: A new class of materials with enhanced properties. *Progress in Materials Science*, 78:93–139, 2016.

[74] Pawel Pieranski, L Strzelecki, and B Pansu. Thin colloidal crystals. *Physical Review Letters*, 50(12):900, 1983.

[75] N Denkov, O Velev, P Kralchevski, I Ivanov, Hideyuki Yoshimura, and Kuniaki Nagayama. Mechanism of formation of two-dimensional crystals from latex particles on substrates. *Langmuir*, 8(12):3183–3190, 1992.

[76] Kyusoon Shin, K Amanda Leach, James T Goldbach, Dong Ha Kim, Jae Young Jho, Mark Tuominen, Craig J Hawker, and Thomas P Russell. A simple route to metal nanodots and nanoporous metal films. *nano letters*, 2(9):933–936, 2002.

[77] Adam Kosiorek, Witold Kandulski, Hanna Glaczynska, and Michael Giersig. Fabrication of nanoscale rings, dots, and rods by combining shadow nanosphere lithography and annealed polystyrene nanosphere masks. *Small*, 1(4):439–444, 2005.

[78] Laura E Hennemann, Andreas Kolloch, Andreas Kern, Josip Mihaljevic, Johannes Boneberg, Paul Leiderer, Alfred J Meixner, and Dai Zhang. Assessing the plasmonics of gold nano-triangles with higher order laser modes. *Beilstein journal of nanotechnology*, 3(1):674–683, 2012.

[79] Nicolas Vogel, Markus Retsch, Charles-Andre Fustin, Aranzazu del Campo, and Ulrich Jonas. Advances in colloidal assembly: the design of structure and hierarchy in two and three dimensions. *Chemical reviews*, 115(13):6265–6311, 2015.

[80] Bin Ai, Helmuth Möhwald, Dayang Wang, and Gang Zhang. Advanced colloidal lithography beyond surface patterning. *Advanced Materials Interfaces*, 2016.

[81] Takazumi Ohno, Carl Wadell, Satoshi Inagaki, Ji Shi, Yoshio Nakamura, Sachiko Matsushita, and Takumi Sannomiya. Hole-size tuning and sensing performance of hexagonal plasmonic nanohole arrays. *Optical Materials Express*, 6(5):1594–1603, 2016.

[82] Lei Zhang, Xiaolan Zhong, Egon Pavlica, Songlin Li, Alexander Klekachev, Gvido Bratina, Thomas W Ebbesen, Emanuele Orgiu, and Paolo Samorì. A nanomesh scaffold for supramolecular nanowire optoelectronic devices. *Nature Nanotechnology*, 2016.

[83] Christy L Haynes and Richard P Van Duyne. Nanosphere lithography: a versatile nanofabrication tool for studies of size-dependent nanoparticle optics. *The Journal of Physical Chemistry B*, 105(24):5599–5611, 2001.

[84] T. M. Whitney, P. C. Searson, J. S. Jiang, and C. L. Chien. Fabrication and magnetic properties of arrays of metallic nanowires. *Science*, 261(5126):1316–1319, 1993.

[85] Hideki Masuda. Ordered metal nanohole arrays made by a two-step replication of honeycomb structures of anodic alumina. *Science*, 268:1466–1468, 1995.

[86] K. Nielsch, F. Müller, A. P. Li, and U. Gösele. Uniform nickel deposition into ordered alumina pores by pulsed electrodeposition. *Advanced Materials*, 12(8):582–586, 2000.

[87] M. E. Toimil-Molares, V. Buschmann, D. Dobrev, R. Neumann, R. Scholz, I. U. Schuchert, and J. Vetter. Single-crystalline copper nanowires produced by electrochemical deposition in polymeric ion track membranes. *Advanced Materials*, 13(1):62–+, 2001.

[88] Mingliang Tian, Shengyong Xu, Jinguo Wang, Nitesh Kumar, Eric Wertz, Qi Li, Paul M. Campbell, Moses H. W. Chan, and Thomas E. Mallouk. Penetrating the oxide barrier in situ and separating freestanding porous anodic alumina films in one step. *Nano Letters*, 5(4):697–703, 2005.

[89] Mojgan Najafi, Saeid Soltanian, Habibollah Danyali, Rahman Hallaj, Abdollah Salimi, Seyed Mohammad Elahi, and Peyman Servati. Preparation of cobalt nanowires in porous aluminum oxide: Study of the effect of barrier layer. *Journal of Materials Research*, 27(18):2382–2390, 2012.

[90] Hongmei Dang, Vijay P Singh, Sai Guduru, and Jeffery T Hastings. Embedded nanowire window layers for enhanced quantum efficiency in window-absorber type solar cells like cds/cdte. *Solar Energy Materials and Solar Cells*, 144:641–651, 2016.

[91] P Apel. Track etching technique in membrane technology. *Radiation Measurements*, 34(1):559–566, 2001.

[92] KC Khulbe, T Matsuura, and C Feng. The art of making polymeric membranes. *Handbook of Polymers for Pharmaceutical Technologies: Processing and Applications, Volume 2*, pages 33–66, 2015.

[93] Etienne Ferain and Roger Legras. Track-etch templates designed for micro-and nanofabrication. *Nuclear Instruments and Methods in Physics Research Section B: Beam Interactions with Materials and Atoms*, 208:115–122, 2003.

[94] Niko Haberkorn, Maria C Lechmann, Byeong Hyeok Sohn, Kookheon Char, Jochen S Gutmann, and Patrick Theato. Templated organic and hybrid materials for optoelectronic applications. *Macromolecular rapid communications*, 30(14):1146–1166, 2009.

[95] Edward JW Crossland, Sabine Ludwigs, Marc A Hillmyer, and Ullrich Steiner. Freestanding nanowire arrays from soft-etch block copolymer templates. *Soft Matter*, 3(1):94–98, 2007.

[96] Kun-Hua Tu, Wubin Bai, George Liontos, Konstantinos Ntetsikas, Apostolos Avgeropoulos, and Caroline A Ross. Universal pattern transfer methods for metal nanostructures by block copolymer lithography. *Nanotechnology*, 26(37):375301, 2015.

[97] Pin Ho, Kun-Hua Tu, Jinshuo Zhang, Congli Sun, Jingsheng Chen, George Liontos, Konstantinos Ntetsikas, Apostolos Avgeropoulos, Paul M Voyles, and Caroline A Ross. Domain configurations in co/pd and l1 0-fept nanowire arrays with perpendicular magnetic anisotropy. *Nanoscale*, 8(9):5358–5367, 2016.

[98] Hyungju Ahn, Sungmin Park, Sang-Woo Kim, Pil J Yoo, Du Yeol Ryu, and Thomas P Russell. Nanoporous block copolymer membranes for ultrafiltration: a simple approach to size tunability. *ACS nano*, 8(11):11745–11752, 2014.

[99] Allen Noshay and James E McGrath. *Block copolymers: overview and critical survey*. Elsevier, 2013.

[100] Adam Kosiorek, Witold Kandulski, Piotr Chudzinski, Krzysztof Kempa, and Michael Giersig. Shadow nanosphere lithography: simulation and experiment. *Nano Letters*, 4(7):1359–1363, 2004.

[101] Xuefeng Liu, Numan Gozubenli, Baeck Choi, Peng Jiang, Timothy Meagher, and Bin Jiang. Templated fabrication of periodic arrays of metallic and silicon nanorings with complex nanostructures. *Nanotechnology*, 26(5):055603, 2015.

[102] Peng Jiang and Michael J McFarland. Wafer-scale periodic nanohole arrays templated from two-dimensional nonclose-packed colloidal crystals. *Journal of the American Chemical Society*, 127(11):3710–3711, 2005.

[103] Peng Jiang, Tushar Prasad, Michael J McFarland, and Vicki L Colvin. Two-dimensional nonclose-packed colloidal crystals formed by spincoating. *Applied Physics Letters*, 89(1):011908, 2006.

[104] Bo Wu, Than Zaw Oo, Xianglin Li, Xinfeng Liu, Xiangyang Wu, Edwin Kok Lee Yeow, Hong Jin Fan, Nripan Mathews, and Tze Chien Sum. Efficiency enhancement in bulk-heterojunction solar cells integrated with large-area ag nanotriangle arrays. *The Journal of Physical Chemistry C*, 116(28):14820–14825, 2012.

[105] LN Deepak Kallepalli, C Constantinescu, P Delaporte, O Utéza, and D Grojo. Ultra-high ordered, centimeter scale preparation of microsphere langmuir films. *Journal of colloid and interface science*, 446:237–243, 2015.

[106] Abhinav Malasi, Jingxuan Ge, Connor Carr, Hernando Garcia, Gerd Duscher, and Ramki Kalyanaraman. Two-dimensionally ordered plasmonic and magnetic nanostructures on transferable electron-transparent substrates. *Particle & Particle Systems Characterization*, 32(10):970–978, 2015.

[107] Peng Jiang and Michael J McFarland. Large-scale fabrication of wafer-size colloidal crystals, macroporous polymers and nanocomposites by spin-coating. *Journal of the American Chemical Society*, 126(42):13778–13786, 2004.

[108] Pingqi Gao, Jian He, Suqiong Zhou, Xi Yang, Sizhong Li, Jiang Sheng, Dan Wang, Tianbao Yu, Jichun Ye, and Yi Cui. Large-area nanosphere self-assembly by a micro-propulsive injection method for high throughput periodic surface nanotexturing. *Nano letters*, 15(7):4591–4598, 2015.

[109] G.Z. Cao. *Nanostructures&nanomaterials*. Imperial College London, 2004.

[110] A. P. Li, F. Müller, A. Birner, K. Nielsch, and U. Gösele. Hexagonal pore arrays with a 50–420 nm interpore distance formed by self-organization in anodic alumina. *Journal of Applied Physics*, 84(11):6023–6026, 1998.

[111] O. Jessensky, F. Müller, and U. Gösele. Self-organized formation of hexagonal pore arrays in anodic alumina. *Applied Physics Letters*, 72(10):1173–1175, 1998.

[112] Carmen Mijangos, Rebeca Hernandez, and Jaime Martin. A review on the progress of polymer nanostructures with modulated morphologies and properties, using nanoporous aao templates. *Progress in Polymer Science*, 54:148–182, 2016.

[113] M Kylan McQuaig Jr, Alejandro Toro, William Van Geertruyden, and Wojciech Z Misiolek. The effect of high temperature heat treatment on the structure and properties of anodic aluminum oxide. *Journal of Materials Science*, 46(1):243–253, 2011.

[114] Woo Lee, Ran Ji, Ulrich Gösele, and Kornelius Nielsch. Fast fabrication of long-range ordered porous alumina membranes by hard anodization. *Nature materials*, 5(9):741–747, 2006.

[115] MJ Kao, SF Chang, CC Chen, and CG Kuo. The surface adsorption of nano-pore template. *World Academy of Science, Engineering and Technology, International Journal of Chemical, Molecular, Nuclear, Materials and Metallurgical Engineering*, 6(5):441–444, 2012.

[116] Guowen Meng, Yung Joon Jung, Anyuan Cao, Robert Vajtai, and Pulickel M Ajayan. Controlled fabrication of hierarchically branched nanopores, nanotubes, and nanowires. *Proceedings of the National Academy of Sciences of the United States of America*, 102(20):7074–7078, 2005.

[117] Hanju Jo, Niko Haberkorn, Jia-Ahn Pan, Mohammad Vakili, Kornelius Nielsch, and Patrick Theato. Fabrication of chemically tunable, hierarchically branched polymeric nanostructures by multi-branched aao templates. *Langmuir*, 2016.

[118] Kaiying Wang, Guohua Liu, Nils Hoivik, Erik Johannessen, and Henrik Jakobsen. Electrochemical engineering of hollow nanoarchitectures: pulse/step anodization (si, al, ti) and their applications. *Chemical Society Reviews*, 43(5):1476–1500, 2014.

[119] Jaime Martin, Marisol Martin Gonzalez, Jose Francisco Fernandez, and Olga Caballero Calero. Ordered three-dimensional interconnected nanoarchitectures in anodic porous alumina. *Nature communications*, 5, 2014.

[120] Ye Wang, Yuting Chen, Tushar Kumeria, Fuyuan Ding, Andreas Evdokiou, Dusan Losic, and Abel Santos. Facile synthesis of optical microcavities by a rationally designed anodization approach: tailoring photonic signals by nanopore structure. *ACS applied materials & interfaces*, 7(18):9879–9888, 2015.

[121] CA Huber, TE Huber, M Sadoqi, JA Lubin, S Manalis, CB Prater, et al. Nanowire array composites. *Science-AAAS-Weekly Paper Edition-including Guide to Scientific Information*, 263(5148):800–801, 1994.

[122] Ahmed Hashoosh, Hassan Hirshy, EB Brousseau, and Ahmed Moosa. Fabrication of aluminium nanowires by differential pressure injection. *ISRN Nanomaterials*, 2013, 2013.

[123] Neil P Dasgupta, Jianwei Sun, Chong Liu, Sarah Brittman, Sean C Andrews, Jongwoo Lim, Hanwei Gao, Ruoxue Yan, and Peidong Yang. 25th anniversary article: semiconductor nanowires–synthesis, characterization, and applications. *Advanced Materials*, 26(14):2137–2184, 2014.

[124] Timothy E Bogart, Soham Dey, K-K Lew, Suzanne E Mohney, and Joan M Redwing. Diameter-controlled synthesis of silicon nanowires using nanoporous alumina membranes. *Advanced Materials*, 17(1):114–117, 2005.

[125] Vincent T Renard, Michael Jublot, Patrice Gergaud, Peter Cherns, Denis Rouchon, Amal Chabli, and Vincent Jousseaume. Catalyst preparation for cmos-compatible silicon nanowire synthesis. *Nature nanotechnology*, 4(10):654–657, 2009.

[126] Chang Hyun Bae, Seung Min Park, Sung Chan Park, and Jeong Sook Ha. Array of ultraviolet luminescent zno nanodots fabricated by pulsed laser deposition using an anodic aluminium oxide template. *Nanotechnology*, 17(2):381, 2005.

[127] Jaya Sarkar, GobindaGopal Khan, and A. Basumallick. Nanowires: properties, applications and synthesis via porous anodic aluminium oxide template. *Bulletin of Materials Science*, 30(3):271–290, 2007.

[128] Rui Liu, Ying Zhang, and Pingyun Feng. Multiresponsive supramolecular nanogated ensembles. *Journal of the American Chemical Society*, 131(42):15128–15129, 2009.

[129] Xuecheng Chen, Hongmin Chen, Carla Tripisciano, Anna Jedrzejewska, Mark H Rümmeli, Rüdiger Klingeler, Ryszard J Kalenczuk, Paul K Chu, and Ewa Borowiak-Palen. Carbon-nanotube-based stimuli-responsive controlled-release system. *Chemistry–A European Journal*, 17(16):4454–4459, 2011.

[130] Xiao-Dong Ma, Xue-Feng Qian, Jie Yin, and Zi-Kang Zhu. Preparation and characterization of polyvinyl alcohol–selenide nanocomposites at room temperature. *Journal of Materials Chemistry*, 12(3):663–666, 2002.

[131] Nobuyuki Takeyasu, Takuo Tanaka, and Satoshi Kawata. Metal deposition deep into microstructure by electroless plating. *Japanese journal of applied physics*, 44(8L):L1134, 2005.

[132] Alexey P. Leontiev, Oleg A. Brylev, and Kirill S. Napolskii. Arrays of rhodium nanowires based on anodic alumina: Preparation and electrocatalytic activity for nitrate reduction. *Electrochimica Acta*, 155:466–473, 2015.

[133] Yu-Song Cheng, Hao-Jan Lang, and Mau-Phon Houng. Fabrication of single phase p-cuinse2 nanowire arrays by electrodeposited into anodic alumina templates. *Applied Physics Letters*, 107(16):162103, 2015.

[134] Dmitri Routkevitch, Terry Bigioni, Martin Moskovits, and Jing Ming Xu. Electrochemical fabrication of cds nanowire arrays in porous anodic aluminum oxide templates. *The Journal of Physical Chemistry*, 100(33):14037–14047, 1996.

[135] Francesca L Boughey, Timothy Davies, Anuja Datta, Richard A Whiter, Suman-Lata Sahonta, and Sohini Kar-Narayan. Vertically aligned zinc oxide nanowires electrodeposited within porous polycarbonate templates for vibrational energy harvesting. *Nanotechnology*, 27(28):28LT02, 2016.

[136] Zhibo Zhang, Jackie Y Ying, and Mildred S Dresselhaus. Bismuth quantum-wire arrays fabricated by a vacuum melting and pressure injection process. *Journal of materials research*, 13(07):1745–1748, 1998.

[137] G. Riveros, H. Gómez, A. Cortes, R. E. Marotti, and E. A. Dalchiele. Crystallographically-oriented single-crystalline copper nanowire arrays electrochemically grown into nanoporous anodic alumina templates. *Applied Physics A*, 81(1):17–24, 2005.

[138] XY Zhang, LD Zhang, Y Lei, LX Zhao, and YQ Mao. Fabrication and characterization of highly ordered au nanowire arrays. *Journal of Materials Chemistry*, 11(6):1732–1734, 2001.

[139] A Kazadi Mukenga Bantu, J Rivas, G Zaragoza, MA Lopez-Quintela, and MC Blanco. Structure and magnetic properties of electrodeposited cobalt nanowires. *Journal of Applied Physics*, 89(6):3393–3397, 2001.

[140] Eunseong Ko, Jinsub Choi, Koichi Okamoto, Yongsug Tak, and Jaeyoung Lee. Cu2o nanowires in an alumina template: Electrochemical conditions for the synthesis and photoluminescence characteristics. *Chemphyschem*, 7(7):1505–1509, 2006. Times Cited: 24.

[141] Nathan J. Gerein and Joel A. Haber. Effect of ac electrodeposition conditions on the growth of high aspect ratio copper nanowires in porous aluminum oxide templates. *The Journal of Physical Chemistry B*, 109(37):17372–17385, 2005.

[142] Lifeng Liu, Woo Lee, Z Huang, R Scholz, and Ulrich Gösele. Fabrication and characterization of a flow-through nanoporous gold nanowire/aao composite membrane. *Nanotechnology*, 19(33):335604, 2008.

[143] A Santos, L Vojkuvka, J Pallares, J Ferre Borrull, and LF Marsal. Cobalt and nickel nanopillars on aluminium substrates by direct current electrodeposition process. *Nanoscale research letters*, 4(9):1021, 2009.

[144] Piao Liu, Vijay P Singh, Suresh Rajaputra, Sovannary Phok, and Zhi Chen. Characteristics of copper indium diselenide nanowires embedded in porous alumina templates. *Journal of Materials Research*, 25(02):207–212, 2010.

[145] Injeti Gurrappa and Leo Binder. Electrodeposition of nanostructured coatings and their characterization—a review. *Science and Technology of Advanced Materials*, 2016.

[146] M. Rycenga, C. M. Cobley, J. Zeng, W. Y. Li, C. H. Moran, Q. Zhang, D. Qin, and Y. N. Xia. Controlling the synthesis and assembly of silver nanostructures for plasmonic applications. *Chemical Reviews*, 111(6):3669–3712, 2011.

[147] Mordechay Schlesinger. *Electroless and Electrodeposition of Silver*, pages 131–138. John Wiley & Sons, Inc., 2010.

[148] Peter P Mardilovich, Alexander N Govyadinoy, Nadezhda I Mazurenko, and Russell Paterson. New and modified anodic alumina membranes part ii. comparison of solubility of amorphous (normal) and polycrystalline anodic alumina membranes. *Journal of membrane science*, 98(1):143–155, 1995.

[149] G. Riveros, S. Green, A. Cortes, H. Gomez, R. E. Marotti, and E. A. Dalchiele. Silver nanowire arrays electrochemically grown into nanoporous anodic alumina templates. *Nanotechnology*, 17(2):561–570, 2006.

[150] Che-Ning Yeh, Kalyan Raidongia, Jiaojing Shao, Quan-Hong Yang, and Jiaxing Huang. On the origin of the stability of graphene oxide membranes in water. *Nature Chemistry*, 7(2):166–170, 2015.

[151] Y. T. Pang, G. W. Meng, Q. Fang, and L. D. Zhang. Silver nanowire array infrared polarizers. *Nanotechnology*, 14(1):20, 2003.

[152] Zhang-Kai Zhou, Min Li, Zhong-Jian Yang, Xiao-Niu Peng, Xiong-Rui Su, Zong-Suo Zhang, Jian-Bo Li, Nam-Chol Kim, Xue-Feng Yu, and Li Zhou. Plasmon-mediated radiative energy transfer across a silver nanowire array via resonant transmission and subwavelength imaging. *ACS nano*, 4(9):5003–5010, 2010.

[153] R. L. Zong, J. Zhou, Q. Li, B. Du, B. Li, M. Fu, X. W. Qi, L. T. Li, and S. Buddhudu. Synthesis and optical properties of silver nanowire arrays embedded in anodic alumina membrane. *Journal of Physical Chemistry B*, 108(43):16713–16716, 2004. ISI Document Delivery No.: 865EP Times Cited: 105 Cited Reference Count: 34 Zong, RL Zhou, J Li, Q Du, B Li, B Fu, M Qi, XW Li, LT Buddhudu, S Amer chemical soc Washington.

[154] Jinsub Choi, Guido Sauer, Kornelius Nielsch, Ralf B. Wehrspohn, and Ulrich Gösele. Hexagonally arranged monodisperse silver nanowires with adjustable diameter and high aspect ratio. *Chemistry of Materials*, 15(3):776–779, 2003.

[155] G Kartopu, KL Choy, and O Yalçın. Perpendicular silver nanowire arrays on an ito/glass substrate for plasmonic applications. *Physica Scripta*, 89(9):095801, 2014.

[156] J. Yao, Y. Wang, K. T. Tsai, Z. W. Liu, X. B. Yin, G. Bartal, A. M. Stacy, Y. L. Wang, and X. Zhang. Design, fabrication and characterization of indefinite metamaterials of nanowires. *Philosophical Transactions of the Royal Society a-Mathematical Physical and Engineering Sciences*, 369(1950):3434–3446, 2011.

[157] X. Y. Sun, F. Q. Xu, Z. M. Li, and W. H. Zhang. Cyclic voltammetry for the fabrication of high dense silver nanowire arrays with the assistance of aao template. *Materials Chemistry and Physics*, 90(1):69–72, 2005. 886UF Times Cited:42 Cited References Count:23.

[158] G. Sauer, G. Brehm, S. Schneider, K. Nielsch, R. B. Wehrspohn, J. Choi, H. Hofmeister, and U. Gösele. Highly ordered monocrystalline silver nanowire arrays. *Journal of Applied Physics*, 91(5):3243–3247, 2002.

[159] F. Keller, M. S. Hunter, and D. L. Robinson. Structural features of oxide coatings on aluminium. *Journal of the Electrochemical Society*, 100(9):411–419, 1953.

[160] Justin J. Hill, Kelly Haller, and Kirk J. Ziegler. Direct fabrication of high-aspect ratio anodic aluminum oxide with continuous pores on conductive glass. *Journal of The Electrochemical Society*, 158(1):E1–E7, 2011.

[161] S. Z. Chu, K. Wada, S. Inoue, S. Todoroki, Y. K. Takahashi, and K. Hono. Fabrication and characteristics of ordered ni nanostructures on glass by anodization and direct current electrodeposition. *Chemistry of Materials*, 14(11):4595–4602, 2002.

[162] Song Zhu Chu, K Wada, S Inoue, and S Todoroki. Formation and microstructures of anodic alumina films from aluminum sputtered on glass substrate. *Journal of the Electrochemical Society*, 149(7):B321–B327, 2002.

[163] Kevin P. Musselman, Gregory J. Mulholland, Adam P. Robinson, Lukas Schmidt-Mende, and Judith L. MacManus-Driscoll. Low-temperature synthesis of large-area, free-standing nanorod arrays on ito/glass and other conducting substrates. *Advanced Materials*, 20(23):4470–4475, 2008.

[164] Thelese R. B. Foong, Alan Sellinger, and Xiao Hu. Origin of the bottlenecks in preparing anodized aluminum oxide (aao) templates on ito glass. *ACS Nano*, 2(11):2250–2256, 2008.

[165] Thelese R. B. Foong, Yen Nan Liang, and Xiao Hu. Anodic aluminum oxide (aao) templates on transparent conducting glass (tco) coated glass: New prospects for a

mature nano-fabrication tool. *Nanoscience and Nanotechnology Letters*, 4(5):494–504, 2012.

[166] J.A Bard and L.R. Faulkner. *Electrochemical Methods: Fundamentals and Applications*. John Wiley & Sons, Inc., 2001.

[167] M. Fuchigami, T.and Atobe and S. Inagi. *Fundamentals and Applications of Organic Electrochemistry Synthesis, Materials, Devices*. Wiley, 2014.

[168] Lionel Vayssieres. *On Solar Hydrogen & Nanotechnology*. Wiley, 2010.

[169] Li Li Zhang and XS Zhao. Carbon-based materials as supercapacitor electrodes. *Chemical Society Reviews*, 38(9):2520–2531, 2009.

[170] Injeti Gurrappa and Leo Binder. Electrodeposition of nanostructured coatings and their characterization—a review. *Science and Technology of Advanced Materials*, 9(4):043001, 2008.

[171] Shuai Chen, Sapanbir S. Thind, and Aicheng Chen. Nanostructured materials for water splitting - state of the art and future needs: A mini-review. *Electrochemistry Communications*, 63:10 – 17, 2016.

[172] Peter Wilkinson. Understanding gold plating. *Gold Bulletin*, 19(3):75–81, 1986.

[173] M. J. Liew, S. Roy, and K. Scott. Development of a non-toxic electrolyte for soft gold electrodeposition: an overview of work at university of newcastle upon tyne. *Green Chemistry*, 5(4):376–381, 2003.

[174] Andreas Kolloch, Tobias Geldhauser, Kosei Ueno, Hiroaki Misawa, Johannes Boneberg, Anton Plech, and Paul Leiderer. Femtosecond and picosecond near-field ablation of gold nanotriangles: nanostructuring and nanomelting. *Applied Physics A*, 104(3):793–799, 2011.

[175] Xiaomu Wu, Peter L Redmond, Haitao Liu, Yihui Chen, Michael Steigerwald, and Louis Brus. Photovoltage mechanism for room light conversion of citrate stabilized silver nanocrystal seeds to large nanoprisms. *Journal of the American Chemical Society*, 130(29):9500–9506, 2008.

[176] Cynthia G. Zoski. *Handbook of Electrochemistry*. Elsevier B.V., 2007.

[177] A. Tuteja. *Fundamentals of Physical Chemistry*. Discovery Pubilishing House, 2007.

[178] K Ebihara, H Takahashi, and M Nagayama. Structure and density of anodic oxide films formed on aluminium in oxalic acid solutions. *Journal of the Metal Finishing Society of Japan*, 34(11):548–553, 1983.

[179] Leszek Zaraska, Grzegorz D. Sulka, Janusz Szeremeta, and Marian Jaskuła. Porous anodic alumina formed by anodization of aluminum alloy (aa1050) and high purity aluminum. *Electrochimica Acta*, 55(14):4377–4386, 2010.

[180] Sachiko Ono, Makiko Saito, and Hidetaka Asoh. Self-ordering of anodic porous alumina formed in organic acid electrolytes. *Electrochimica Acta*, 51(5):827–833, 2005.

[181] Hsien-Ping Feng, Trilochan Paudel, Bo Yu, Shuo Chen, Zhi Feng Ren, and Gang Chen. Nanoparticle-enabled selective electrodeposition. *Advanced Materials*, 23(21):2454–2459, 2011.

[182] K. Nielsch, F. Müller, A. P. Li, and U. Gösele. Uniform nickel deposition into ordered alumina pores by pulsed electrodeposition. *Advanced Materials*, 12(8):582–586, 2000.

[183] Paul R. Evans, René Kullock, William R. Hendren, Ron Atkinson, Robert J. Pollard, and Lukas M. Eng. Optical transmission properties and electric field distribution of interacting 2d silver nanorod arrays. *Advanced Functional Materials*, 18(7):1075–1079, 2008.

[184] Chad E Taylor, Jeanne E Pemberton, Gary G Goodman, and Mark H Schoenfisch. Surface enhancement factors for ag and au surfaces relative to pt surfaces for monolayers of thiophenol. *Applied spectroscopy*, 53(10):1212–1221, 1999.

[185] Seung Joon Lee, Andrew R. Morrill, and Martin Moskovits. Hot spots in silver nanowire bundles for surface-enhanced raman spectroscopy. *Journal of the American Chemical Society*, 128(7):2200–2201, 2006.

[186] Geun Hoi Gu, Jurae Kim, Lily Kim, and Jung Sang Suh. Optimum length of silver nanorods for fabrication of hot spots. *The Journal of Physical Chemistry C*, 111(22):7906–7909, 2007.

[187] Neval A Cinel, Serkan Buetuen, Guelay Ertas, and Ekmel Oezbay. Fairy chimney -shaped tandem metamaterials as double resonance sers substrates. *small*, 9(4):531–537, 2013.

[188] Lucas A Lane, Ximei Qian, and Shuming Nie. Sers nanoparticles in medicine: from label-free detection to spectroscopic tagging. *Chemical reviews*, 115(19):10489–10529, 2015.

[189] Zhulin Huang, Guowen Meng, Qing Huang, Bin Chen, Chuhong Zhu, and Zhuo Zhang. Large-area ag nanorod array substrates for sers: Aao template-assisted fabrication, functionalization, and application in detection pcbs. *Journal of Raman Spectroscopy*, 44(2):240–246, 2013.

[190] Zhendong Yan, Wei Du, Linlin Tu, Ping Gu, Zhong Huang, Peng Zhan, Fanxin Liu, and Zhenlin Wang. A facile high-performance sers substrate based on broadband near-perfect optical absorption. *Journal of Raman Spectroscopy*, 46(9):795–801, 2015.

[191] Katherine N Kanipe, Philip PF Chidester, Galen D Stucky, and Martin Moskovits. Large format surface-enhanced raman spectroscopy substrate optimized for enhancement and uniformity. *ACS nano*, 10(8):7566–7571, 2016.

[192] Qiuming Yu, Phillip Guan, Dong Qin, Greg Golden, and Paul M Wallace. Inverted size-dependence of surface-enhanced raman scattering on gold nanohole and nanodisk arrays. *Nano letters*, 8(7):1923–1928, 2008.

[193] Minhee Kang, Jae-Jun Kim, Young-Jae Oh, Sang-Gil Park, and Ki-Hun Jeong. A deformable nanoplasmonic membrane reveals universal correlations between plasmon resonance and surface enhanced raman scattering. *Advanced Materials*, 26(26):4510–4514, 2014.

[194] Nicolas Pazos-Perez, Claudia Simone Wagner, Jose M Romo-Herrera, Luis M Liz-Marzan, F Javier Garcia de Abajo, Alexander Wittemann, Andreas Fery, and Ramon A Alvarez-Puebla. Organized plasmonic clusters with high coordination number and extraordinary enhancement in surface-enhanced raman scattering (sers). *Angewandte Chemie International Edition*, 51(51):12688–12693, 2012.

[195] Bhavya Sharma, Renee R Frontiera, Anne-Isabelle Henry, Emilie Ringe, and Richard P Van Duyne. Sers: materials, applications, and the future. *Materials today*, 15(1):16–25, 2012.

[196] Zhiqiang Liang, Qifeng Zhang, Orawan Wiranwetchayan, Junting Xi, Zhou Yang, Kwangsuk Park, Chundong Li, and Guozhong Cao. Effects of the morphology of a zno buffer layer on the photovoltaic performance of inverted polymer solar cells. 22(10):2194–2201, 2012.

[197] Jin Young Kim, Sun Hee Kim, H-H Lee, Kwanghee Lee, Wanli Ma, Xiong Gong, and Alan J Heeger. New architecture for high-efficiency polymer photovoltaic cells using solution-based titanium oxide as an optical spacer. *Advanced materials*, 18(5):572–576, 2006.

[198] Jan Gilot, Ionuţ Barbu, Martijn M Wienk, and René AJ Janssen. The use of ZnO as optical spacer in polymer solar cells: theoretical and experimental study. *Applied Physics Letters*, 91(11):113520, 2007.

[199] Aung Ko Ko Kyaw, Dong Hwan Wang, David Wynands, Jie Zhang, Thuc-Quyen Nguyen, Guillermo C Bazan, and Alan J Heeger. Improved light harvesting and improved efficiency by insertion of an optical spacer ZnO in solution-processed small-molecule solar cells. *Nano letters*, 13(8):3796–3801, 2013.

[200] Harald Hoppe and Niyazi Serdar Sariciftci. Morphology of polymer/fullerene bulk heterojunction solar cells. *Journal of Materials Chemistry*, 16(1):45–61, 2006.

[201] Franz Padinger, Roman S Rittberger, and Niyazi S Sariciftci. Effects of postproduction treatment on plastic solar cells. *Advanced Functional Materials*, 13(1):85–88, 2003.

[202] Youngkyoo Kim, Stelios A Choulis, Jenny Nelson, Donal DC Bradley, Steffan Cook, and James R Durrant. Device annealing effect in organic solar cells with blends of regioregular poly (3-hexylthiophene) and soluble fullerene. *Applied Physics Letters*, 86(6), 2005.

[203] Lilian Chang, Hans WA Lademann, Jörg-Bernd Bonekamp, Klaus Meerholz, and Adam J Moulé. Effect of trace solvent on the morphology of P3HT: PCBM bulk heterojunction solar cells. *Advanced Functional Materials*, 21(10):1779–1787, 2011.

[204] Minh Trung Dang, Lionel Hirsch, and Guillaume Wantz. P3HT: PCBM, best seller in polymer photovoltaic research. *Advanced Materials*, 23(31):3597–3602, 2011.

[205] Nils-Krister Persson, Hans Arwin, and Olle Inganas. Optical optimization of polyfluorene-fullerene blend photodiodes. *Journal of Applied Physics*, 97(3):034503, 2005.

[206] Adam J Moulé, Jörg B Bonekamp, and Klaus Meerholz. The effect of active layer thickness and composition on the performance of bulk-heterojunction solar cells. *Journal of Applied Physics*, 100(9):094503, 2006.

[207] Jan D Kotlarski, Paul WM Blom, Lambert JA Koster, Martijn Lenes, and Lenneke H Slooff. Combined optical and electrical modeling of polymer: fullerene bulk heterojunction solar cells. *Journal of Applied Physics*, 103(8):084502, 2008.

[208] H Hoppe, N Arnold, NS Sariciftci, and D Meissner. Modeling the optical absorption within conjugated polymer/fullerene-based bulk-heterojunction organic solar cells. *Solar Energy Materials and Solar Cells*, 80(1):105–113, 2003.

[209] Douglas W Sievers, Vishal Shrotriya, and Yang Yang. Modeling optical effects and thickness dependent current in polymer bulk-heterojunction solar cells. *Journal of Applied Physics*, 100(11):114509, 2006.

[210] Areum Kim, Yulim Won, Kyoohee Woo, Chul-Hong Kim, and Jooho Moon. Highly transparent low resistance zno/ag nanowire/zno composite electrode for thin film solar cells. *ACS nano*, 7(2):1081–1091, 2013.

[211] Rupesh S Devan, Yuan-Ron Ma, Ranjit A Patil, and Schmidt-Mende Lukas. Highly stable supercapacitive performance of one-dimensional (1d) brookite tio 2 nanoneedles. *RSC Advances*, 6(67):62218–62225, 2016.

[212] Feng Gu, Lili Gai, Wei Shao, Chunzhong Li, and Lukas Schmidt-Mende. Heteroepitaxial growth of zno branches selectively on tio 2 nanorod tips with improved light harvesting performance. *Chemical communications*, 47(29):8400–8402, 2011.

[213] Xiaobo Chen and Samuel S Mao. Titanium dioxide nanomaterials: synthesis, properties, modifications, and applications. *Chem. Rev*, 107(7):2891–2959, 2007.

[214] Lukas Schmidt-Mende and Michael Grätzel. Tio 2 pore-filling and its effect on the efficiency of solid-state dye-sensitized solar cells. *Thin Solid Films*, 500(1):296–301, 2006.

[215] Jessica E Kroeze, Narukuni Hirata, Lukas Schmidt-Mende, Charles Orizu, Simon D Ogier, Kathryn Carr, Michael Grätzel, and James R Durrant. Parameters influencing charge separation in solid-state dye-sensitized solar cells using novel hole conductors. *Advanced Functional Materials*, 16(14):1832–1838, 2006.

[216] Henry J Snaith and Lukas Schmidt-Mende. Advances in liquid-electrolyte and solid-state dye-sensitized solar cells. *Advanced Materials*, 19(20):3187–3200, 2007.

[217] Kirill Zilberberg, Sara Trost, Jens Meyer, Antoine Kahn, Andreas Behrendt, Dirk Lützenkirchen-Hecht, Ronald Frahm, and Thomas Riedl. Inverted organic solar cells with sol–gel processed high work-function vanadium oxide hole-extraction layers. *Advanced Functional Materials*, 21(24):4776–4783, 2011.

[218] Kirill Zilberberg, Sara Trost, Hans Schmidt, and Thomas Riedl. Solution processed vanadium pentoxide as charge extraction layer for organic solar cells. *Advanced Energy Materials*, 1(3):377–381, 2011.

[219] İsmail Karakurt, Johannes Boneberg, and Paul Leiderer. Electrochromic switching of wo3 nanostructures and thin films. *Applied Physics A*, 83(1):1–3, 2006.

[220] Kirill Zilberberg, Houssem Gharbi, Andreas Behrendt, Sara Trost, and Thomas Riedl. Low-temperature, solution-processed moo x for efficient and stable organic solar cells. *ACS applied materials & interfaces*, 4(3):1164–1168, 2012.

[221] Y Hirose, A Kahn, V Aristov, P Soukiassian, V Bulovic, and SR Forrest. Chemistry and electronic properties of metal-organic semiconductor interfaces: Al, ti, in, sn, ag, and au on ptcda. *Physical Review B*, 54(19):13748, 1996.

[222] SC Veenstra and HT Jonkman. Energy-level alignment at metal–organic and organic–organic interfaces. *Journal of Polymer Science Part B: Polymer Physics*, 41(21):2549–2560, 2003.

[223] N Koch, A Kahn, J Ghijsen, J-Jj Pireaux, J Schwartz, RL Johnson, and A Elschner. Conjugated organic molecules on metal versus polymer electrodes: Demonstration of a key energy level alignment mechanism. *Applied Physics Letters*, 82(1):70–72, 2003.

[224] Seo-Jin Ko, Bright Walker, Thanh Luan Nguyen, Hyosung Choi, Jason Seifter, Mohammad Afsar Uddin, Taehyo Kim, Seongbeom Kim, Jungwoo Heo, Gi-Hwan Kim, et al. Photocurrent extraction efficiency near unity in a thick polymer bulk heterojunction. *Advanced Functional Materials*, 26(19):3324–3330, 2016.

[225] Dani M Stoltzfus, Jenny E Donaghey, Ardalan Armin, Paul E Shaw, Paul L Burn, and Paul Meredith. Charge generation pathways in organic solar cells: Assessing the contribution from the electron acceptor. *Chemical Reviews*, 2016.

[226] George F Burkhard, Eric T Hoke, and Michael D McGehee. Accounting for interference, scattering, and electrode absorption to make accurate internal quantum efficiency measurements in organic and other thin solar cells. *Advanced Materials*, 22(30):3293–3297, 2010.

[227] Nafiseh Sharifi, Shabnam Dadgostar, Nima Taghavinia, et al. Freestanding light scattering hollow silver spheres prepared by a facile sacrificial templating method and their application in dye-sensitized solar cells. *Journal of Power Sources*, 225:46–50, 2013.

[228] Armando Giannattasio, Ian R Hooper, and William L Barnes. Transmission of light through thin silver films via surface plasmon-polaritons. *Optics express*, 12(24):5881–5886, 2004.

[229] Hiram W Edwards and Robert P Petersen. Reflectivity of evaporated silver films. *Physical Review*, 50(9):871, 1936.

[230] Thomas Pfadler, Martin Stärk, Eugen Zimmermann, Martin Putnik, Johannes Boneberg, Jonas Weickert, and Lukas Schmidt-Mende. A comparison of light-coupling into high and low index nanostructured photovoltaic thin films. *APL materials*, 3(6):066101, 2015.

[231] W Dickson, GA Wurtz, P Evans, D O'Connor, R Atkinson, R Pollard, and AV Zayats. Dielectric-loaded plasmonic nanoantenna arrays: A metamaterial with tuneable optical properties. *Physical Review B*, 76(11):115411, 2007.

[232] Thomas Pfadler, Thomas Kiel, Martin Stärk, Julia FM Werra, Christian Matyssek, Daniel Sommer, Johannes Boneberg, Kurt Busch, Jonas Weickert, and Lukas Schmidt-Mende. Structure-induced resonant tail-state regime absorption in polymer: fullerene bulk-heterojunction solar cells. *Physical Review B*, 93(20):205305, 2016.

[233] Jason B Baxter and Eray S Aydil. Nanowire-based dye-sensitized solar cells. *Applied Physics Letters*, 86(5):053114, 2005.

[234] Isabella Concina and Alberto Vomiero. Metal oxide semiconductors for dye-and quantum-dot-sensitized solar cells. *Small*, 11(15):1744–1774, 2015.

[235] Jens Czolk, Dominik Landerer, Manuel Koppitz, David Nass, and Alexander Colsmann. Highly efficient, mechanically flexible, semi-transparent organic solar cells doctor bladed from non-halogenated solvents. *Advanced Materials Technologies*, 2016.

[236] T Miyazaki, A Akisawa, and T Kashiwagi. Energy savings of office buildings by the use of semi-transparent solar cells for windows. *Renewable energy*, 30(3):281–304, 2005.

[237] Ricky B Dunbar, Thomas Pfadler, and Lukas Schmidt-Mende. Highly absorbing solar cells—a survey of plasmonic nanostructures. *Optics express*, 20(102):A177–A189, 2012.

[238] Sylvio Schubert, Jan Meiss, Lars Müller-Meskamp, and Karl Leo. Improvement of transparent metal top electrodes for organic solar cells by introducing a high surface energy seed layer. *Advanced Energy Materials*, 3(4):438–443, 2013.

[239] Sylvio Schubert, Lars Müller-Meskamp, and Karl Leo. Unusually high optical transmission in ca:ag blend films: High-performance top electrodes for efficient organic solar cells. *Advanced Functional Materials*, 24(42):6668–6676, 2014.

[240] S.Schubert. *Transparent top electrodes for organic solar cells*. PhD thesis, 2014.

[241] M Farangi, M Zahedifar, MR Mozdianfard, and MH Pakzamir. Effects of silicon nanowires length on solar cells photovoltaic properties. *Applied Physics A*, 109(2):299–306, 2012.

[242] Naveen Kumar Elumalai and Ashraf Uddin. Open circuit voltage of organic solar cells: an in-depth review. *Energy & Environmental Science*, 9(2):391–410, 2016.

[243] Antonio Guerrero, Teresa Ripolles-Sanchis, Pablo P Boix, and Germà Garcia-Belmonte. Series resistance in organic bulk-heterojunction solar devices: Modulating carrier transport with fullerene electron traps. *Organic Electronics*, 13(11):2326–2332, 2012.

[244] RA Street, KW Song, and S Cowan. Influence of series resistance on the photocurrent analysis of organic solar cells. *Organic Electronics*, 12(2):244–248, 2011.

[245] Boyuan Qi and Jizheng Wang. Fill factor in organic solar cells. *Physical Chemistry Chemical Physics*, 15(23):8972–8982, 2013.

[246] Sarah Maria Falke, Carlo Andrea Rozzi, Daniele Brida, Margherita Maiuri, Michele Amato, Ephraim Sommer, Antonietta De Sio, Angel Rubio, Giulio Cerullo, Elisa Molinari, et al. Coherent ultrafast charge transfer in an organic photovoltaic blend. *Science*, 344(6187):1001–1005, 2014.

[247] H Nishino, G Yu, AJ Heeger, T-A Chen, and RD Rieke. Electroluminescence from blend films of poly (3-hexylthiophene) and poly (n-vinylcarbazole). *Synthetic metals*, 68(3):243–247, 1995.

[248] Tian-An Chen, Xiaoming Wu, and Reuben D Rieke. Regiocontrolled synthesis of poly (3-alkylthiophenes) mediated by rieke zinc: their characterization and solid-state properties. *Journal of the American Chemical Society*, 117(1):233–244, 1995.

[249] Kwang-Dae Kim, Thomas Pfadler, Eugen Zimmermann, Yuyi Feng, James A Dorman, Jonas Weickert, and Lukas Schmidt-Mende. Decoupling optical and electronic optimization of organic solar cells using high-performance temperature-stable tio2/ag/tio2 electrodes. *APL Materials*, 3(10):106105, 2015.

[250] Lichang Zeng, Ching W Tang, and Shaw H Chen. Effects of active layer thickness and thermal annealing on polythiophene: Fullerene bulk heterojunction photovoltaic devices. *Applied Physics Letters*, 97(5):053305, 2010.

[251] Gang Li, Vishal Shrotriya, Jinsong Huang, Yan Yao, Tom Moriarty, Keith Emery, and Yang Yang. High-efficiency solution processable polymer photovoltaic cells by self-organization of polymer blends. *Nat Mater*, 4(11):864–868, 2005.

[252] S. R. Cowan, A. Roy, and A. J. Heeger. Recombination in polymer-fullerene bulk heterojunction solar cells. *Physical Review B*, 82(24), 2010.

[253] R. A. Street, Sarah Cowan, and A. J. Heeger. Experimental test for geminate recombination applied to organic solar cells. *Physical Review B*, 82(12):121301, 2010.

[254] Uli Würfel, Dieter Neher, Annika Spies, and Steve Albrecht. Impact of charge transport on current-voltage characteristics and power-conversion efficiency of organic solar cells. *Nature communications*, 6, 2015.

[255] VD Mihailetchi, LJA Koster, JC Hummelen, and PWM Blom. Photocurrent generation in polymer-fullerene bulk heterojunctions. *Physical review letters*, 93(21):216601, 2004.

[256] Valentin D Mihailetchi, HX Xie, Bert de Boer, LJ Anton Koster, and Paul WM Blom. Charge transport and photocurrent generation in poly (3-hexylthiophene): methanofullerene bulk-heterojunction solar cells. *Advanced Functional Materials*, 16(5):699–708, 2006.

[257] VD Mihailetchi, J Wildeman, and PWM Blom. Space-charge limited photocurrent. *Physical review letters*, 94(12):126602, 2005.

[258] M Lenes, LJA Koster, VD Mihailetchi, and PWM Blom. Thickness dependence of the efficiency of polymer: fullerene bulk heterojunction solar cells. *Applied physics letters*, 88(24):243502–243502, 2006.

[259] Daisuke Mori, Hiroaki Benten, Izumi Okada, Hideo Ohkita, and Shinzaburo Ito. Highly efficient charge-carrier generation and collection in polymer/polymer blend solar cells with a power conversion efficiency of 5.7%. *Energy & Environmental Science*, 7(9):2939–2943, 2014.

[260] Alvin M Goodman and Albert Rose. Double extraction of uniformly generated electron-hole pairs from insulators with noninjecting contacts. *Journal of Applied Physics*, 42(7):2823–2830, 1971.

[261] Albert Rose. *Concepts in photoconductivity and allied problems*. Number 19. Interscience publishers, 1963.

[262] L Jan Anton Koster, Wouter J van Strien, Waldo JE Beek, and Paul WM Blom. Device operation of conjugated polymer/zinc oxide bulk heterojunction solar cells. *Advanced Functional Materials*, 17(8):1297–1302, 2007.

[263] Christopher R McNeill, Jonathan JM Halls, Richard Wilson, Gregory L Whiting, Stephen Berkebile, Michael G Ramsey, Richard H Friend, and Neil C Greenham. Efficient polythiophene/polyfluorene copolymer bulk heterojunction photovoltaic devices: device physics and annealing effects. *Advanced Functional Materials*, 18(16):2309–2321, 2008.

[264] L Jan A Koster, Valentin D Mihailetchi, R Ramaker, and Paul WM Blom. Light intensity dependence of open-circuit voltage of polymer: fullerene solar cells. *Applied Physics Letters*, 86(12):123509–123509, 2005.

[265] M Magdalena Mandoc, Welmoed Veurman, L Jan Anton Koster, Bert de Boer, and Paul WM Blom. Origin of the reduced fill factor and photocurrent in mdmo-ppv: Pcnepv all-polymer solar cells. *Advanced Functional Materials*, 17(13):2167–2173, 2007.

[266] Claire L Armstrong, Michael B Price, David Muoz Rojas, Nathaniel JKL Davis, Mojtaba Abdi Jalebi, Richard H Friend, Neil C Greenham, Judith L MacManus Driscoll, Marcus L Boehm, and Kevin P Musselman. Influence of an inorganic interlayer on exciton separation in hybrid solar cells. *ACS nano*, 9(12):11863–11871, 2015.

[267] S Solak, PWM Blom, and GAH Wetzelaer. Effect of non-ohmic contacts on the light-intensity dependence of the open-circuit voltage in organic solar cells. *Applied Physics Letters*, 109(5):053302, 2016.

[268] Thomas Kirchartz, Florent Deledalle, Pabitra Shakya Tuladhar, James R Durrant, and Jenny Nelson. On the differences between dark and light ideality factor in polymer: fullerene solar cells. *The Journal of Physical Chemistry Letters*, 4(14):2371–2376, 2013.

[269] Uwe Rau. Tunneling-enhanced recombination in cu (in, ga) se2 heterojunction solar cells. *Applied Physics Letters*, 74:111, 1999.

[270] Silke Steingrube, Otwin Breitenstein, Klaus Ramspeck, Stefan Glunz, Andreas Schenk, and Pietro P Altermatt. Explanation of commonly observed shunt currents in c-si solar cells by means of recombination statistics beyond the shockley-read-hall approximation. *Journal of Applied Physics*, 110(1):014515, 2011.

[271] O Breitenstein, P Altermatt, K Ramspeck, MA Green, Jianhua Zhao, and A Schenk. Interpretation of the commonly observed iv characteristics of c-si cells having ideality factor larger than two. In *2006 IEEE 4th World Conference on Photovoltaic Energy Conference*, volume 1, pages 879–884. IEEE, 2006.

[272] Christopher M Proctor, Martijn Kuik, and Thuc-Quyen Nguyen. Charge carrier recombination in organic solar cells. *Progress in Polymer Science*, 38(12):1941–1960, 2013.

[273] Hao Hu, Ka Kan Wong, Tom Kollek, Fabian Hanusch, Sebastian Polarz, Pablo Docampo, and Lukas Schmidt-Mende. Highly efficient reproducible perovskite solar cells prepared by low-temperature processing. *Molecules*, 21(4):542, 2016.

[274] Mingzhen Liu, Michael B Johnston, and Henry J Snaith. Efficient planar heterojunction perovskite solar cells by vapour deposition. *Nature*, 501(7467):395–398, 2013.

[275] Azhar Fakharuddin, Francesca De Rossi, Trystan M Watson, Lukas Schmidt-Mende, and Rajan Jose. Research update: Behind the high efficiency of hybrid perovskite solar cells. *APL Materials*, 4(9):091505, 2016.

[276] Jiewu Cui, Yucheng Wu, Yan Wang, Hongmei Zheng, Guangqing Xu, and Xinyi Zhang. In-situ fabrication of aao template without oxide barrier layer and its applications. *Journal of nanoscience and nanotechnology*, 12(4):3130–3134, 2012.

[277] A. V. Kabashin, P. Evans, S. Pastkovsky, W. Hendren, G. A. Wurtz, R. Atkinson, R. Pollard, V. A. Podolskiy, and A. V. Zayats. Plasmonic nanorod metamaterials for biosensing. *Nat Mater*, 8(11):867–871, 2009.

[278] Jeffrey N. Anker, W. Paige Hall, Olga Lyandres, Nilam C. Shah, Jing Zhao, and Richard P. Van Duyne. Biosensing with plasmonic nanosensors. *Nat Mater*, 7(6):442–453, 2008.

[279] John McPhillips, Antony Murphy, Magnus P. Jonsson, William R. Hendren, Ronald Atkinson, Fredrik Hoeoek, Anatoly V. Zayats, and Robert J. Pollard. High-performance biosensing using arrays of plasmonic nanotubes. *ACS Nano*, 4(4):2210–2216, 2010.

[280] M. E. Nasir, W. Dickson, G. A. Wurtz, W. P. Wardley, and A. V. Zayats. Hydrogen detected by the naked eye: Optical hydrogen gas sensors based on core/shell plasmonic nanorod metamaterials. *Advanced Materials*, 26(21):3532–3537, 2014.

[281] Mark S Tame, KR McEnery, SK Ozdemir, J Lee, SA Maier, and MS Kim. Quantum plasmonics. *Nature Physics*, 9(6):329–340, 2013.

[282] Alejandro Varas, Pablo Garcia-Gonzalez, Johannes Feist, FJ Garcia-Vidal, and Angel Rubio. Quantum plasmonics: from jellium models to ab initio calculations. *Nanophotonics*, 2016.

[283] Jean-Sebastien G. Bouillard, Wayne Dickson, Daniel P. O'Connor, Gregory A. Wurtz, and Anatoly V. Zayats. Low-temperature plasmonics of metallic nanostructures. *Nano Letters*, 12(3):1561–1565, 2012.

[284] Qijun Liang, Shanpeng Wang, Xutang Tao, and Thomas Dekorsy. Temperature dependence of free carriers and optical phonons in liinse 2 in the terahertz frequency regime. *Physical Review B*, 92(14):144303, 2015.

[285] William L Barnes. Surface plasmon–polariton length scales: a route to sub-wavelength optics. *Journal of optics A: pure and applied optics*, 8(4):S87, 2006.

[286] Priti Tiwana, Pablo Docampo, Michael B Johnston, Henry J Snaith, and Laura M Herz. Electron mobility and injection dynamics in mesoporous zno, sno2, and tio2 films used in dye-sensitized solar cells. *ACS nano*, 5(6):5158–5166, 2011.

[287] Narendra S Parmar, Caleb D Corolewski, Matthew D McCluskey, and KG Lynn. Potassium acceptor doping of zno crystals. *AIP Advances*, 5(5):057107, 2015.

[288] Kevin M Coakley, Bhavani S Srinivasan, Jonathan M Ziebarth, Chiatzun Goh, Yuxiang Liu, and Michael D McGehee. Enhanced hole mobility in regioregular polythiophene infiltrated in straight nanopores. *Advanced Functional Materials*, 15(12):1927–1932, 2005.

[289] Chiatzun Goh, R Joseph Kline, Michael D McGehee, Ekaterina N Kadnikova, and Jean MJ Frechet. Molecular-weight-dependent mobilities in regioregular poly (3-hexyl-thiophene) diodes. *Applied Physics Letters*, 86(12):122110, 2005.

[290] Steve Albrecht, Silvia Janietz, Wolfram Schindler, Johannes Frisch, Jona Kurpiers, Juliane Kniepert, Sahika Inal, Patrick Pingel, Konstantinos Fostiropoulos, Norbert Koch, et al. Fluorinated copolymer pcpdtbt with enhanced open-circuit voltage and reduced recombination for highly efficient polymer solar cells. *Journal of the American Chemical Society*, 134(36):14932–14944, 2012.

[291] Rachel L Chamousis, Lilian Chang, William J Watterson, Rick D Montgomery, Richard P Taylor, Adam J Moule, Sean E Shaheen, Boaz Ilan, Jao van de Lagemaat, and Frank E Osterloh. Effect of fractal silver electrodes on charge collection and light distribution in semiconducting organic polymer films. *Journal of Materials Chemistry A*, 2(39):16608–16616, 2014.

Publications, Conferences and Teaching

List of Publications

(1) **Yuyi Feng***, Kwang-Dae Kim, Clayton A. Nemitz, Paul Kim, Thomas Pfadler, Melanie Gerigk, Sebastian Polarz, James A. Dorman, Jonas Weickert, Lukas Schmidt-Mende* *Uniform large-area free-standing silver nanowire arrays on transparent conducting substrates*, J. Electrochem. Soc. **2016**, 163(8), 6.

(2) Kwang-Dae Kim, Thomas Pfadler, Eugen Zimmermann, **Yuyi Feng**, James A. Dorman, Jonas Weickert*, and Lukas Schmidt-Mende* *Decoupling Optical and Electronic Optimization of Organic Solar Cells using High-Performance Temperature-Stable $TiO_2/Ag/TiO_2$ Electrodes*, APL Mat. **2015**, 3, 106105.

Conferences, Workshops and Scientific Visits

2016

REFINE Summer School 2016, Oberstdorf, Germany (Oral & Poster)

European Materials Research Society (EMRS) Spring Meeting 2016, Lille, France (Poster)

2015

International Workshop on Magnetic Nanowires and Nanotubes 2015, Meersburg, Germany (Poster)

Short-Term Visit of the group of Prof. Henry Snaith (EU-40 Materials Winner) in the University of Oxford, and the group of Prof. Sir Richard Friend in the University of Cambridge, August 2015

2014

Trends in Nanotechnology International Conference (TNT) 2014, Barcelona, Spain (Poster)

2013

DPG School "Innovative Concepts in Photovoltaics" 2013, Bad Honnef, Germany (Poster)

Supervision and Teaching

Supervision

Deep Shah (University of Konstanz), Project Internship, Oct 2015 - Dec 2015

Paul Kim (University of Yale), DAAD's RISE scholarship program, May - August 2015

Clay Nemitz (University of North Carolina, Chapel Hill), Brown Family Internship Grant, May - August 2015

Michael Seybold (University of Konstanz), Project Internship, Oct 2014 - Feb 2015

Teaching

SS2016 Involvement in teaching *Physics of Organic and Hybrid Solar Cells*, University of Konstanz

SS2015 Involvement in teaching *Physics of Organic and Hybrid Solar Cells*, University of Konstanz

WS2014/15 Tutorial for *Advanced Experimental Course: Plasmonic Resonance*, University of Konstanz

WS2012/13 Tutorial for *Advanced Experimental Course: Plasmonic Resonance*, University of Konstanz

Acknowledgement

First and foremost, I truly thank Prof. Lukas Schmidt-Mende not only for giving me this opportunity to work in such a fascinating group, but also for strongly supporting me to become a better scientist. I have learned a lot from you – being open-minded, honest, enthusiastic, persistent and efficient. Moreover, I would like to thank you for listening to our words and being concerned for our happiness. I could not have hoped for a better supervisor than Lukas.

Likewise, I would like to thank Prof. Wei Xue for supporting me to transfer my PhD studies from China to abroad in order to explore wider world. You have had a profound influence on me concerning how to overcome difficult times, how to promote international mutual understanding and how to go beyond my limitations. Sometimes, I feel you believe in me more than I believe in myself. I think of you as a mentor for life.

Special thanks go to Jonas and Kwang-Dae for providing hands-on guidance in my experimental work and patiently answering my endless questions. Jonas, you are really gifted as a mentor. I very much enjoyed our discussions. I found it was amazing that you could always make my vague ideas clearer and deeper. Furthermore, your efficient work rhythm, assertiveness and your spirit of sharing have been always set a good example for me. KD Obba, I was very fortunate to work hands-on with such a professional, which can never be found in a textbook. Watching you doing experiments is like appreciating an amazing piece of art. Thank you for being in these years my great working partner, inspiration, wise advisor, and mostly, my true friend.

I also would like to express my deepest gratitude to the professors and students who have provided valuable advice and technical assistance to my research: Prof. Johannes Boneberg (thank you for generously offering me your precious experimental experience and equipment for making polystyrene spheres monolayer), Prof. Paul Leiderer (it was highly enjoyable to do experiments with you and I cannot wait to do more exciting collaboration work in the future), Prof. Alfred Leitenstorfer (thank you for opening our eyes to the beauty of semiconductor physics, and in particular for switching from German to English for the first time in the course just for me), Prof. Karl Leo, Prof. Mingguo Ma, Prof. Georg Maret, Prof. Kevin P. Musselman, Prof. Kornelius Nielsch, Prof. Sebastian Polarz, Prof. Ulli Steiner, Prof. Rainer Winter, Prof. Jinhu Yang, Dr. Jae-Hong Lim, Dr. Bingqiang Lu, Dr. Torsten Pietsch, Dr. Liangfei Tian, Mathias Altenburg, Sergej Andreev (thanks for our many sparkling moments of discussions), Hans Ballot, Melanie Gerigk, Matthias Hagner, Louis Kukk, Peter Nietsch, Hamidreza Riazi-Nejad, Peter Romer and Stefan Scheerer.

This work also comes from the efforts of my students. Michael S., thanks for your patience in preparing plenty of AAO samples to enable me to tackle the important challenges. I am very grateful that although you already left our group for several months, you kindly volunteered to come back to transfer your experimental experience to Clay N., which greatly promoted the project's progress. Paul K., your high levels of self-discipline, efficiency and innovation astonished me. It was such luck to work with you to achieve fruitful results in only three months. You give me strong faith that we can conquer more challenges of this project after you leave, and I strongly wish our work will be published in the future. Clay N., thank you so much for correcting our manuscript around 50 times with incredible patience, which helped me build my confidence with scientific writing. Deep S., thanks for volunteering to assist me in my research work, which greatly accelerated the project's progress.

Furthermore, I would like to thank my other lovely group members. Each one of you comes to this group with unique shining points. James, thanks for saying to me "our Postdocs are always available to help you", and for your awesome turkey on Thanksgiving Day. Julian. K, thanks for your company in the same office from the beginning until the end of our PhD studies. Many thanks for helping me with so much administrative stuff when I had language barriers, for accompanying me to pass through the dark forest when I missed the last bus at night, and also for the mental support. Thomas, thanks for your brilliant suggestions, which always hit the nail right on the head. Eugen, your wealth of experience of equipment and software, many creative scientific ideas and willingness to help people amazed me. Thank you, adorable Eugen! Chaw Loon, Kevin and Sajad, thanks for the golden period of daily dinner get-together time, when we freely talked about our experimental problems and also amazing exotic cultures. Caro, Corina, Kali, Philipp E., Susi, and Sammy, thanks for involving me in the discussion in the young physicists' society, for the crazy night of German football championship on 13 July 2014, for the sweet time of sailing, picnics and home parties. Matthias N., Martin and Tobias, your cool guys' half-year travel over the world inspired me to think big and go beyond my limits to explore the world. Hao, thanks for your help with moving heavy equipment, and for comforting me with nice Chinese food when I felt upset. Christina, thanks for spending a short but beautiful period together in the same office. The talk on comparing our education and childhood experience helped me understand more about the confusions I encountered in Germany before we met. Julian R., thanks for patiently instructing me lots of equipment in our lab, and also for beautiful tiramisu and coffee time. William, your passion for learning German increased my motivation in learning the language. Alex, Frank, Lukas K., Maren, Markus, Michael M., Mihi, Patrik, Paul Z., Philipp B., Pius, Sabrina, Simon, Stefan J. and Stefan S., thanks for great barbecue and cake time, when we had nice conversations. Furthermore, I appreciate the wonderful strawberry-picking, baking and traveling time together with the international exchange students: Berit, Emily, Samantha, Sara, Sooyon and Harsh. You helped improve my English, and inspired me to travel alone in Scandinavia, which turned out to be an unforgettable wonderful experience in my lifetime. Prof. John and Dr. Maria, thanks for sharing your rich research experience with us during your visit in

our lab. Azhar, Ananth, Jeldrik, Shaista, Sohaila, and Zhaoke, your arrival has injected lots of new vigor into our group. Friederike, Nicole and Stefanie, thanks for helping me with lots of administrative things, for our nice conversations, and for sweet ice cream time. Lastly, I want to thank a very important person, Haiyan, the pioneer Chinese student in this group. Although you already had left when I came to this group, it is wonderful to keep in touch with you. Your valuable advice helped me such a lot in adapting to this new environment, and also helped me make good progress in my PhD.

I was very fortunate to meet like-minded and ambitious friends at conferences, and furthermore established great collaborations. A big thanks for the wonderful time together goes to Dr. Isan Amin, Dr. Xuecheng Chen, Dr. Sedat Dogan, Dr. Matthias Feinäugle, Dr. Kun Gao, Dr. Joachim Glatz-Reichenbach, Dr. Kai Li, Dr. Tobias Mönch, Dr. Eberhard Richter, Dr. Kirill Zilberberg, Yuan Gao, Yaxiang Lu, Stefanie Schlicht, and Yoonseok Park (your transparent electrode technique gave me hope when I got stuck with my project). Additionally, I greatly appreciate Prof. Henry Snaith, Prof. Sir. Richard Friend, Prof. Judith Driscoll for giving me opportunities to visit their labs in the University of Oxford and University of Cambridge to broaden my academic horizons. And also thanks to the local students: Andreas W., Robert, Severin and Yulia for warm welcoming lab-tours and inspiring discussions.

Furthermore, I have enjoyed my PhD studies with the support of the Welcome Center, Academic Staff Development, Research Support and Equal Opportunity Committee, specifically Johannes Dingler, Tanja Edelhäußer, Anja Eisenbeiß, Silke Hell, Silke Kiebler and Heike Kühmoser. I will always have fond memories of the University of Konstanz and I hope she will be proud of me in the future.

I would also like to take this opportunity to thank the impressive mentors I have encountered during my education. Thanks to Prof. Weiguang Ma, Prof. Yan Zhao, Prof. Kuanshou Zhang and Prof. Ting Zhang for your unwavering encouragement, love, trust and support. I am very grateful to consider you as both mentors and friends.

Special thanks goes to Ananth, Clay, Eugen, Hao.C, Kevin, Kirill, Paul.K, Philipp.E, Sajad and Michael.S for proof-reading and valuable feedback.

I acknowledge the Chinese Scholarship Council (CSC) for the generous funding of my PhD studies.

Additionally, I have received tremendous support from many great friends and families during this wonderful and adventurous journey. Thanks to my regular running team members: Lingdan, Nijie, Qijun, Simin, Xiaohui and Yiqun for your positive influence. Thanks also to my traveling friends: Binbin, Fei, Nina, Qiaohao, Yannan, Zhenghui, etc. for exploring new architectures and cultures together. Thanks to Fan, Lei, Heng, Hong, Meng, Mengdi, Pengpeng, Yan, Yunlong, Zhengyang, Zhu, etc. for dinner parties on big Chinese festivals, which made me very relieved and much less homesick. Thanks to my elegant swimming classmates: Eleanor, Maria, Nurjamal and Oleksandra for our

joint discovery of our strength as women. Thanks to my German and dancing teachers: Isabel Kern and Heike Wawersich, for making the class so attractive that a stable of classmates followed you over years. Thanks to the warm and caring Reimann family for great food and practical advice. Moreover, thanks to my gym, snow-hiking and Bondensee-sport buddies: Andi D., Philipp E., Seven F., Markus H., Norman M., Peter M., Juan Q., Tadeus R., and Konfeng Z. for your patience in talking to me in German, for giving me the assurance to try new exciting sports, for embracing the energy of the Apls and Bondensee. I will always think of Konstanz as my second hometown.

Finally, I would like to thank my family and relatives for standing behind me many years through my studies. Thank you Mum & Dad for creating a warm haven of a home, where I can throughly relax to embrace new inspirations. I also thank my grandparents, aunties and uncles for inspiring talks about research methods, career development and the valuable experience of life. Moreover, I cannot thank my boyfriend Hao Chen enough for his enduring love, cherishing, patience, encouragement, inspiration and support.

To these and all people who I have forgotten to express my thanks: thank you!